



CHITOSAN-CAPPED GOLD NANOPARTICLES AND THE DEVELOPMENT OF
DISSOLVING MICRONEEDLES LOADING CHITOSAN-CAPPED GOLD
NANOPARTICLES FOR TRANSDERMAL DELIVERY



A Thesis Submitted in Partial Fulfillment of the Requirements
for Doctor of Philosophy PHARMACEUTICAL TECHNOLOGY
(INTERNATIONAL PROGRAM)

Department of PHARMACEUTICAL TECHNOLOGY

Silpakorn University

Academic Year 2022

Copyright of Silpakorn University

อนุภาคนาโนทองและการพัฒนาไมโครน็ดเคลือบชนิดละลายสำหรับเพิ่มการนำส่งสาร
ชอน้ำผ่านทางผิวหนัง



โดย
นางสาวกนกวรรณ สิงห์พัดนา

วิทยานิพนธ์นี้เป็นส่วนหนึ่งของการศึกษาตามหลักสูตรปรัชญาดุษฎีบัณฑิต
สาขาวิชาเทคโนโลยีสารสนเทศ (หลักสูตรนานาชาติ) แบบ 1.2 ปรัชญาดุษฎีบัณฑิต
ภาควิชาเทคโนโลยีสารสนเทศ
มหาวิทยาลัยศิลปากร
ปีการศึกษา 2565
ลิขสิทธิ์ของมหาวิทยาลัยศิลปากร

CHITOSAN-CAPPED GOLD NANOPARTICLES AND THE
DEVELOPMENT OF DISSOLVING MICRONEEDLES LOADING
CHITOSAN-CAPPED GOLD NANOPARTICLES FOR
TRANSDERMAL DELIVERY



By
MISS Kanokwan SINGPANNA

A Thesis Submitted in Partial Fulfillment of the Requirements
for Doctor of Philosophy PHARMACEUTICAL TECHNOLOGY
(INTERNATIONAL PROGRAM)

Department of PHARMACEUTICAL TECHNOLOGY

Silpakorn University

Academic Year 2022

Copyright of Silpakorn University

Title Chitosan-capped gold nanoparticles and the development of dissolving microneedles loading Chitosan-capped gold nanoparticles for transdermal delivery
By MISS Kanokwan SINGPANNA
Field of Study PHARMACEUTICAL TECHNOLOGY (INTERNATIONAL PROGRAM)
Advisor Professor Dr. Praneet Opanasopit, Ph.D.
Co advisor Professor Dr. Tanasait Ngawhirunpat, Ph.D.

Faculty of Pharmacy, Silpakorn University in Partial Fulfillment of the Requirements for the Doctor of Philosophy

..... Dean of Faculty of Pharmacy
(Assistant Professor Dr. Surasit Lochidamnuay)

Approved by Chair person
(Assistant Professor Dr. Wipada Samprasit, Ph.D.)

..... Advisor
(Professor Dr. Praneet Opanasopit, Ph.D.)

..... Co advisor
(Professor Dr. Tanasait Ngawhirunpat, Ph.D.)

..... Committee
(Associate Professor Dr. Prasopchai Patrojanasophon, Ph.D.)

..... Committee
(Assistant Professor Dr. Boonnada Pamornpathomkul, Ph.D.)

620830002 : Major PHARMACEUTICAL TECHNOLOGY (INTERNATIONAL PROGRAM)

Keyword : chitosan, gold nanoparticles, transdermal delivery, sodium fluorescein, fluorescein isothiocyanate-bovine serum albumin, skin permeation enhancer, dissolving microneedles

MISS Kanokwan SINGPANNA : Chitosan-capped gold nanoparticles and the development of dissolving microneedles loading Chitosan-capped gold nanoparticles for transdermal delivery Thesis advisor : Professor Dr. Praneet Opanasopit, Ph.D.

Drug administration through the skin is widely accounted as a convenient option. This study examined the effect of chitosan-stabilized gold nanoparticles (CS-AuNPs) and citrate ion-stabilized gold nanoparticles (Ci-AuNPs) on the skin permeation of fluorescein sodium salt (NaFI) and fluorescein isothiocyanate-bovine serum albumin (FITC-BSA), as small and large model hydrophilic permeants, respectively. CS-AuNPs and Ci-AuNPs were characterized by transmission electron microscopy (TEM) and dynamic light scattering (DLS) methods. To examine the skin permeation, studies were conducted on neonatal pig skin using vertical Franz diffusion cells, TEM, and confocal laser scanning microscopy (CLSM). The safety of CS-AuNPs on human skin fibroblast was also assessed using the MTT assay. The nanosized particles of the synthesized CS-AuNPs and Ci-AuNPs were in a spherical shape. The CS-AuNPs had a positive zeta potential, while the Ci-AuNPs had a negative zeta potential. According to the skin permeation study, CS-AuNPs were found to effectively improve the permeation of both NaFI and FITC-BSA. Additionally, CLSM visualization indicated that skin permeation was enhanced by improving the delivery through the transepidermal pathway. The CS-AuNPs were considered safe for human skin cells. The distribution study also found that the particles mainly remained on the upper layers of the skin and did not permeate. Above all, CS-AuNPs show potential as a skin permeation enhancer for hydrophilic compounds in cosmetics and pharmaceuticals. Furthermore, dissolving microneedles (DMNs) incorporated with CS-AuNPs (Au-MNs) were developed to enhance skin delivery. CS-AuNPs at 15% wt were added to the polymer solution to create Au-MNs using microneedle molds. However, our study showed that combining CS-AuNPs with DMNs did not have a synergistic effect to increase skin drug delivery of hydrophilic molecules.

ACKNOWLEDGEMENTS

I would like to express my deepest appreciation to my advisors Professor Dr. Praneet Opanasopit and Professor Dr. Tanasait Ngawhirunpat for their support, patience, guidance, dedication, encouragement, and knowledge given to me. I am also thankful to the committee, Associate Professor Dr. Prasopchai Patrojanasophon and Assistant Professor Dr. Boonada Pamornpathomkul, for their help and guidance. Furthermore, words cannot express my gratitude to Dr. Chaiyakarn Pornpitchanarong for his inspiration, encouragement, valuable advice and suggestions, assistance with editing and proofreading, and overall support during my Ph.D. journey. I feel so grateful for the opportunity to have commenced my doctoral study at this prestigious institution.

Additionally, I would like to express my gratitude to Professor Dr. Kevin Li for accepting me to join his lab group at the James L. Winkle College of Pharmacy, University of Cincinnati, USA and for sharing his knowledge and expertise with me. Working with him and his lab group has been a remarkable and invaluable experience. His guidance developed my ideas and skills as well as augmented my individuality to become a proficient researcher.

I am also grateful to all my friends, lab members of the Pharmaceutical Development of Green Innovation Group (PDGIG), and staff members for their assistance and support. I truly appreciate and would like to acknowledge the Faculty of Pharmacy, Silpakorn University for the financial support to pursue my Ph.D.

In particular, I would like to extend my heartfelt gratitude to all my beloved ones, especially my parents, sister, and grandmother, for their understanding and belief in me. Lastly, I would be remiss in not mentioning Mr. Kawinchan Huayhongthong. I sincerely thank for his encouragement and valuable support.

MISS Kanokwan SINGPANNA



TABLE OF CONTENTS

	Page
ABSTRACT.....	D
ACKNOWLEDGEMENTS.....	E
TABLE OF CONTENTS	F
LIST OF TABLES	K
LIST OF FIGURES	L
CHAPTER 1.....	4
1.1 Statement and significance of the research problem.....	4
1.2 OBJECTIVES.....	7
1.3 HYPOTHESES.....	8
CHAPTER 2.....	9
2.1 Transdermal delivery.....	9
2.1.1 Skin structure.....	9
2.1.2 Skin penetration pathway.....	14
2.2 Skin penetration enhancement strategies.....	15
2.2.1 Chemical enhancers.....	15
2.2.2 Physical enhancers.....	16
2.2.2.1 Iontophoresis.....	16
2.2.2.2 Sonophoresis.....	18
2.2.2.3 Electroporation.....	20
2.2.2.4 Microneedles (MNs).....	21
2.2.3 Nanocarrier systems.....	25

2.2.3.1 Lipid-based NPs	26
2.2.3.2 Polymeric NPs.....	30
2.2.3.3 Inorganic-based NPs	30
2.3 Gold nanoparticles (AuNPs)	31
2.3.1 Introduction and properties of AuNPs	31
2.3.2 Synthesis of AuNPs.....	34
2.3.3 Application of AuNPs	40
2.3.3.1 AuNPs as a delivery carrier.....	41
2.3.3.2 AuNPs for diagnostic, biosensing, and imaging.....	44
2.3.3.3 AuNPs for therapy.....	46
2.3.3.5 AuNPs for transdermal delivery.....	47
2.4 Method for evaluation skin delivery	49
2.4.1 Diffusion cells	50
2.4.2 Tape stripping.....	52
2.4.3 Confocal Laser Scanning Microscope (CLSM).....	53
CHAPTER 3.....	55
3.1 Materials	55
3.2 Equipments.....	56
3.3 Methods.....	57
3.3.1 The study of AuNPs	57
3.3.1.1 Synthesis of AuNPs.....	57
i. Citrate-stabilized AuNPs (Ci-AuNPs)	57
ii. Chitosan-capped AuNPs (CS-AuNPs)	58

3.3.1.2	Characterization of AuNPs	58
3.3.1.3	Effect of AuNPs on skin penetration	59
i.	Preparation of porcine skin.....	59
ii.	<i>In vitro</i> skin permeation test.....	59
3.3.1.4	AuNPs distribution in skin layers	60
i.	Quantitative analysis of AuNPs by inductively coupled plasma-mass spectrometry (ICP-MS)	60
3.3.1.5	Skin penetration pathways	61
i.	Confocal laser scanning microscopy (CLSM) study	61
3.3.1.6	Visualization of AuNPs in the skin by TEM	61
3.3.1.7	Cytotoxicity of AuNPs	62
3.3.1.8	Stability of AuNPs.....	62
3.3.2	Development and Fabrication of DMNs	62
3.3.2.1	Preparation of polymer solutions	62
3.3.2.2	Fabrication of DMNs	63
3.3.2.3	Fabrication of AuNPs-loaded DMNs (Au-MNs).....	63
3.3.2.4	Characterization of DMNs and Au-MNs.....	63
i.	Morphology	63
ii.	Mechanical strength.....	63
iii.	Skin insertion	64
iv.	Ex vivo skin dissolution study	64
3.3.2.5	<i>In vitro</i> skin permeation of AuNPs loaded MNs (Au-MNs)	65
3.3.2.6	Stability of Au-MNs.....	65

3.3.3 Quantitative assay of hydrophilic compounds.....	65
3.3.3.1 Fluorescein sodium (NaFl)	65
3.3.3.2 Albumin-fluorescein isothiocyanate conjugate (FITC-BSA).....	66
3.3.4 Data analysis and Statistics	66
CHAPTER 4.....	67
4.1 The study of AuNPs.....	67
4.1.1 Characterization of AuNPs	67
4.1.2 <i>In vitro</i> skin permeation study	69
4.1.2.1 Effect of AuNPs on skin penetration	69
i. Skin penetration of small hydrophilic permeants: NaFl	69
ii. Skin penetration of large hydrophilic permeants: FITC-BSA	71
4.1.2.2 Effect of the concentration of CS-AuNPs on skin penetration	74
4.1.3 CS-AuNPs distribution in skin layers	78
4.1.5 Cytotoxicity of CS-AuNPs.....	82
4.1.6 Stability of AuNPs	83
4.2 Development and fabrication of DMNs.....	85
4.2.1 Physical appearance of DMNs and Au-DMNs.....	85
4.2.2 Mechanical strength evaluation	87
4.2.3 Skin insertion	88
4.3.4. <i>Ex vivo</i> skin dissolution study.....	89
4.3.5 <i>In vitro</i> skin permeation of AuNPs loading MNs (Au-MNs)	90
4.3.6 Stability of Au-MNs.....	92

CHAPTER 5.....	93
5.1 The study of AuNPs on skin permeation	93
5.2 Development and Fabrication of DMNs.....	93
REFERENCES	95
VITA.....	113



LIST OF TABLES

	Page
Table 1 Hydrodynamic diameter, PDI, and ZP of AuNPs.....	68
Table 2 The stability of Ci-AuNPs and CS-AuNPs.....	84
Table 3 Physical appearance of fabricated MNs under microscope	86



LIST OF FIGURES

	Page
Figure 1 Skin anatomy and its components (27).....	9
Figure 2 Epidermis layer of human skin.....	10
Figure 3 Schematic of epidermal structure (30).....	11
Figure 4 Cross section of human skin representing the layers of dermis (33).	13
Figure 5 Schematic of skin penetration pathways (36).	14
Figure 6 Examples of chemical enhancers in transdermal drug delivery (37).....	16
Figure 7 Iontophoresis schematic diagram (41).	17
Figure 8 The experimental set up of sonophoresis (45).....	18
Figure 9 The proposed mechanisms of sonophoresis by the cavitation effect (46).....	19
Figure 10 (A) Experimental set up of electroporation device (B) Hypothesized pore forming by electroporation and the recovery (51).....	20
Figure 11 Illustration of skin penetration of polymeric MNs (56).....	21
Figure 12 Various shapes of MNs: (a) cylindrical, (b) tapered tip, (c) canonical, (d) square base, (e) pentagonal-base canonical tip, (f) side-open single lumen, (g) double lumen, (h) side-open double lumen (57).....	22
Figure 13 Drug delivery mechanism of various microneedles (58)	23
Figure 14 NPs classifications and their features (9).....	26
Figure 15 Classification of liposomes based on size and lamellarity (73).....	27
Figure 16 The structure of niosomes (74).	28
Figure 17 Schematic presentation of oil-in water and water-in-oil nanoemulsions (76). ..	28
Figure 18 The structure of SLNs and NLCs (83).	30

Figure 19 The colors of AuNPs at different particle size (90).	31
Figure 20 The colors of AuNPs in different shape (91).....	32
Figure 21 (a) UV absorbance of AuNPs (red line) and the aggregation state (purple line), TEM images of (b) AuNPs and (c) aggregated AuNPs (92).	32
Figure 22 Schematic of a single AuNP structure (10).	33
Figure 23 Schematic of surface plasmon resonance of AuNPs (89).	34
Figure 24 Top-down and bottom-up approaches for AuNPs synthesis (102).....	35
Figure 25 Bottom-up approach using chemical reduction	35
Figure 26 Representative of stabilizing agents of AuNPs (100).	36
Figure 27 Synthesis of AuNPs by Turkevich method (105).	37
Figure 28 Schematic of Brust-Schiffrin method for AuNPs synthesis (107).	38
Figure 29 Chemical structure of chitosan (112).	39
Figure 30 Synthesis of chitosan-capped AuNPs (92).....	39
Figure 31 Schematic illustrating various surface functionalities employed in AuNPs (114).	40
Figure 32 Medical application of AuNPs (88).	40
Figure 33 Conjugation strategies of AuNPs through covalent and non-covalent conjugation (95).	41
Figure 34 Schematic for Au-GSH-Dox (121).	42
Figure 35 (a) Schematic representation of AuNP/CRISPR nanoformulation (b) TEM images of AuNP and AuNP/CRISPR nanoformulations (124).	43
Figure 36 The application of AuNPs as a delivery carrier for cancer therapy (88).	44
Figure 37 Schematic of in cell tracking by AuNPs and CT imaging (135).	45

Figure 38 CT scans demonstrated AUNPs migration (a) 3D CT image of AuNPs accumulation in the lungs (b) 2D CT image of AuNPs in lung (c) Accumulation of AuNPs in tumor (135).....	46
Figure 39 The application of PTT, PDT and RT for AuNPs (88).	47
Figure 40 Graphical representation of (A) untreated skin, (B) skin treated with ketoprofen patch without AuD, and (C) skin treated with ketoprofen-incorporated AuD patch (15).	48
Figure 41 Schematic presentation of protein antigen transcutaneous delivery by AuNPs (17).	49
Figure 42 (A) Horizontal diffusion cell and (B) Flow-through cell (144).	50
Figure 43 Graphical diagram of vertical static diffusion cell (146).	51
Figure 44 Typical plot of skin permeation study (147).	52
Figure 45 Tape stripping of stratum corneum (148).	53
Figure 46 Schematic diagram of CLSM (149).	53
Figure 47 Ci-AuNPs and CS-AuNPs exhibited ruby red color with the SPR absorption band at 520 nm.....	68
Figure 48 TEM images of (A) Ci-AuNPs and (B) CS-AuNPs at 300k×magnification.	69
Figure 49 Skin permeation profile of NaFl using CS-AuNPs, Ci-AuNPs, CS solution as skin penetration enhancers and NaFl in aqueous solution (as a control). Each data point represents the mean±SD (n=3). * $p < 0.05$ vs control, # $p < 0.05$ vs CS solution, and § $p < 0.05$ vs Ci-AuNPs.	70
Figure 50 (A) J_{ss} and (B) ER of NaFl using CS-AuNPs, Ci-AuNPs, CS solution as skin penetration enhancers, and NaFl in aqueous solution (as a control). Each value represents the mean±SD (n=3). * $p < 0.05$ vs control, # $p < 0.05$ vs CS solution, § $p < 0.05$ vs Ci-AuNPs.	71

- Figure 51 Skin permeation profile of FITC-BSA using CS-AuNPs, Ci-AuNPs, CS solution as skin penetration enhancers and FITC-BSA in aqueous solution (as a control). Each data point represents the mean±SD (n=3). * p <0.05 vs control, # p <0.05 vs CS solution, \$ p <0.05 vs Ci-AuNPs..... 72
- Figure 52 (A) J_{ss} and (B) ER of FITC-BSA using CS-AuNPs, Ci-AuNPs, CS solution as skin penetration enhancers and FITC-BSA in aqueous solution (as a control). Each value represents the mean±SD (n=3). * p <0.05 vs control, # p <0.05 vs CS solution, \$ p <0.05 vs Ci-AuNPs. 73
- Figure 53 Skin permeation profile of NaFl with different concentrations of CS-AuNPs. NaFl in aqueous solution was used as a control. Each data point represents the mean±SD (n=3). * p <0.05 vs control..... 75
- Figure 54 (A) J_{ss} and (B) ER of NaFl with different concentrations of CS-AuNPs. NaFl in aqueous solution was used as a control. Each data point represents the mean±SD (n=3). * p <0.05 vs control..... 75
- Figure 55 Skin permeation profile of FITC-BSA with different concentrations of CS-AuNPs. FITC-BSA in aqueous solution was used as a control. Each data point represents the mean±SD (n=3). * p <0.05 vs control..... 76
- Figure 56 (A) J_{ss} and (B) ER of FITC-BSA with different concentrations of CS-AuNPs. FITC-BSA in aqueous solution was used as a control. Each data point represents the mean±SD (n=3). * p <0.05 vs control..... 77
- Figure 57 The percentage amount of Au found in the epidermal layer, dermal layer, and receptor fluid after 24-h skin permeation test. *Significant difference (p <0.05) vs receptor fluid..... 79
- Figure 58 TEM images of CS-AuNPs (shown as small particles in the circled area) in the SC layer of porcine skin. 79
- Figure 59 CLSM images of NaFl penetration at the area near the hair follicle of (A) CS-AuNPs group (B) control, and the penetration at non-follicular region (the circled area) of

(C) CS-AuNPs group and (D) control. The semi-cylindrical structures are related to hair shafts.	80
Figure 60 CLSM images of FITC-BSA penetration at the area near the hair follicle of (A) CS-AuNPs, (B) control, and the penetration at non-follicular region (the circled area) of (C) CS-AuNPs group, and (D) control. The semi-cylindrical structures are related to hair shafts.	81
Figure 61 Cell viability of NHF and HaCaT following the 24 h-treatment with CS-AuNPs at different concentrations *Statistically significant ($p < 0.05$) vs untreated control.	83
Figure 62 Illustrations of (A) CS-AuNPs and (B) Ci-AuNPs.	85
Figure 63 SEM image of 15%wt CS-AuNPs-loaded MNs performing at 10 kV and 225 \times magnification.....	87
Figure 64 Percentage height reduction of MNs after compressing with the force at 10.769 N per 121 needles with the speed of 0.5 mm per second. *Statistically significant ($p < 0.05$) vs control (Blank MNs).....	88
Figure 65 Stained microholes on porcine skin following the insertion of (A) DMNs and (B) 15%wt CS-AuNPs loaded MNs.....	89
Figure 66 <i>Ex vivo</i> skin dissolution of (A) DMNs and (B) 15%wt CS-AuNPs loaded MNs at different time points in an incubator at the temperature of 37 ± 1 $^{\circ}\text{C}$	89
Figure 67 Skin permeation profile of NaFl entrapped in DMNs and Au-MNs. Each data point represents the mean \pm SD (n=3).	90
Figure 68 Skin permeation profile of FITC-BSA entrapped in DMNs and Au-MNs. Each data point represents the mean \pm SD (n=3).	90
Figure 69 The enhancement ratios of NaFl entrapped in DMNS and Au-MNs compared to AuNPs. Each data point represents the mean \pm SD (n=3) *Statistically significant ($p < 0.05$) vs CS-AuNPs.....	91

Figure 70 The enhancement ratios of FITC-BSA entrapped in DMNS and Au-MNs compared to AuNPs. Each data point represents the mean \pm SD (n=3) *Statistically significant ($p<0.05$) vs CS-AuNPs. 91

Figure 71 Mechanical strength during 6-month stability study of Au-MNs (expressed as percentage height reduction after compressing with the force at 10.769 N per 121 needles with the speed of 0.5 mm per second)..... 92



LIST OF ABBREVIATIONS

ANOVA	Analysis of variance
Au	Gold
AuNPs	Gold nanoparticles
Au-MNs	Gold nanoparticles-loaded microneedles
°C	Degree Celsius
Ci-AuNPs	Citrate-stabilized gold nanoparticles
CS	Chitosan
CS-AuNPs	Chitosan-capped gold nanoparticles
CLSM	Confocal laser scanning microscope
cm	centimeter(s)
cm ²	Square centimeter(s)
CO ₂	Carbon dioxide
Da	Dalton
DLS	Dynamic light scattering
DMNs	Dissolving microneedles
DMSO	Dimethyl sulfoxide
Eq.	Equation
ER	Enhancement ratio
FITC-BSA	Fluorescein isothiocyanate-bovine serum albumin
h	Hour(s)
HA	Hyaluronic acid
HPMC	hydroxypropyl methylcellulose
ICP-MS	Inductively coupled plasma-mass spectrometry
i.e.	<i>id est</i> (Latin abbreviation); that is
J _{ss}	Transdermal flux at steady-state
KCl	Potassium chloride
kDa	Kilodalton
kg	Kilogram(s)
KH ₂ PO ₄	Potassium dihydrogen orthophosphate
kV	Kilovolt(s)

L	Liter(s)
CLSM	Confocal laser scanning microscope
logP	Log partition-coefficient
m ²	Square centimeter(s)
mg	Milligram(s)
min	Minute(s)
mL	Milliliter(s)
mm	Millimeter(s)
MNs	Microneedle(s)
MTT	3-(4,5-dimethylthiazol-2-yl)-2,5-diphenyltetrazolium bromide
MTX	Methotrexate
MW	Molecular weight
N	Newton
NaCl	Sodium chloride
NaFl	Fluorescein sodium salt
NaHCO ₃	Sodium bicarbonate
NaOH	Sodium hydroxide
NLC	Nanostructured lipid carriers
nm	Nanometer(s)
NHF	Normal human fibroblasts
NPs	Nanoparticles
OD	Optical density
OVA	Ovalbumin
PAMA	Poly(acrylic acid-co-maleic acid)
PBS	Phosphate buffered saline
PCR	Polymerase chain reaction
PDI	Polydispersity index
PDMS	Polydimethylsiloxane
pH	Potential of hydrogen
PDT	Photodynamic therapy

PLGA	Poly (lactic- <i>co</i> -glycolic acid)
PTT	Photothermal therapy
PVP	Polyvinylpyrrolidone
PVA	Polyvinyl alcohol
R ²	Coefficient of determination
RA	Rheumatoid arthritis
RH	Relative humidity
ROS	Reactive oxygen species
rpm	Revolutions per minute
RT	Radiation therapy
s	Second
SC	Stratum corneum
S.D.	Standard deviation
SEM	Scanning electron microscope
SERS	surface-enhanced Raman scattering
SPR	Surface plasmon resonance
vs	versus
% wt	Percentage by weight
µg	Microgram(s)
µL	Microliter(s)
µm	Micrometer(s)
%	Percentage(s)
®	Registered trademark
SC	Stratum corneum
SLN	Solid lipid nanoparticles
TEM	Transmission electron microscope
TJ	Tight junctions
™	Trademark
UV	Ultraviolet
ZP	Zeta potential

CHAPTER 1

INTRODUCTION

1.1 Statement and significance of the research problem

The most common route for drug delivery is oral due to the patient's convenience and the ability for self-administration. Unfortunately, drugs delivered by the oral route undergo hepatic first-pass metabolism. Particularly, in the case of macromolecules (e.g., proteins and peptides), they can be degraded rapidly by gastric enzymes (1, 2). Parenteral route is another option to avoid degradation, but the injection is not widely accepted by patients because of pain and risk of infection. Skin becomes an attractive alternative to oral and parenteral delivery because of the ease of administration, convenience, and avoidance of hepatic first-pass metabolism. Transdermal drug delivery is developed to provide a safe and effective strategy of drug delivery for patients since the skin offers an attractive approach for drug administration (3, 4). However, there are many limitations associated with transdermal delivery. Firstly, the skin itself is considered a major barrier to drug absorption, especially the stratum corneum. Moreover, the delivery system's efficiency, stability, and skin compatibility are the factors that should be concerned. Numerous pharmaceuticals, including cosmeceutical developments on transdermal delivery, are engaged to overcome these limitations (3, 5).

Skin is the largest structure of the human body, serving as a protective barrier against hazardous substances, injury, and microorganisms. Also, it plays a crucial role in preventing moisture loss and regulating body temperature (5). Human skin is composed of 3 main layers, the epidermis, dermis, and subcutaneous layer. The epidermis is the outermost layer of skin, act as a waterproof barrier, determines the skin tone, and serves as the major barrier to drug absorption. The dermis, situate beneath the epidermis, consists of connective tissue, hair follicles, blood vessel, sweat glands, and sebaceous glands. The subcutaneous tissue located directly beneath the dermis, consists of connective tissue and adipose tissue serving as a storage site for fat while providing insulation and cushioning for the integument (6).

The skin's barrier properties selectively allow only molecules with favorable physicochemical characteristics to penetrate its layers and processing the stratum corneum. The characteristics include small size (MW 100-500 Da), unionized state, appropriate hydrophilicity/ lipophilicity (with logP value in the range 1-3) (6, 7). However, most drugs fail to meet these requirements, transdermal delivery systems have been developed to overcome the challenges associated with the barrier function of the skin. Many active and passive strategies have been introduced and applied for improving transdermal delivery systems. Active transdermal delivery involves the use of appropriate physical, electrical, or mechanical stimulation equipment, including microneedles. On the other hand, passive transdermal delivery aims to enhance skin permeability through the use of chemical enhancers, lipid-based vesicles (e.g., liposomes), nanoemulsions, polymeric nanoparticles, and metal-based nanoparticles (5, 8).

Nano-drug delivery systems or nanoparticles (NPs) are described as materials with a size less than 100 nm, which can be classified as lipid-based, polymeric, and inorganic-based NPs. Lipid-based NPs are structured vesicles made of lipids such as phosphatidylcholine and cholesterol. Examples of lipid-based NPs are liposomes, niosomes, ethosomes, transfersomes, solid lipid nanoparticles (SLN), and nanostructured lipid carriers (NLC). Polymeric NPs can be synthesized using natural or synthetic polymers. They can be classified as polymersome, dendrimer, polymer micelle, and nanosphere. In contrast, inorganic NPs are synthesized from inorganic materials such as gold, iron, and silica (9).

Gold is an inert atom widely used in nanotechnology, specifically as gold nanoparticles (AuNPs). Gold-based metal NPs are small gold particles with a diameter of 1-100 nm. These NPs consist of densely-packed gold atoms at their inner core, stabilized by ligands. AuNPs are an excellent material for investigation because they are non-toxic, highly stable, easy to synthesize, and their synthetic method is reproducible (10, 11). To date, AuNPs have found extensive application in various fields, including biological and biomedical fields. Several studies have proved the ability of AuNPs to penetrate the skin, making them a subject of many pieces of

research in transdermal delivery. The skin permeability of AuNPs is influenced by several factors, i.e., particles size, morphology, surface charge, chemical functionalization, and aggregation state. Skin permeability is size-dependent, with smaller particles show higher permeability compared to larger ones (12, 13). The effect of surface charge has been investigated. The positively charged AuNPs penetrate the skin more efficiently than the negatively and neutral charged particles due to the biological negativity of the skin attracting positively charged particles (14). In addition, the surface of AuNPs can be functionalized with a wide range of ligands, such as drugs, proteins, peptides, antibodies, DNA, including RNA, enabling them to serve as carriers. Surface modification facilitates drug loading, targeting, and skin penetration (10). Additionally, AuNPs also behave like an enhancer and help increase skin permeation of co-delivered drugs as well as macromolecules. This enhancement effect is attributed to hydrophobic interaction between AuNPs and the lipid structure of the skin, resulting in increased skin porosity and improved penetration of exogeneous compounds. (15-18).

Microneedle-based drug delivery has gained increased attention because microneedles (MNs) are capable of delivering a wide variety of molecules (from small drugs to macromolecules) to bypass the skin's barrier, specifically the stratum corneum. MNs are also non-invasive, painless, and allow self-administration. Because of their advantages, MNs become an interesting tool for improving transdermal delivery of drugs, proteins, peptides, vaccines, including cosmeceutical substances (19). MNs are defined as micron-scale needles that can create the micro-channel and allow drug transport across the skin (20). MNs are divided into solid, coated, hollow, hydrogel-forming, and dissolving MNs. Among these MNs, dissolving microneedles (DMNs) is highly interested due to many advantages, such as being easily made, high drug loading, safe, the one-step application which offers convenience for patients. DMNs are designed based on "poke and release" principle meaning that drugs are entrapped within the MNs, and after the skin insertion, the needles remain in the skin. Once the MNs dissolve or degrade in the skin, the drugs are released. Moreover, the MNs ensure safe disposal because needles are completely dissolved and leave no hazardous sharp waste (21-23). DMNs are usually made of hydrophilic polymers or

polysaccharides, e.g., hyaluronic acid (HA), polyvinyl pyrrolidone (PVP), polyvinyl alcohol (PVA), hydroxypropyl methylcellulose (HPMC), poly(acrylic acid-co-maleic acid) (PAMA), sucrose, trehalose, maltose, and dextran. However, most polymers are too soft and unable to be inserted into the skin. Thus, the structural materials are used in combination to increase the mechanical strength of the needles (19, 20, 22, 24, 25).

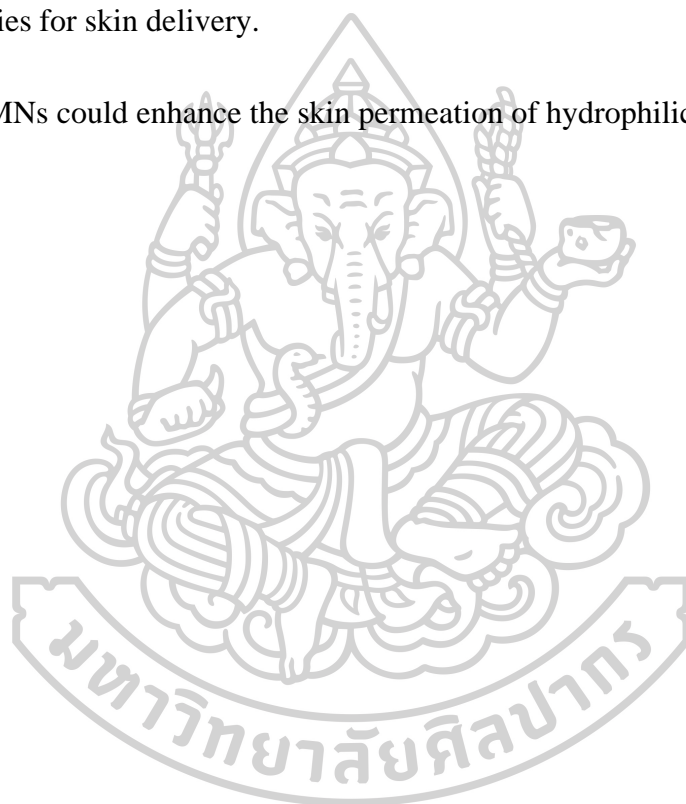
MNs array combined with AuNPs is now a novel method for transdermal delivery and their synergistic effect has not been widely investigated. The aim of this study is to investigate two types of AuNPs (citrate-stabilized (Ci-AuNPs) and chitosan-capped gold nanoparticles (CS-AuNPs)) for enhancing the skin penetration of fluorescent hydrophilic compounds (with small and large molecular weight, fluorescein sodium salt (NaFI) and albumin fluorescein isothiocyanate conjugate (FITC-BSA), respectively). The investigation includes elucidation of the penetration pathway and the mechanism. Furthermore, the effect of AuNPs-loaded MNs (Au-MNs) on skin delivery of hydrophilic compounds as well as the penetration pathway are also studied.

1.2 OBJECTIVES

1. To study the effect of physicochemical properties of AuNPs on *in vitro* skin permeation of hydrophilic compounds co-delivery with Ci-AuNPs and CS-AuNPs.
2. To examine the skin penetration pathway of hydrophilic compounds co-delivery with Ci-AuNPs and CS-AuNPs.
3. To develop and characterize AuNPs loaded MNs (Au-MNs) for skin penetration enhancement of hydrophilic compounds.
4. To evaluate the *in vitro* skin permeation of hydrophilic compounds from Au-MNs.

1.3 HYPOTHESES

1. Different physicochemical properties of AuNPs influence *in vitro* skin permeation of hydrophilic compounds
2. AuNPs enhance the skin permeation of hydrophilic compounds through either transappendageal or transepidermal pathway.
3. AuNPs-loaded MNs (Au-MNs) can be successfully developed with suitable properties for skin delivery.
4. Au-MNs could enhance the skin permeation of hydrophilic compounds.



CHAPTER 2

LITERATURE REVIEW

2.1 Transdermal delivery

2.1.1 Skin structure

Skin is the largest organ of the human body; it is estimated to be 15% of total body weight. The human skin is responsible for the protection against the harmful environment, prevention of moisture loss from the body, and regulation of body temperature. The skin can be divided into 3 main layers: epidermis, dermis, and subcutaneous tissue (Figure 1) (26).

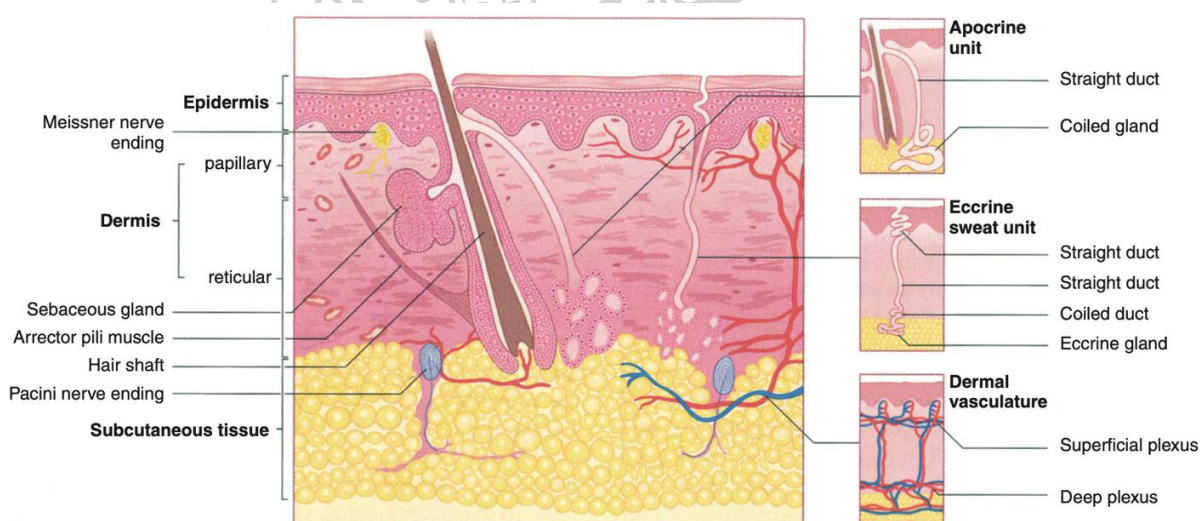


Figure 1 Skin anatomy and its components (27).

Epidermis

The epidermis is the outer layer of the skin that contains no blood vessel but composed of keratinized, stratified squamous epithelium that is continually being regenerated (Figure 2). It is usually divided into 5 sublayers based on the morphology and position of skin cells. From outside to inside, it begins with stratum corneum, stratum lucidum, stratum granulosum, stratum spinosum, and stratum basale. Cells in

the epidermis layer include a variety of cells, e.g., keratinocytes, corneocytes, melanocytes, Langerhans cells, and Merkel cells (28).

Keratinocyte is the most dominant component of the epidermis. It is formed by cell division at its base and continually moves towards the surface. These cells undergo maturation and differentiation as they move. They accumulate keratin, then gradually die and become flattened during the late phase of maturation. The dead cells are named corneocytes, and together they make up the very outer layer of the epidermis providing a protective barrier called the stratum corneum (also known as the horny layer). In healthy epidermis, the cells undergo regeneration and desquamation process approximately every 28 days (28, 29).

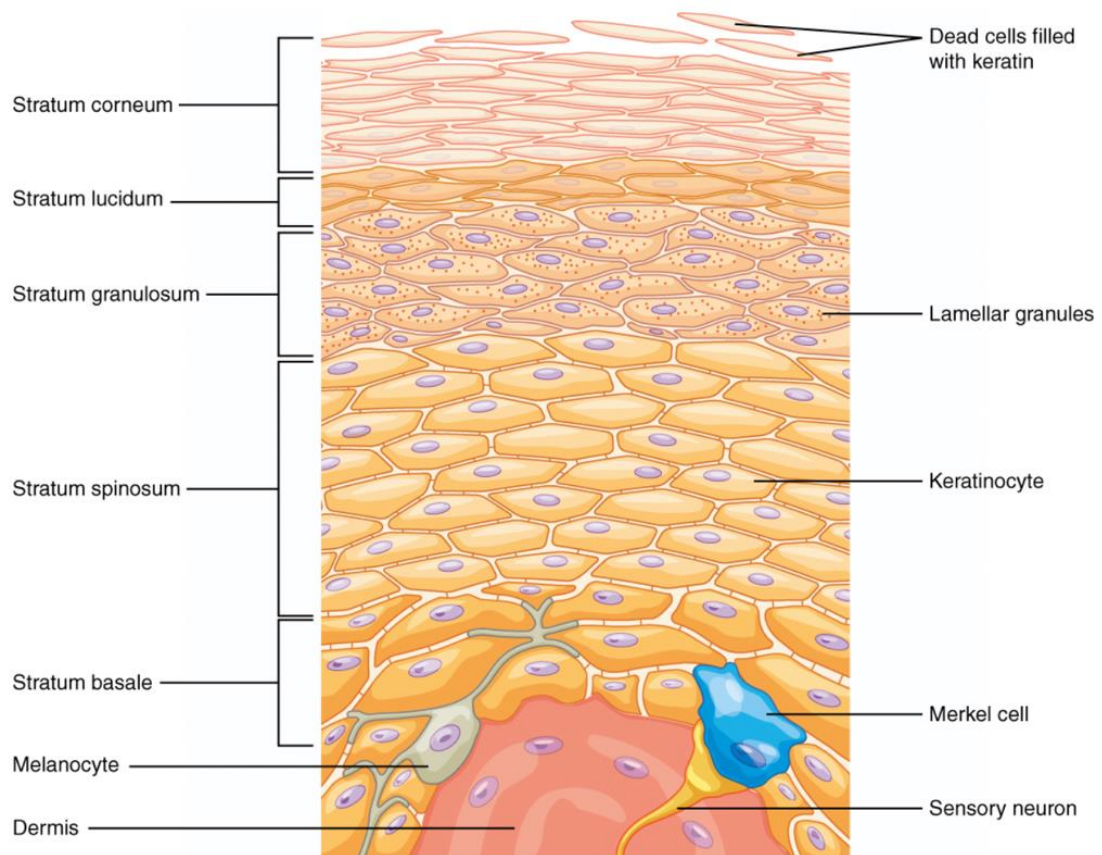


Figure 2 Epidermis layer of human skin.

(i) Stratum corneum

During cell differentiation, the synthesis and accumulation of structural protein (keratin) occur in keratinocytes. When the differentiation reaches its final stage, keratin is assembled into a tight bundle with filaggrin and collapsed into a flattened shape, known as corneocytes. The stratum corneum (SC) is composed of a tightly packed sheet of corneocytes and surrounded by intercellular lipid. Its structure is described as a brick-and-mortar model. The lipid matrix is a bilayer structure consisting of a mixture of ceramide, cholesterol, and fatty acids. Ceramide is the major lipid that provides a rigid structure and plays a critical role in the barrier function, whereas the role of cholesterol is to provide flexibility and fluidity. The main function of SC is to provide mechanical protection to viable epidermis including the dermis and acts as a barrier function to prevent water loss and foreign substances (28, 30).

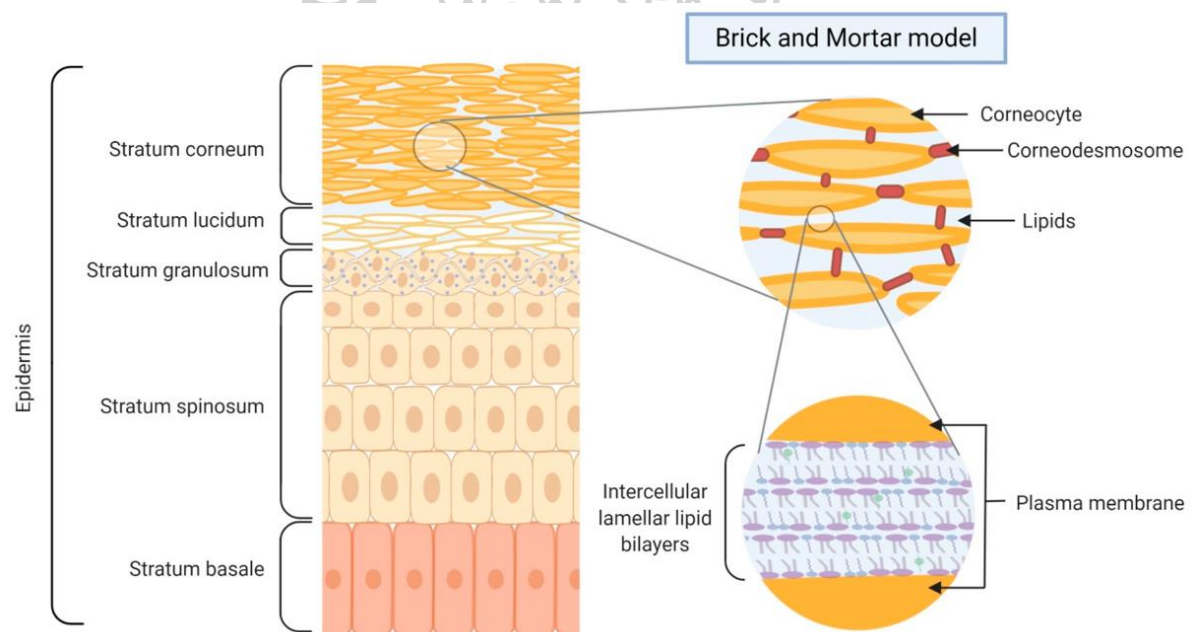


Figure 3 Schematic of epidermal structure (30).

(ii) Stratum lucidum

The stratum lucidum is a thin translucent layer that present only in thick skin locating at palms, soles, and digits. This layer is positioned between stratum corneum and stratum granulosum. This layer mainly acts as a water barrier.

(iii) Stratum granulosum

Stratum granulosum is comprised of viable keratinocytes. The cells in this layer produce fibrous keratin and accumulate keratohyalin as a lamellar granule in their cytoplasm. They are responsible for the synthesis and modification of proteins related to cell differentiation. When these cells die, they leave keratin and keratohyalin behind, leading to the formation of stratum lucidum and stratum corneum (31).

(iv) Stratum spinosum

Stratum spinosum contains approximately 5-10 layers of spiny-shaped keratinocytes tied together with desmosomes. The cells in this layer are generated by cellular division of the stratum basale and become flatter as they are pushed upward. Besides the keratinocytes, Langerhans cells are also located in this layer. They function as immune cells by eradicating bacteria and foreign substances (29, 31).

(v) Stratum basale or stratum germinativum

The deepest layer of the epidermis is the stratum basale (or stratum germinativum), located above the dermis. This is a single layer of basal cells, which is a stem cell precursor of keratinocytes. All epidermal keratinocytes are created from this layer by mitosis and are pushed toward the skin surface. The other cells found in the basal layer are Merkel cells and melanocytes. Merkel cells act as a sensory receptor for touch. These cells are abundant at hands and feet. Melanocyte is the cell that produces skin pigments called melanin. The main function of melanin is to protect cell damage from UV radiation (29).

Dermis

The dermis is the inner layer beneath the epidermis. It is composed of fibroblasts which produce connective tissues (elastin and collagenous fibers) and contains other structures such as hair follicles, blood vessels, lymph vessels, sweat glands, nerves, and sebaceous glands. The dermis can be divided into 2 layers which are the papillary and reticular layer. The papillary layer is the upper layer of dermis that supplies nutrients and oxygen to epidermis. This layer is also responsible for touch sensory and prevents microbial infections. Whereas, the reticular layer composed of dense connective tissue (elastin and collagen fibers) which provide elasticity and tensile strength of the skin. Owing to the water binding capability of collagen, it can keep the skin hydrated. In addition, the reticular layer also includes abundant blood vessels, and nerve supplies (32).

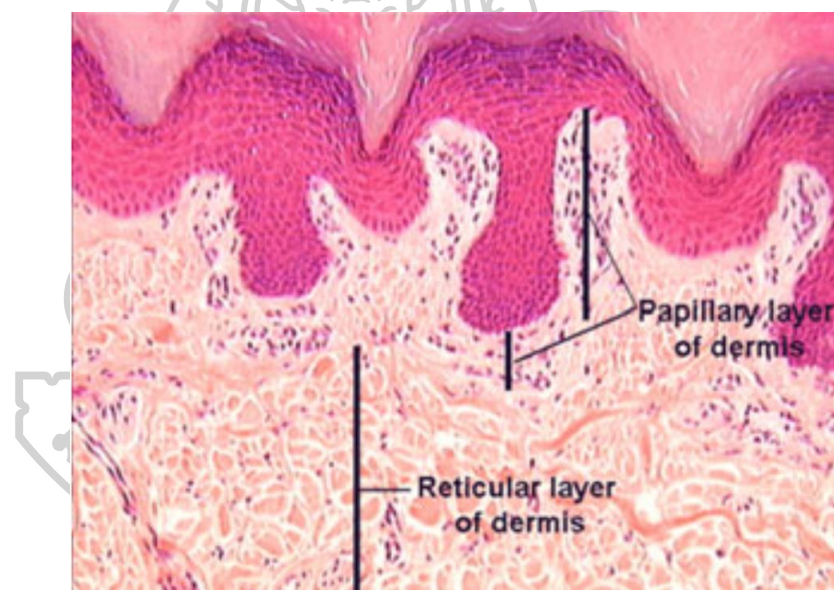


Figure 4 Cross section of human skin representing the layers of dermis (33).

Subcutaneous tissue

The subcutaneous tissue (also called hypodermis) is the layer underneath the dermis and surrounds the skeletal muscles. The layer consists of connective and adipose tissue, which functions as fat storage that supports the integument and provides insulation against external cold and heat (28).

2.1.2 Skin penetration pathway

The transdermal route becomes an eye-catching route for drug administration due to the ease of accessibility. Unfortunately, the penetration of drugs across SC is the most difficult step attributed to the protective barrier of SC. However, the SC allows some molecules with certain characteristics to pass through via two common pathways, which are transepidermal and transappendageal pathways (34).

The transepidermal pathway addresses the conveyance of molecules across the SC by intercellular (paracellular) or intracellular (transcellular) routes. The intercellular route refers to the diffusion of drugs through the lipid matrix between corneocytes thus it is the major pathway for small lipophilic molecules. The intracellular pathway offers the transport of molecules through the corneocytes. This path involves the partition steps from the hydrophilic environment inside the cells to lipid domains between the cells. So, most molecules do not follow this route. The transappendageal pathway is the permeation via sweat glands and hair follicles (also known as transfollicular pathway). The estimated area of this route is only 0.1 % of the total skin surface. This pathway is essential for large hydrophilic molecules (34, 35).

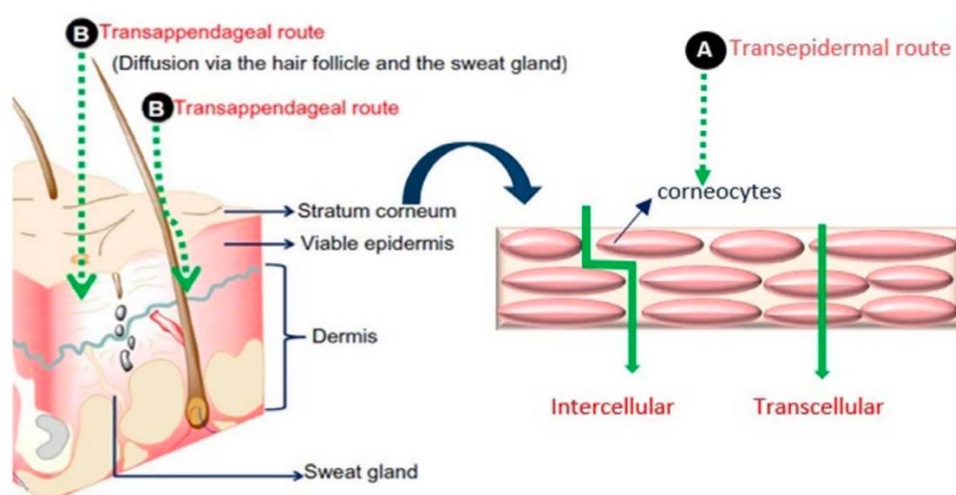


Figure 5 Schematic of skin penetration pathways (36).

2.2 Skin penetration enhancement strategies

The epidermis is the outermost layer of skin that acts as the major barrier to drug absorption. The drugs that can permeate through the skin are commonly those that possess certain properties, e.g., small size (<500 Da), non-ionized, moderate lipophilicity with logP value between 1-4, and a low melting point (< 250 °C). Thus, the skin penetration of drugs that do not align with those properties can be improved using various strategies such as chemical or physical enhancers and nanocarrier systems (34, 37).

2.2.1 Chemical enhancers

At present, a number of chemicals have been found to assist drug delivery across the skin barrier which is called chemical enhancers. These enhancers can disrupt the highly ordered structure of the skin and increase the fluidity of lipid layers, which results in an enhanced skin permeability. The chemical enhancers can be classified into various classes based on their molecular attributes, such as alcohols, fatty acids, esters, hydrocarbons, surfactants, phospholipids, amines, terpenes, and sulfoxides. Potent chemical enhancers are usually composed of a lipophilic chain and a polar head. The hydrophobic chain can create lipid fluidization while the polar head provides hydrogen bonding with the protein structures. However, the major limitations of chemical enhancers are skin irritation and their notable toxicity (37-39).

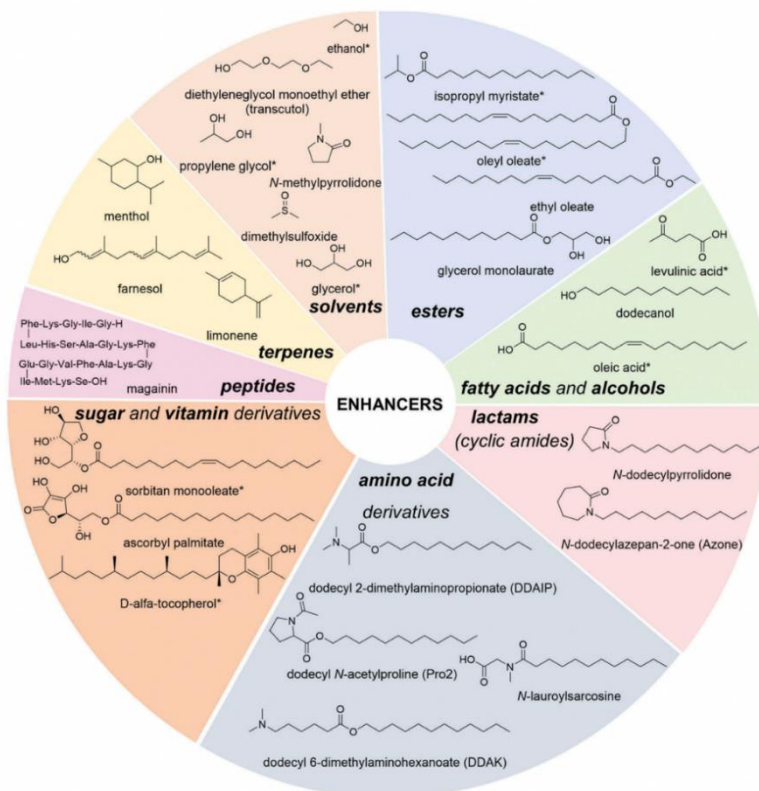


Figure 6 Examples of chemical enhancers in transdermal drug delivery (37).

2.2.2 Physical enhancers

2.2.2.1 Iontophoresis

Iontophoresis has been introduced for the delivery of therapeutic agents since the early 21st century, and it was used to resolve the problems concerning oral administration. This technique involves the electric current as a driving force to push the drugs through the skin (40). Iontophoresis is a technique based on electro-repulsion and electro-osmosis. In the presence of an electric field, ionized drugs are forced to move across the skin by electronic repulsion of the same charge. Positively charged drugs are driven with a positively charged electrode, whereas the negatively charged drugs permeate through the skin using a negatively charged electrode. Electro-osmosis refers to the fluid movement when an electric field is applied. It plays a dominant role in the delivery of neutral particles (41, 42). The electro-repulsive force along with electro-osmosis are utilized for the delivery of many therapeutic agents across the skin, such as proteins, peptides, oligonucleotides, etc.

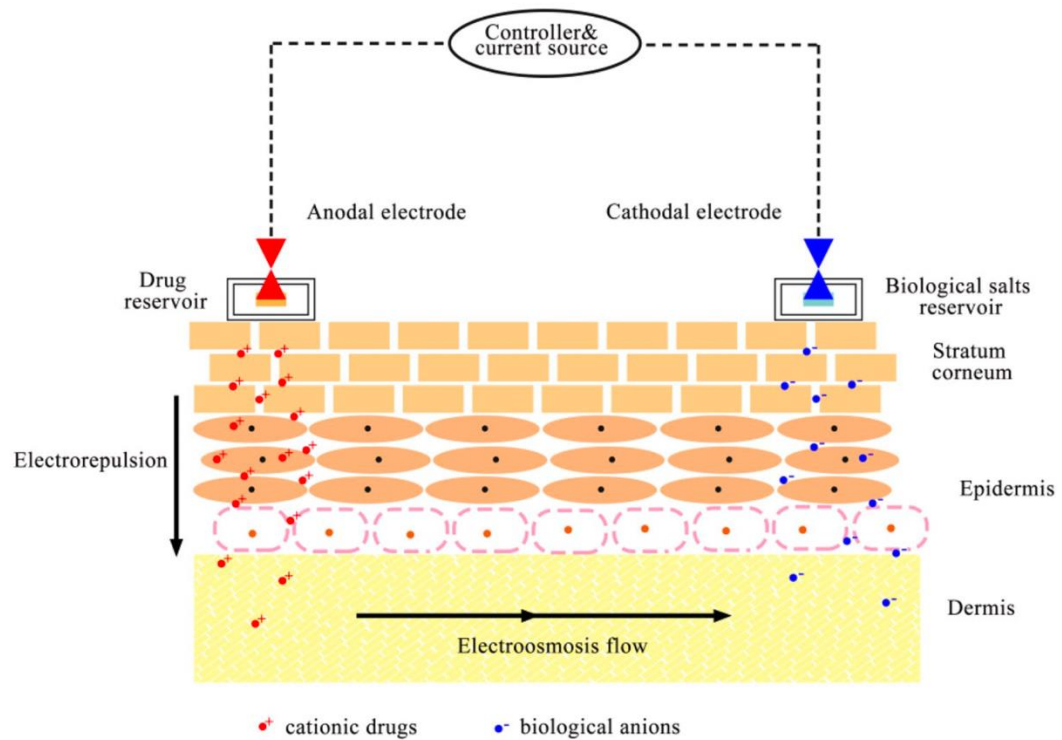


Figure 7 Iontophoresis schematic diagram (41).

Iontophoresis can be combined with other techniques to achieve the synergistic enhancement of transdermal delivery. Li et al. (2021) developed a microneedle array patch combined with the iontophoresis technique as a device for macromolecular drug transdermal delivery. An iontophoresis-driven porous microneedle array patch (IDPMAP) is effective for the delivery of charged drugs. It is non-toxic, non-irritable, and serves as a patient-friendly device due to its portability and self-administration. The results from an *in vivo* study in type I diabetic rats showed that IDPMAP could successfully deliver insulin and effectively maintain the blood glucose level (42).

2.2.2.2 Sonophoresis

Sonophoresis refers to the use of an ultrasound aiming to improve transdermal delivery via a non-invasive manner (43). To set up sonophoresis, the distance between the horn and the skin is provided by a coupling medium, and the skin is placed between mechanical support and an ultrasound source, as illustrated in figure 8. Sonophoresis has been proved to enhance the skin permeability of many therapeutic agents, including drugs and biomolecules (44).

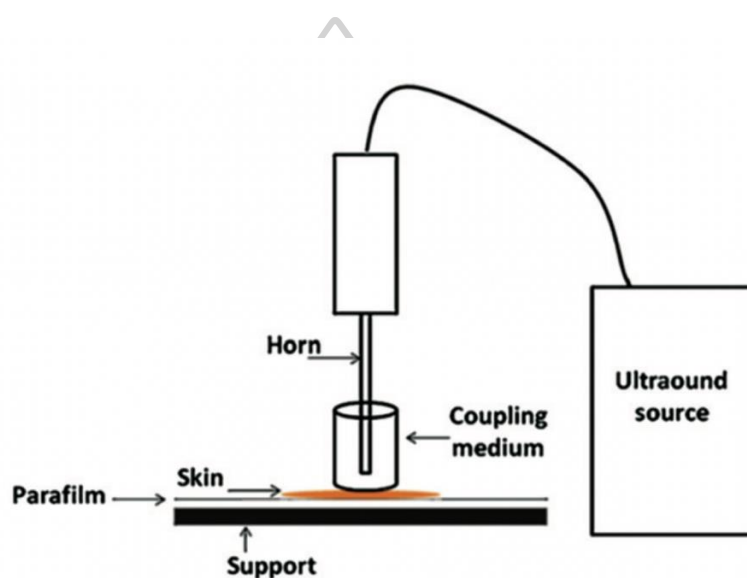


Figure 8 The experimental set up of sonophoresis (45).

Sonophoresis can increase the skin permeability by the heat impact and the cavitation effect on the skin. Yet, the exact mechanism of sonophoresis is not clearly understood. The hypothesized mechanism of sonophoresis involves the cavity generated by the fluctuations and crumpling of liquid bubbles. These bubbles could cause a shock wave or high-pressure microjets that mechanically disrupt the SC (46-48).

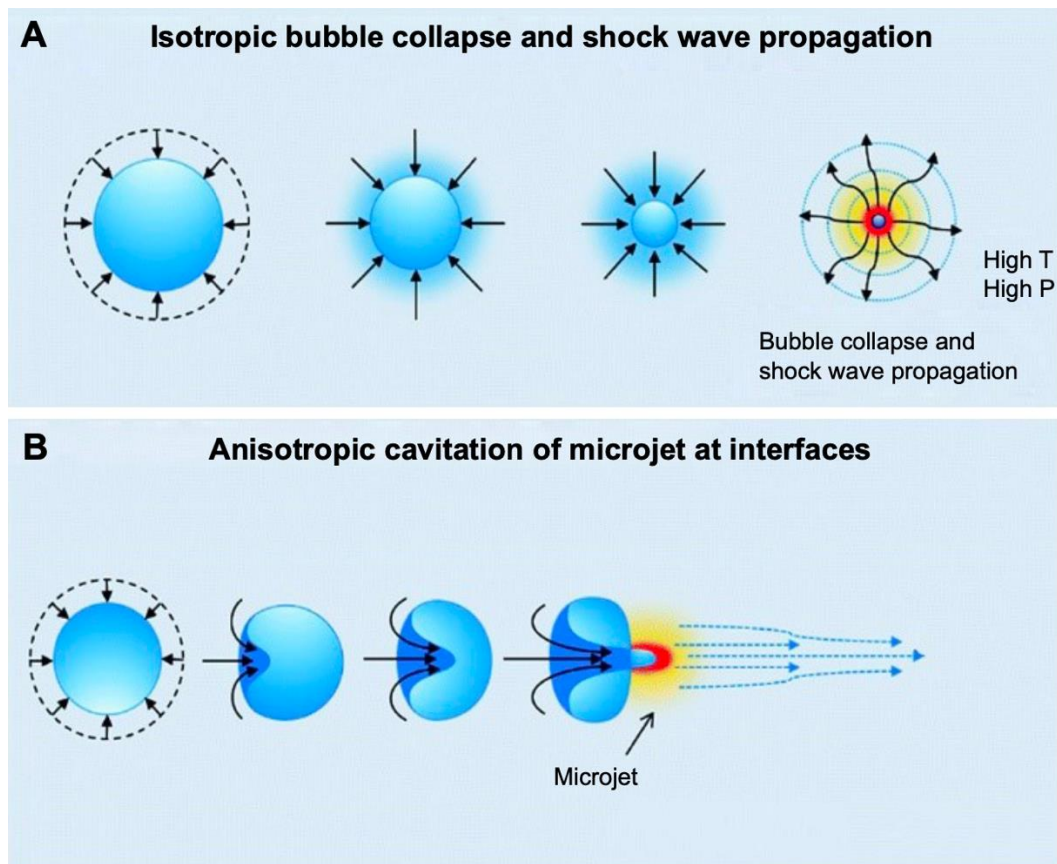


Figure 9 The proposed mechanisms of sonophoresis by the cavitation effect (46).

Vaidya et al. (2020) studied methotrexate (MTX)-contained transdermal patch with sonophoresis pre-treatment. The study demonstrated that the delivery of MTX was significantly improved. In addition, the pharmacodynamics study in rats also indicated the significant recovery from rheumatoid arthritis (RA). Sonophoresis facilitated the diffusion of MTX across the skin by lipid disruption of the stratum corneum. This study suggested that sonophoresis combined with a MTX patch may be a better strategy for RA treatment (48). Another study from Pamornpathomkul et al. (2015) investigated the effect of combining low-frequency sonophoresis with microneedles (MNs). Fluorescein isothiocyanate-dextran, as a model macromolecule drug, was delivered deep into the skin in a greater amount when MNs were combined with the sonophoresis technique compared to each technique individually (49).

2.2.2.3 Electroporation

Transdermal electroporation is the application of a series of short, high voltage electric pulses on the skin to create transient pores in cell membranes. When the voltage of 30-100 V is applied to the skin, its permeability is suddenly increased. The pores created from electroporation are presumed to be sparse, small, and temporary. Pulse length, amplitude, frequency, waveform, and intensity are considered influential factors of electroporation. This technique has been used to enhance the skin permeation of various molecules with different lipophilicity as well as size, including the macromolecules like proteins and nucleotides (50).

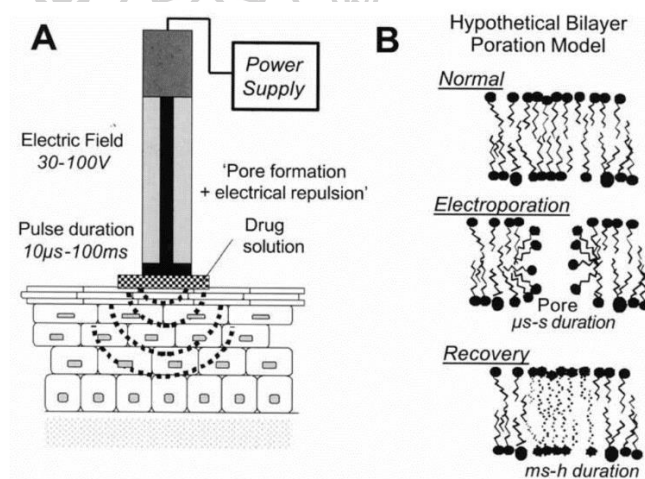


Figure 10 (A) Experimental set up of electroporation device (B) Hypothesized pore forming by electroporation and the recovery (51).

Feng et al. (2017) explored and examined the transdermal delivery of sinomenine for OA and RA treatment both *in vitro* and clinically. Sonophoresis is considered as safe and requires a tiny instrument which is convenient for self-application by patients. The *in vitro* transdermal percutaneous delivery of drugs was significantly increased in mice and pig skin (1.9 - 10.1 and 1.6 - 47.1-fold, respectively), compared to passive diffusion. In the clinical tests, the combination with electroporation offered high drug concentration in synovial fluid (52).

2.2.2.4 Microneedles (MNs)

Microneedles (MNs) have become a new technology for transdermal delivery and have been studied intensively during the last decades. MNs employ micron-sized needles to generate physical path across the SC and deliver the drugs including macromolecules into deeper skin layers without pain. MNs are defined as small needles in micron-scale (25-1000 μm in height) that do not cause pain since they do not reach the nerve endings (53, 54). MN technology is notably superior to conventional percutaneous delivery due to plenty of advantages such as painless, minimal invasiveness, convenience to patient for self-administration, and increase patient compliances (55).

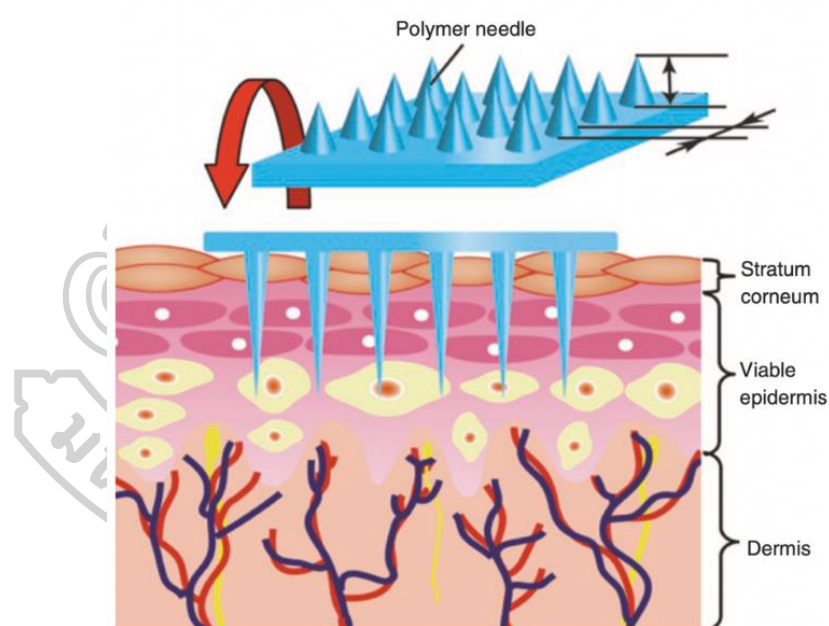


Figure 11 Illustration of skin penetration of polymeric MNs (56).

MNs can be designed with different height and dimension to optimize the delivery across the skin and the tips of MNs can be varied in shape such as rectangular, cylindrical, pyramidal, conical, etc. (53, 57).

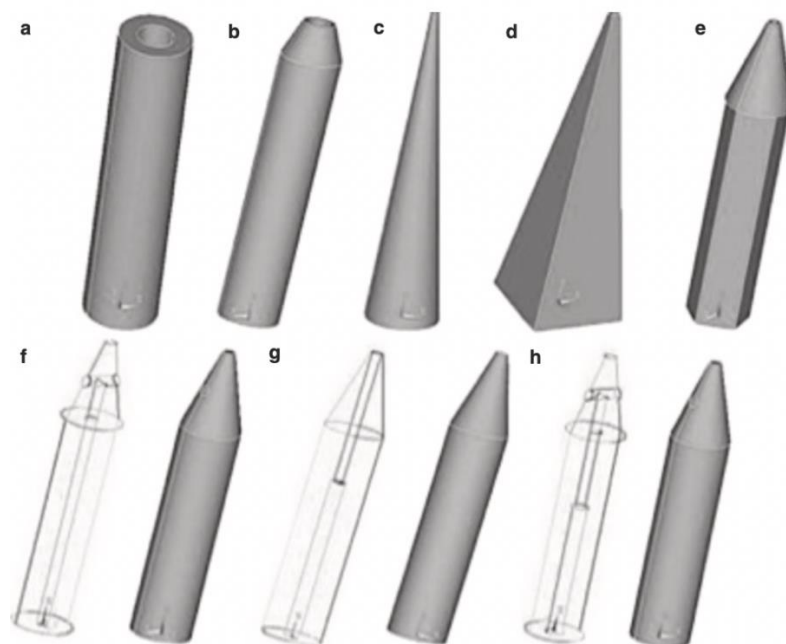


Figure 12 Various shapes of MNs: (a) cylindrical, (b) tapered tip, (c) canonical, (d) square base, (e) pentagonal-base canonical tip, (f) side-open single lumen, (g) double lumen, (h) side-open double lumen (57).

Types of MNs

MNs have been widely developed and at the present. They can be categorized into five major groups based on their design and principle of drug delivery, i.e., solid, coated, hollow, dissolving, and hydrogel forming MNs (58). Each type of MNs has unique properties and designs which provide different advantages (55).

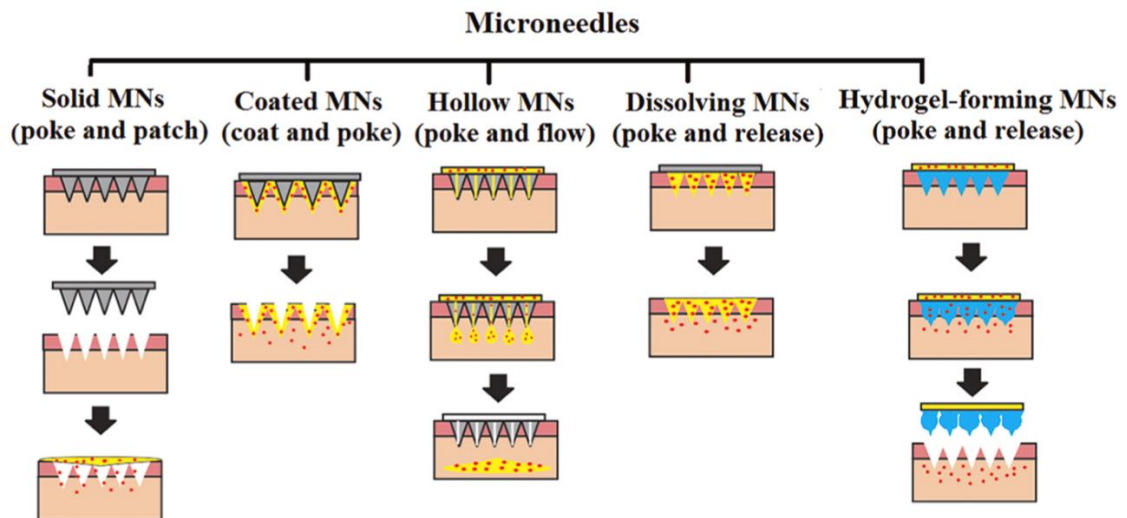


Figure 13 Drug delivery mechanism of various microneedles (58)

(i) *Solid-MNs*

Solid MNs are usually used to pre-treat the skin. The principle of solid MNs composed of two approaches called poke and patch. First, the tips of MNs are inserted into the skin to create microchannels. Secondly, the drug patch is applied and the drug molecules then directly enter the skin through the microchannels (59). Solid MNs can be made of silicon, metal, or polymers (60).

(ii) *Coated-MNs*

Coated MNs are MNs that have needle tips coated by a drug dispersion layer. Its transdermal delivery is based on “coat and poke” principle. By that, the drug is coated onto the MN surface. After the insertion of MNs into the skin, the coated layer is dissolved and the drugs are deposited in the skin. The disadvantage of coated MNs is limited drug loading because the thickness of the coating layer, the needle size, as well as the surface area affects the amount of drug that can be loaded into the coated MNs (61).

(iii) Hollow-MNs

Hollow MNs consisted of empty space in microneedle tips where the drug is filled. Upon the skin insertion, the loaded drug directly flows to the deeper skin layer (lower epidermis and upper dermis). This approach is known as “poke and flow”. Hollow MNs are mostly used to deliver high MW compounds, e.g., vaccines, proteins, DNA, and RNA. The advantage of hollow MNs is the high drug loading capability due to the large empty space inside the needles (21, 62, 63) .

(iv) Dissolving-MNs (DMNs)

DMNs are mostly fabricated from biodegradable polymers or polymers that are able to dissolve in the skin physiological conditions where the drug is entrapped inside the polymers. It is highly attractive due to plenty of advantages such as being easily made, high drug loading, and being safe. The entrapped drug is released after DMNs are inserted and dissolved in the skin, known as “poke and release” approach. The application of DMNs involves only one simple step since the MNs do not need to be removed which makes DMNs a user-friendly method. Moreover, the drug release profile is also controllable for the forming polymers play a crucial role. (58, 64) DMNs are usually made of hydrophilic polymers such as hyaluronic acid (HA), polyvinyl pyrrolidone (PVP), polyvinyl alcohol (PVA), hydroxypropyl methylcellulose (HPMC), and poly(acrylic acid-co-maleic acid) (PAMA) which are commonly combined with structural materials to increase the mechanical strength of the needles (19, 20, 22, 24, 25).

(v) Hydrogel-forming MNs

Hydrogel-forming MNs have recently been developed. Polymers with high swelling capability are used to fabricate this type of MNs. Its mechanism is based on “poke and release” principle. When the MNs are inserted into the skin, they absorb a large quantity of water and swell. The drug is released through the swollen polymer which acts as a rate-controlling membrane (58, 64).

MNs can be made from materials such as metal, glass, ceramic, silicon, and polymer. Due to the solidity of metal, glass, silicon, and ceramic, they can cause pain and swelling at the site of administration. In addition, brittle materials such as silicon could break upon insertion and cause some health concerns. The ideal material for transdermal MN fabrication should provide good mechanical strength concerning the lack of breakage or bending of MN tips during skin insertion, having biocompatible and biodegradable properties, as well as not causing pain or skin irritation (65). Hence, polymers are favored to produce MNs according to their biocompatibility, biodegradability, and inexpensive (66). Polymers are used excessively for the fabrication of dissolving and hydrogel-forming MNs which have proved to be the most effective approach. The major challenge of polymer is its poor mechanical properties which might lead to failure upon skin insertion. However, the combination of two or more polymers with or without additional materials can improve the mechanical strength of MNs (58).

The combination of MNs with micro/nanoparticles for transdermal delivery

The combination between polymeric MNs and micro/nanoparticles has been developed as an advanced approach for transdermal delivery. For instance, insulin microparticles incorporated in MNs exhibited a superior hypoglycemic effect compared to the conventional insulin-loaded MNs (67). In addition, controlled drug delivery through smart MNs with bioresponsive nanoparticles was recently developed. This approach is achieved by the incorporation of the drug molecule into bioresponsive nanoparticles, where the drug will be released under specific physiological conditions such as the acidic environment of the cancer cells or high glucose level in the tissues (68-70).

2.2.3 Nanocarrier systems

Nanoparticles (NPs) are defined as particles with the size range of 1-100 nm and can be classified into various types according to the fabrication materials. For

biomedical purposes, NPs are made of biocompatible materials such as lipids, polymers, metal, etc (9).

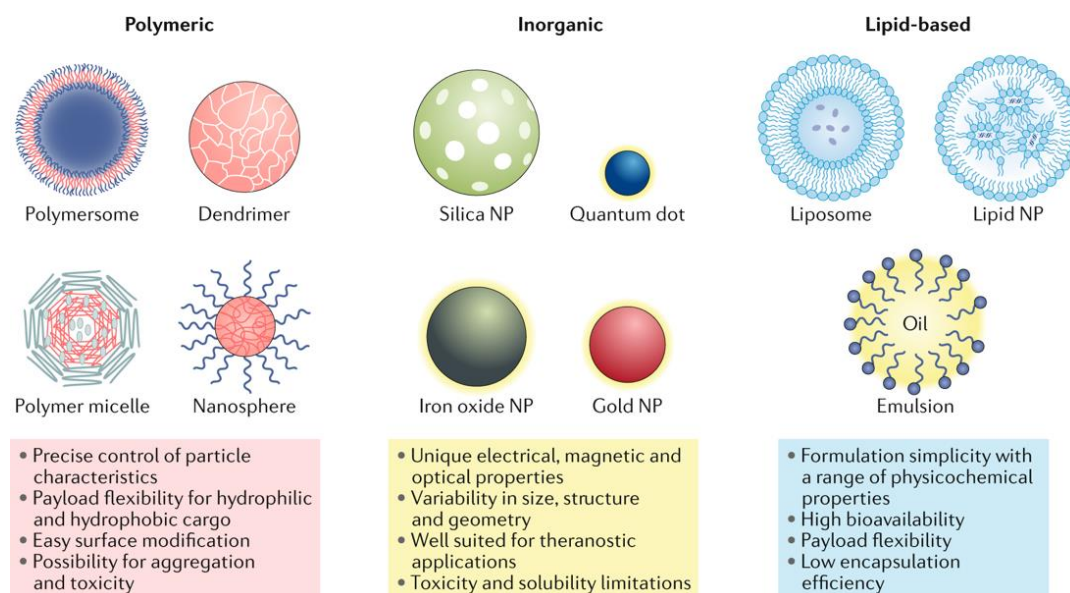


Figure 14 NPs classifications and their features (9).

2.2.3.1 Lipid-based NPs

Lipid-based nano-systems are one of the most studied nanocarrier systems due to their effectiveness and non-toxicity in transdermal delivery. Lipid-based NPs are namely liposomes, niosomes, nanoemulsions, solid lipid particles (SLN), and nanostructured lipid carriers (NLC). However, the major limitations of lipid NPS are low encapsulation efficiency and stability concerns.

Liposomes

In the early 1980s, liposome was considered novel nanotechnology. It was introduced to the cosmetic market in 1986 by Dior and has been widely developed in pharmaceutical products. Liposomes are closed spherical composed of phospholipid bilayers. They can be made from natural or synthetic phospholipids such as phosphatidylcholine, phosphatidylethanolamine, and cholesterol (71). Liposomes are well-known for biocompatible and non-toxic properties which make them appealing

for drug delivery (72). Based on their structure, liposomes can be classified as unilamellar, multilamellar, and multivesicular vesicles (73).

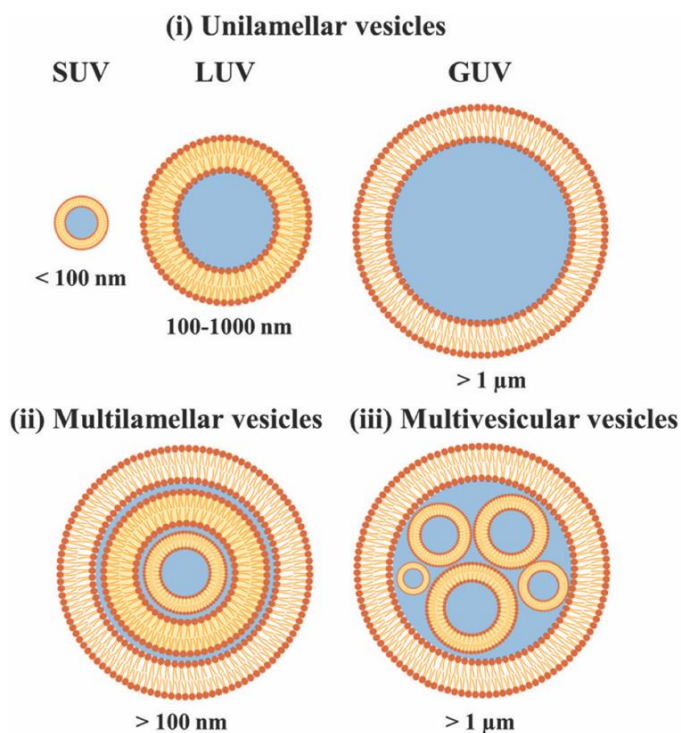


Figure 15 Classification of liposomes based on size and lamellarity (73).

Niosomes

Niosomes are lipid-based vesicles composed of cholesterol and non-ionic surfactants. The vesicular structure of niosomes is similar to liposomes, but the bilayers are assembled from nonionic surfactants. The surfactant that is incorporated in niosomes offers the improvement of drug dispersion, solubility, skin penetration, and sustained drug release. Moreover, niosomes have better stability than liposomes over a long period of time. Niosomes are now widely used in cosmeceutical and pharmaceutical applications (71).

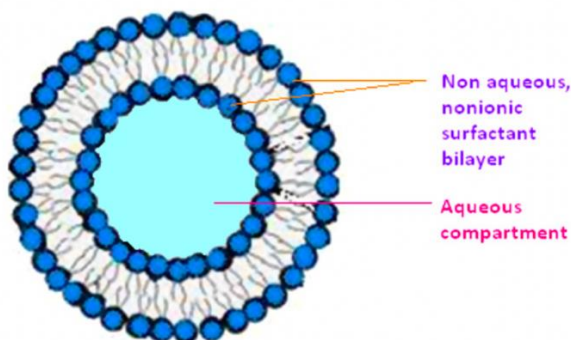


Figure 16 The structure of niosomes (74).

Nanoemulsions

Nanoemulsions are composed of two immiscible liquids that one phase (or internal phase) is dispersed in another (known as continuous phase) and becomes a colloidal particulate system. The droplets are between 10-1,000 nm in size and are stabilized by emulsifiers. Due to the small droplet size, nanoemulsion preparations are transparent. Nanoemulsions can be formed as oil-in-water, water-in-oil, and bi-continuous nanoemulsions. The combination of surfactants and co-surfactants makes nanoemulsions highly stable thermodynamically. This formulation is widely used in pharmaceutical, cosmeceutical, and food industries due to several advantages such as enhanced drug bioavailability, non-toxic, promising physical stability, improved drug absorption, etc (75-77).

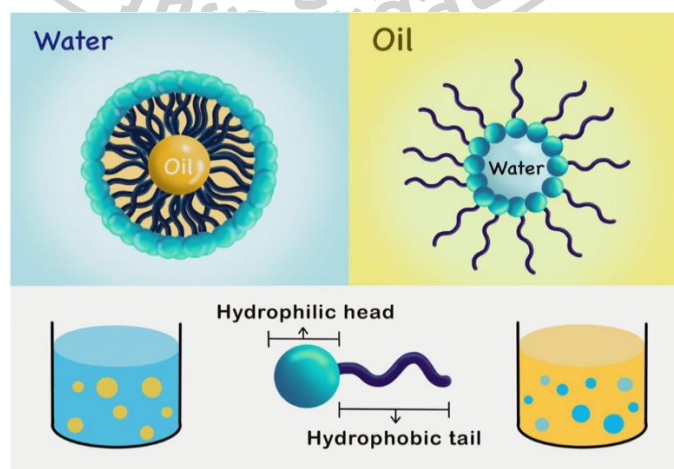


Figure 17 Schematic presentation of oil-in water and water-in-oil nanoemulsions (76).

Solid lipid nanoparticles (SLNs)

The major challenge of most liquid lipid nanosystems is their poor stability. In the late 20th century, solid lipid nanoparticles (SLNs) were promoted as safe and more stable than liposomes. SLNs are composed of a solid matrix surrounded by surfactants. The materials for the preparation of SLNs are waxes, complex glycerides, and triglycerides (78). The replacement of liquid lipid with solid lipid offers several advantages such as controlled drug release, improved stability, high drug loading, compatibility with lipophilic and hydrophilic drug, simple preparation technique, suitable for industrial production, and cost-effective. SLNs are suitable for transdermal, parenteral, as well as pulmonary delivery due to their small size and biocompatibility. However, the drug loading and encapsulation efficiency of SLNs are limited by lipid crystallinity, polymorphism, and drug solubility in lipid (79, 80).

Nanostructured lipid carriers (NLCs)

Liposomes are the conventional and well-known lipid-based NPs, but the use of liposomes is limited because of several drawbacks, such as instability of its vesicular structure and difficulty in scaled-up production (71). SLNs and NLCs were developed as they can overcome the limitations of liposomes. Since SLNs and NLCs consist of lipid matrix in their structure, they are more stable and well-tolerated by the skin (81). However, low drug loading and expulsion of the drug remain the disadvantage of SLNs due to the highly ordered lipid crystallinity. So, NLCs were developed by adding low-melting-point liquid lipid to create an imperfect lipid matrix, which results in higher drug encapsulation and loading capacity (82, 83).

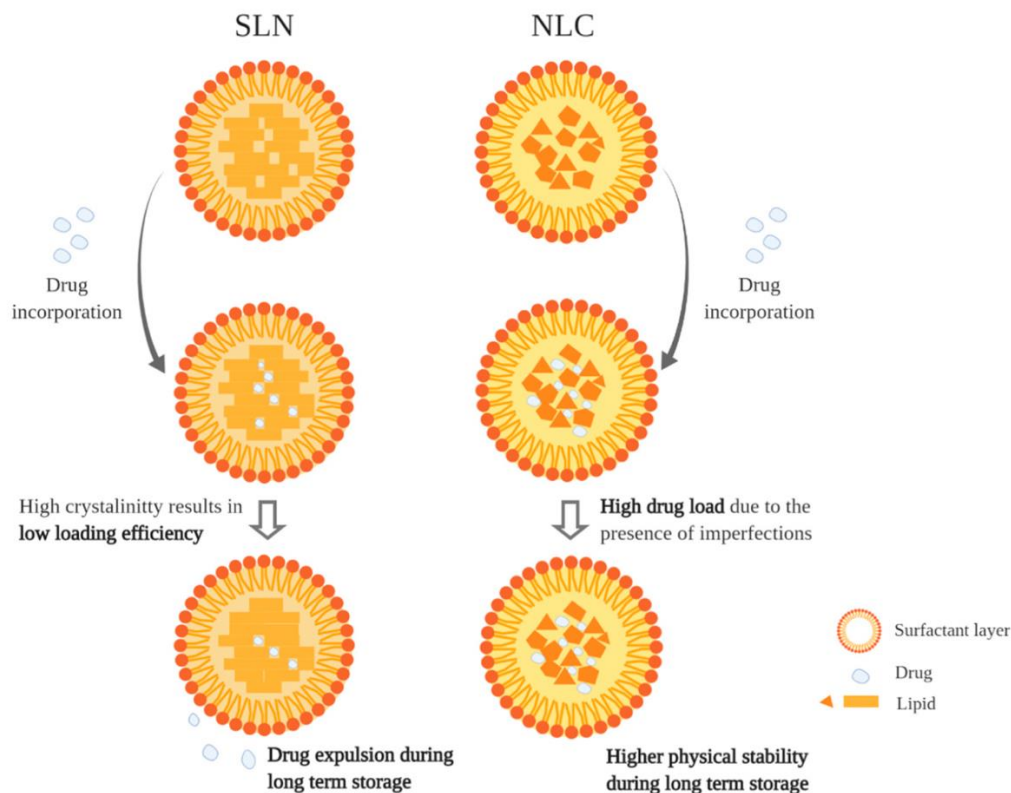


Figure 18 The structure of SLNs and NLCs (83).

2.2.3.2 Polymeric NPs

Polymeric NPs can be made from natural or synthetic polymers. Usually, synthetic polymers offered better consistency and purity. Examples of widely used polymers are poly (lactic-*co*-glycolic acid) (PLGA), polylactides, polyacrylates, and poly (methyl methacrylate). (84) Most polymeric NPs are unable to penetration through the SC due to their large molecular weight, but instead, employ the transfollicular pathway (85).

2.2.3.3 Inorganic-based NPs

Recently, inorganic NPs have been widely used in the field of drug delivery due to their photothermal therapy and bioimaging properties. Some inorganic nanostructures, particularly with a positive charge and lipophilic functionalization, have shown transdermal capability by penetrating through the stratum corneum. Due

to their great stability and high potentiality for surface functionalization, inorganic NPs are getting more attention for transdermal delivery (86). Examples of inorganic particles that have been observed for transdermal applications are gold, silver, and iron oxide. Gold nanoparticles (AuNPs) are widely explored for transdermal delivery for having low toxicity, being biocompatible, allowing surface modification, and particle size controllable attribute (13). Further information about gold nanoparticles will be discussed in the next section.

2.3 Gold nanoparticles (AuNPs)

2.3.1 Introduction and properties of AuNPs

Gold is a shiny yellow solid element that can be found on the ground. It is a valuable metal that is used to make jewelry and coins. However, AuNPs are different from bulk gold. AuNPs were described as small gold particles in a nano-size range (1-100 nm). It is often dispersed in water, known as colloidal gold (87, 88). AuNPs appear in various shades of color which are either red, blue, or purple, depending on the size, shape, and aggregation state, as shown in Figures 19-21. It has been reported that blue or purple shades indicate larger particle sizes that can be caused by AuNPs aggregation compared to red shades. The colloidal gold was discovered in 1857 by Michael Faraday who noticed the change of gold solution color from transparent yellow to a red wine color after mixing AuCl solution with sodium citrate (89).

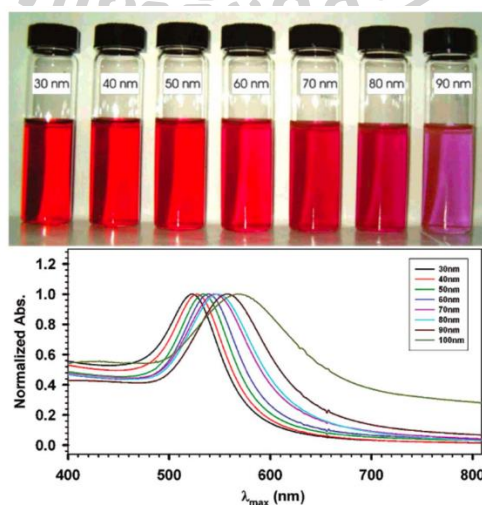


Figure 19 The colors of AuNPs at different particle size (90).

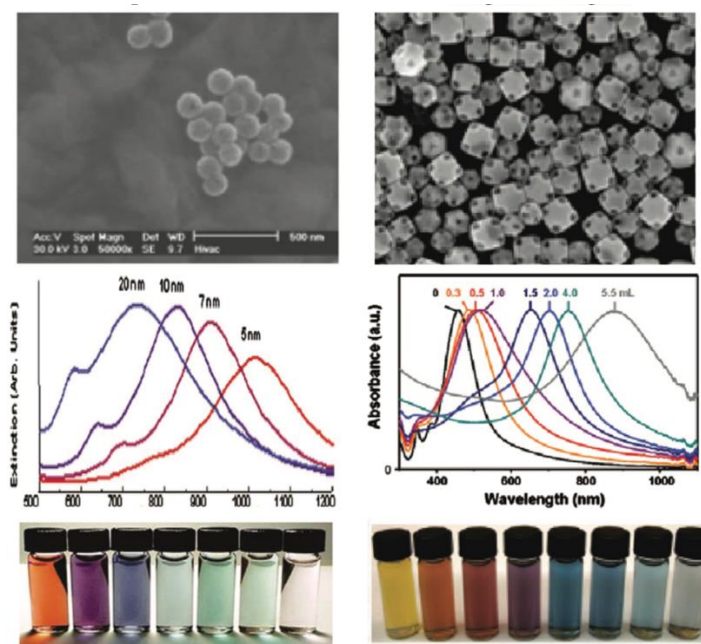


Figure 20 The colors of AuNPs in different shape (91).

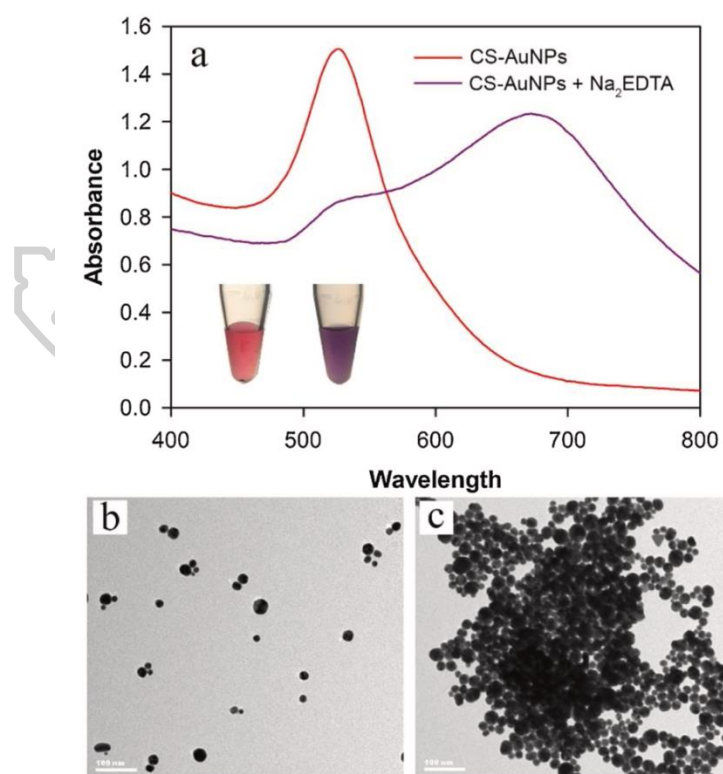


Figure 21 (a) UV absorbance of AuNPs (red line) and the aggregation state (purple line), TEM images of (b) AuNPs and (c) aggregated AuNPs (92).

The structure of AuNPs is composed of three layers: (i) closed packed of gold atoms at its central inner core, (ii) surface gold atom-layer, which usually have different properties from inner gold atoms, and (iii) the ligands that act as the protecting layer (10, 93), as presented in figure 22.

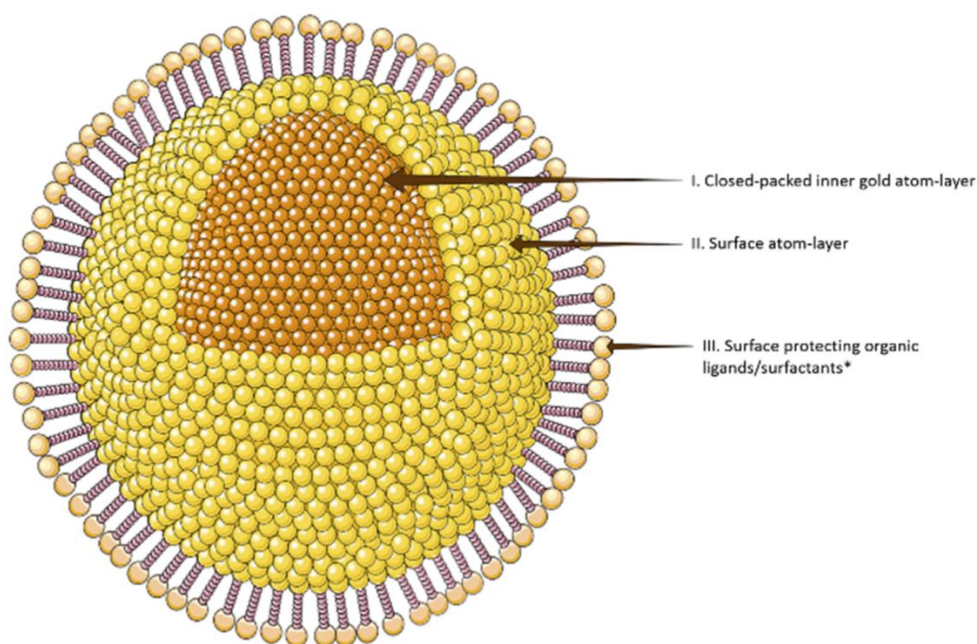


Figure 22 Schematic of a single AuNP structure (10).

The optical and electronic properties of AuNPs are tunable and expressed in different colors. The variations of AuNPs color result from the unique physicochemical properties called surface plasmon resonance (SPR). The SPR effect occurs when gold particles are exposed to light and induce the oscillations of free electrons in the electron cloud. The resonance in the frequency of electromagnetic field (light) and oscillated electrons leads to the absorption of the visible light region (SPR band). The SPR wavelength of AuNPs is approximately 520 nm, indicating the absorption of the green light and the reflection of the red light which causes the red color of gold colloidal solution. In addition, the SPR band shifting is affected by the change in particle size creating different colors of gold colloidal solution. This unique characteristic is useful for the size determination of AuNPs on the basis of SPR absorption (91, 94, 95).

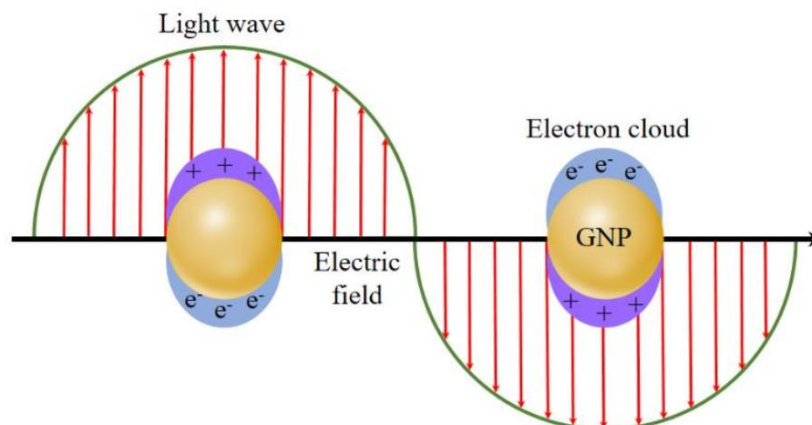


Figure 23 Schematic of surface plasmon resonance of AuNPs (89).

AuNPs become an attractive material in nanomedicines, attributed to the stability, biocompatibility, and ease of synthesis method. (10, 11) Currently, AuNPs are widely used in medical applications, e.g., bioimaging, diagnostic tools, cancer therapy, drug/gene/protein delivery, etc. (88, 96-98).

2.3.2 Synthesis of AuNPs

AuNPs can be synthesized using top-down and bottom-up approaches via different chemical and physical methods. The top-down process is related to size reduction from bulk state gold (Au) to generate AuNPs, whereas the bottom-up synthesis is associated with the chemical reduction reaction to form AuNPs by the assembly of individual Au atoms. (89, 99) The chemical transformation, which is a commonly used method to produce AuNPs, consists of two major steps, namely reduction and stabilization. The reduction process involves the reduction of Au^{3+} to Au^0 by the reducing agents. Chloroauric acid (gold (III) chloride; HAuCl_4) is mostly used as a gold precursor. Examples of reducing agents are sodium citrate, sodium borohydride, polyols, and other electron-rich molecules. The stabilizing agents such as sodium citrate, polymers, and surfactants help to prevent gold particles from agglomeration (11, 99, 100). Furthermore, the cleanliness of the glassware used for

AuNPs preparation is crucial to prevent unwanted nucleation during the synthesis procedures. All glassware, including magnetic stirrers, should be cleansed with aqua regia (a mixture of hydrochloric acid (HCl) and nitric acid (HNO₃) at a ratio of 3:1 by volume) and rinsed with ultrapure water before being dried. After AuNPs preparation, the obtained AuNPs should be kept in the dark and preferably inside a refrigerator to avoid oxidation (101).

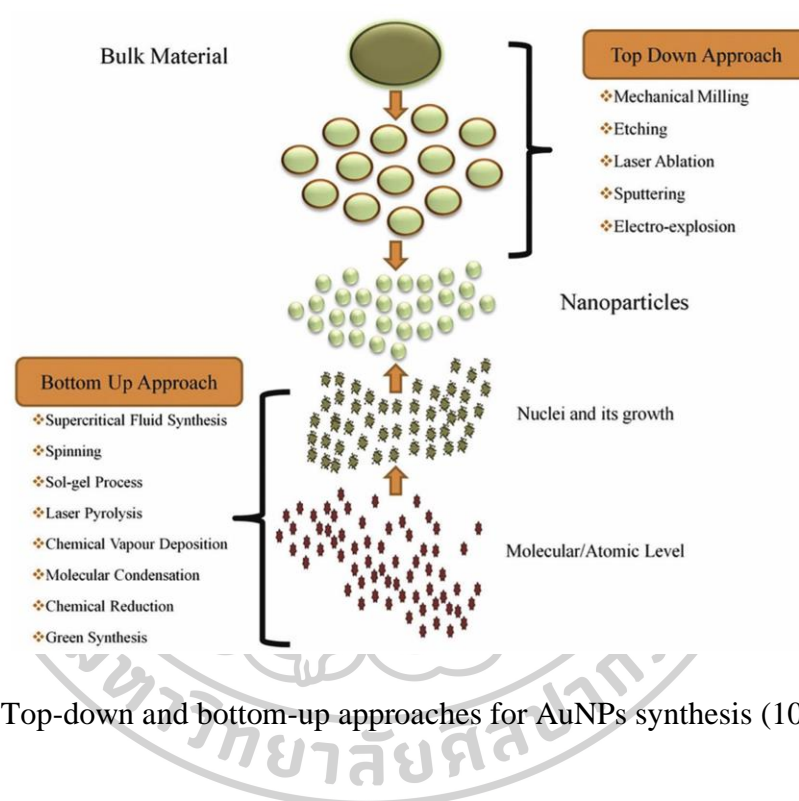


Figure 24 Top-down and bottom-up approaches for AuNPs synthesis (102).

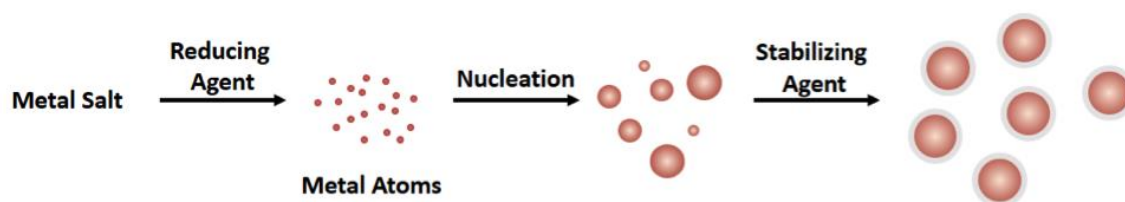


Figure 25 Bottom-up approach using chemical reduction

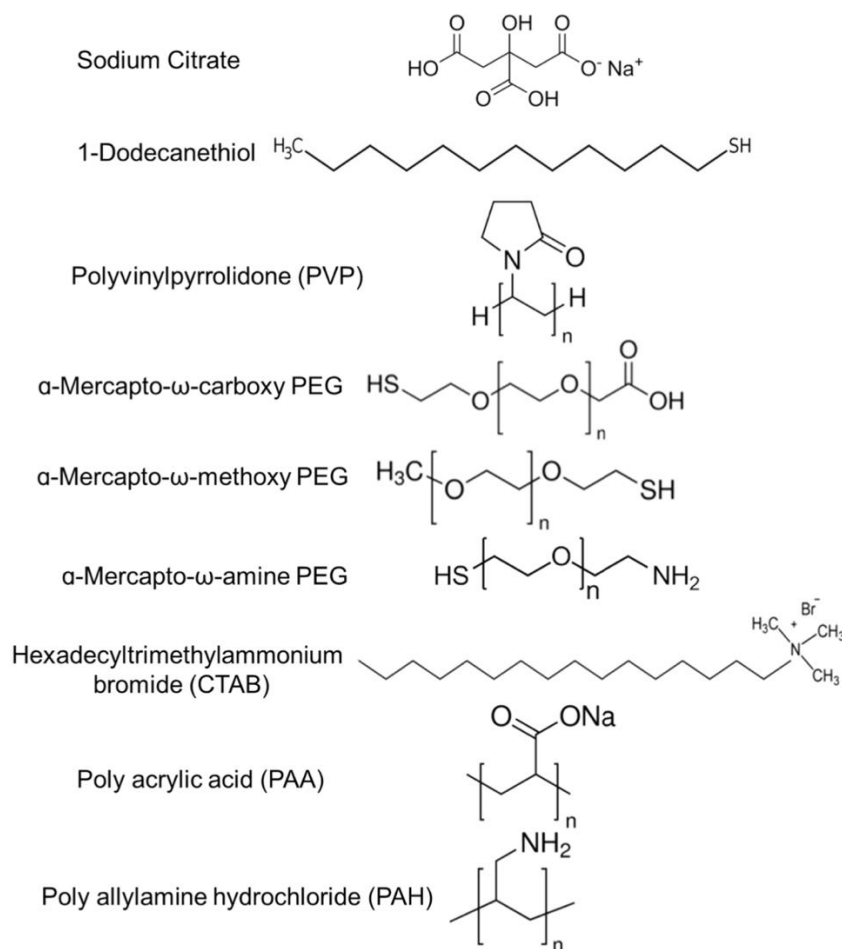


Figure 26 Representative of stabilizing agents of AuNPs (100).

Turkevich method

The classical method of AuNPs synthesis was first reported by Turkevich and his coworkers in the 1950s. In this method, colloidal gold was formed through a chemical reaction between gold (III) chloride, as a precursor, and sodium citrate ($\text{Na}_3\text{C}_6\text{H}_5\text{O}_7$), as both reducing and stabilizing agents (103). Briefly, gold (III) chloride solution was heated to the boiling point, and sodium citrate was added. The transition of Au^{3+} to Au^0 was visualized by the color change from yellow to a red wine solution (89, 104). This method resulted in spherical shaped-AuNPs with a narrow size distribution (10).

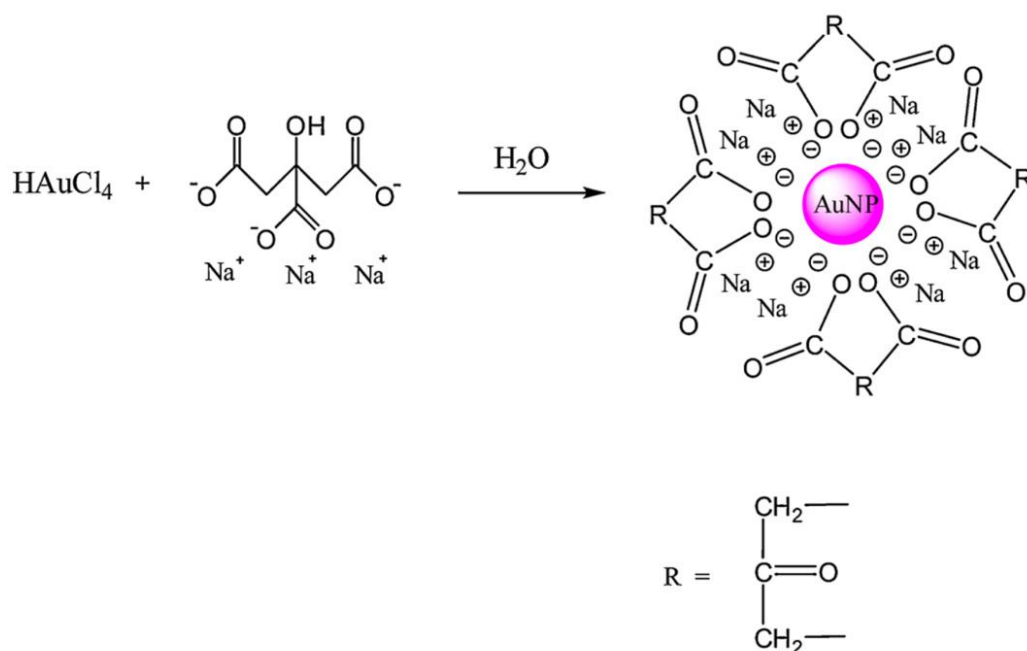


Figure 27 Synthesis of AuNPs by Turkevich method (105).

Brust-Schiffrin method

Another well-known method to produce spherical AuNPs is the Brust-Schiffrin method, discovered in 1994. This method involved the synthesis in a two-phase system, the aqueous and organic phases. Gold ions were transferred from the aqueous to the organic layer, and tetraoctylammonium bromide (TOAB) was used as a phase-transfer agent. This step was followed by the reduction and stabilization using sodium borohydride (NaBH_4) and dodecanethiol, respectively. AuNPs obtained from this method have narrow size distribution and are highly stable due to the alkanethiol capping (101, 104, 106-108).

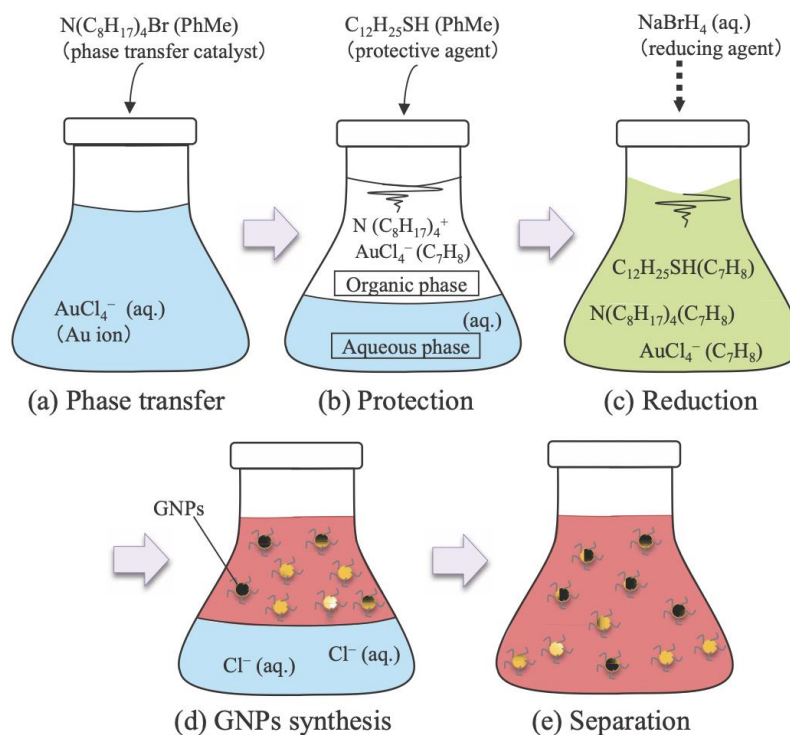


Figure 28 Schematic of Brust-Schiffrin method for AuNPs synthesis (107).

Other methods used for AuNPs synthesis: green synthesis

Conventionally suggested AuNPs synthesis involves hazardous chemicals. The green synthesis methods have been proposed as a safe and environmentally friendly approach. Biological resources, such as plants, microorganisms, biomolecules, and polysaccharides, have been utilized for AuNPs synthesis (10). Chitosan is a natural polymer extracted from crustaceans (e.g., crab and shrimps). It is a derivative of chitin composed of *N*-acetylglucosamine and glucosamine units. Chitosan is considered a green polymer because it is non-toxic, biocompatible, and biodegradable (109, 110). The synthesis of AuNPs using chitosan has been reported by many researchers. The polar functional groups of chitosan can reduce the gold precursor, tetrachloroaurate (AuCl_4^-), to zero-valent state gold via charge transfer, and its amino groups play a key role in the stabilization of AuNPs. In conclusion, chitosan

is functioned as both a reducing and stabilizing agent for the synthesis of AuNPs (111).

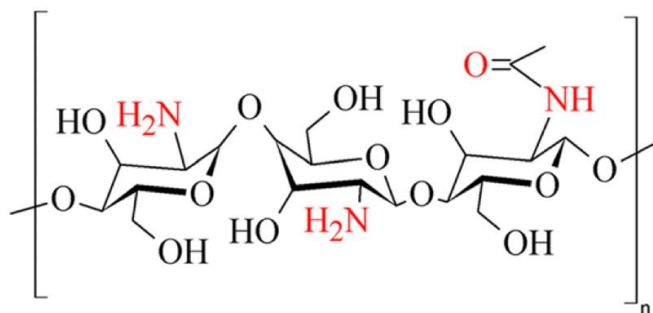


Figure 29 Chemical structure of chitosan (112).

Recently, a novel technique of chitosan capped AuNPs synthesis using microwave radiation has been introduced as a green synthesis method. This method is rapid, simple, and requires fewer and non-toxic reagents compared to other methods. In brief, HAuCl_4 aqueous solution is mixed with the chitosan solution in diluted acid in a glass reaction tube. The mixture is subsequently placed in a microwave synthesizer and irradiated using a fixed temperature. As the synthesizer is operating, gold ions are being reduced to the zero-valence state and stabilized by chitosan. The reaction completion is indicated by the color change of the solution from clear light yellow to red wine. Lastly, the resulting AuNPs solution is immediately cooled in an ice bath (92).

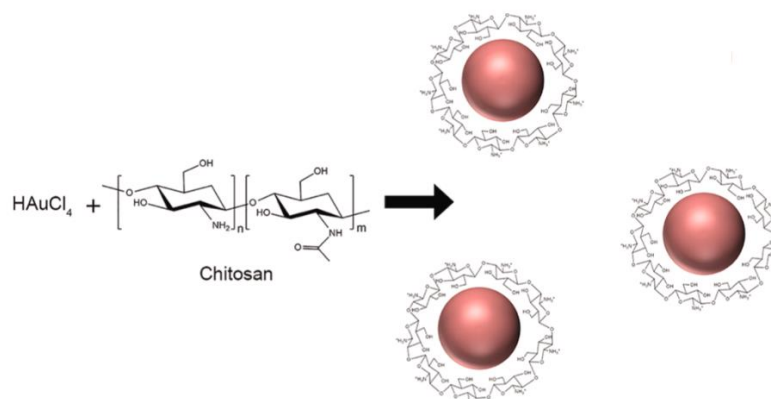


Figure 30 Synthesis of chitosan-capped AuNPs (92).

2.3.3 Application of AuNPs

AuNPs are widely used in nanotechnology and nanomedicines because they are the most stable metal NPs with biocompatible and relatively inert properties in biological systems. In medical applications, AuNPs can be used as diagnostic tools, drug carriers, biosensors, and biomedical nanodevice (Figure 31 and 32) (88, 113).

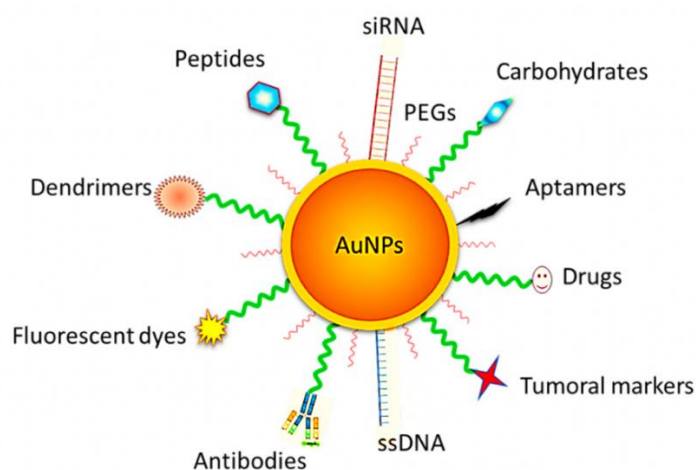


Figure 31 Schematic illustrating various surface functionalities employed in AuNPs (114).

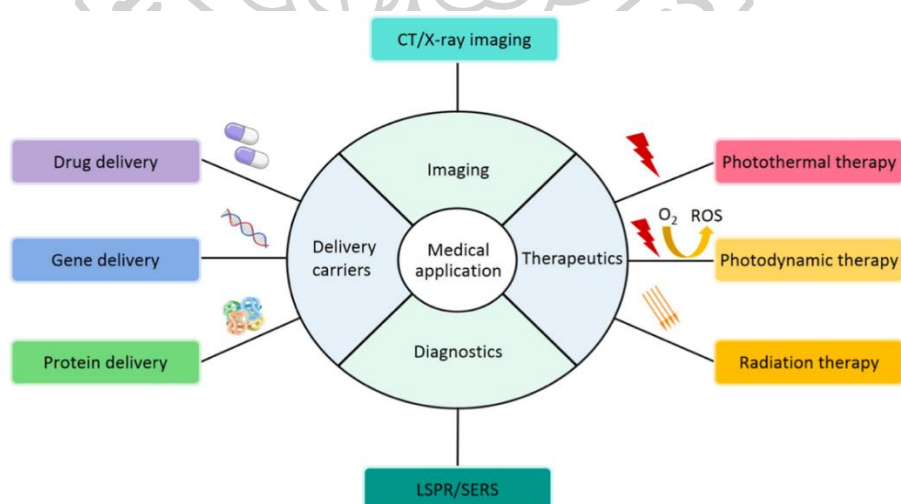


Figure 32 Medical application of AuNPs (88).

2.3.3.1 AuNPs as a delivery carrier

AuNPs offers the delivery of DNA/RNA, proteins, peptides, antibodies, enzymes, polymers, fluorescein dyes, and drugs by surface functionalization of the NPs (Figure 33). These molecules and biomolecules can be conjugated with AuNPs through non-covalent and covalent conjugation. The non-covalent interaction is a simple way to attach molecules to the gold surface using specific binding affinity, hydrophobic and electrostatic interactions. These interactions are reversible and the drug molecules are easily released; thus, it is utilized in drug delivery area (95, 115).

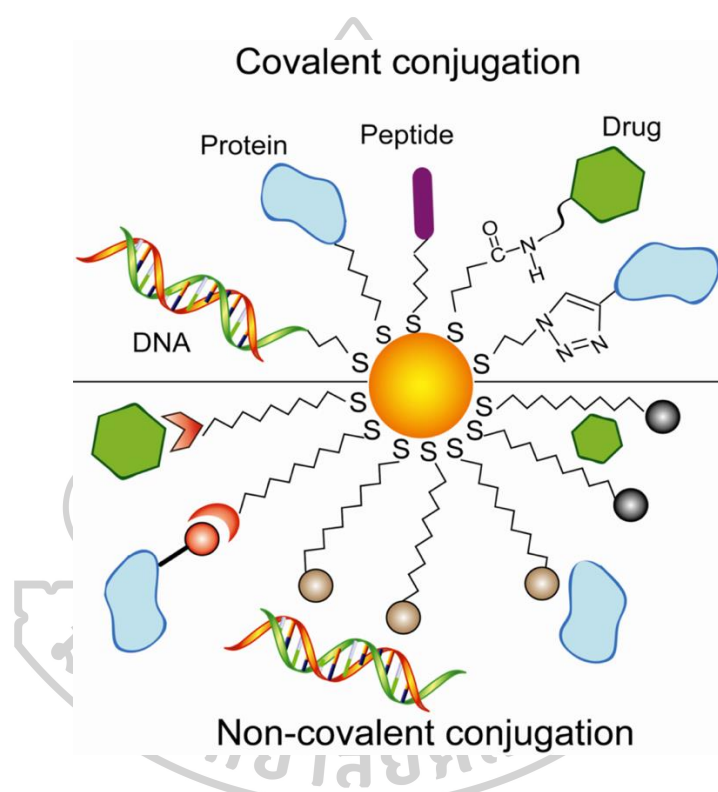


Figure 33 Conjugation strategies of AuNPs through covalent and non-covalent conjugation (95).

AuNPs as drug delivery

AuNPs are widely studied for drug delivery, particularly, for cancer therapy. Chemotherapy is a conventional and commonly used method of cancer therapy. Traditional drug administration via oral or intravenous route supplies the chemotherapeutic agents throughout the whole body, which only a small percentage

of drugs would reach the tumor site and potentially leads to unwanted side effects (116). By that, the drug delivery system becomes a promising tool for anti-cancer drug delivery in order to increase the efficiency of drug conveyance to target organs (117). AuNPs demonstrated the potential for anti-cancer drug delivery for the ease of surface modification. Additionally, the drugs can be conjugated with AuNPs via chemical bonding and released at the target site (118). F Du et al. (2018) reported that lower amount doxorubicin was found in mice plasma when given as AuNPs conjugated doxorubicin (Au-Dox) compared to conventional doxorubicin administration. Moreover, mice treated with Au-Dox had no histopathological lesions, whereas the observable lesions were found in mice treated with an equivalent dose of doxorubicin, indicating reduced toxicity in normal cells (119). In addition, Wójcik et al. (2015) also demonstrated that glutathione-stabilized AuNPs conjugated with doxorubicin (Au-GSH-Dox, Figure 34) resulted in a higher cytotoxic effect toward fibrosarcoma cells compared to free doxorubicin. Hence, Au-GSH-Dox could be a new strategy to improve the efficacy of anti-cancer drugs (120).

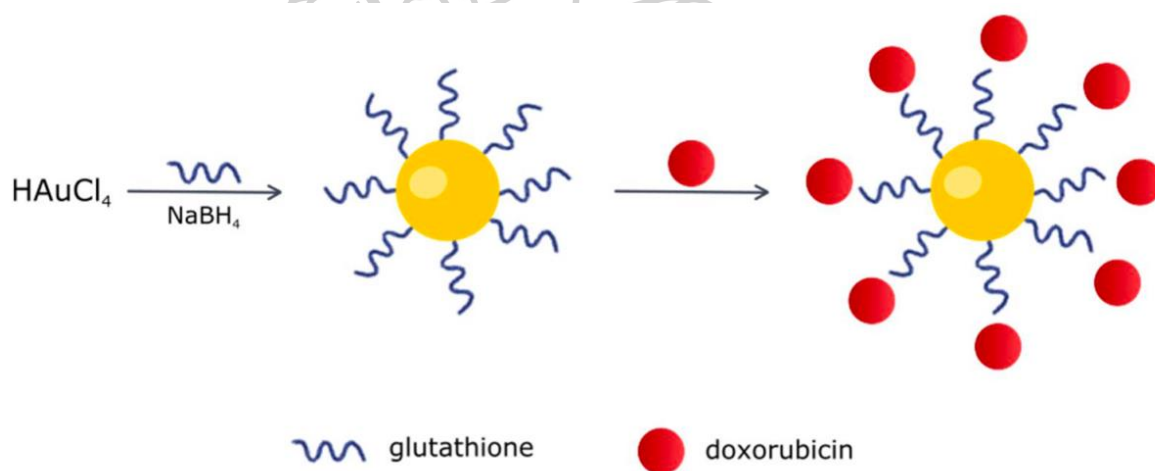


Figure 34 Schematic for Au-GSH-Dox (121).

AuNPs as gene delivery

The use of DNA or RNA to cure or prevent the disease has gained more attentions in the past decades, known as gene therapy. The conventional delivery of nucleotides is as viral vectors, which the activation of host immune

systems and the reduction of gene therapy efficiency are being concerned. Non-viral vectors, e.g., metal-based nanoparticles, has been used to solve the problems related with viral-vectors (122). Klebowski et al. (2018) revealed that AuNPs is an interesting carrier for gene delivery since it can prevent the degradation of nucleotides by the nuclease enzyme (123). CRISPR is one of the most interesting gene studied in gene therapy because of its gene editing capability. CRISPR technology is moving rapidly from basic science to clinical application. The current delivery of CRISPR required electroporation and complicated virus transduction. Recently, Shahbazi et al. (2019) presented a CRISPR nanoformulation using AuNPs (AuNPs/CRISPR, Figure 35) as a promising tool for gene delivery due to the avoidance the lysosomal degradation as well as efficient transportation into the nucleus of human blood progenitors without significant toxicity (124).

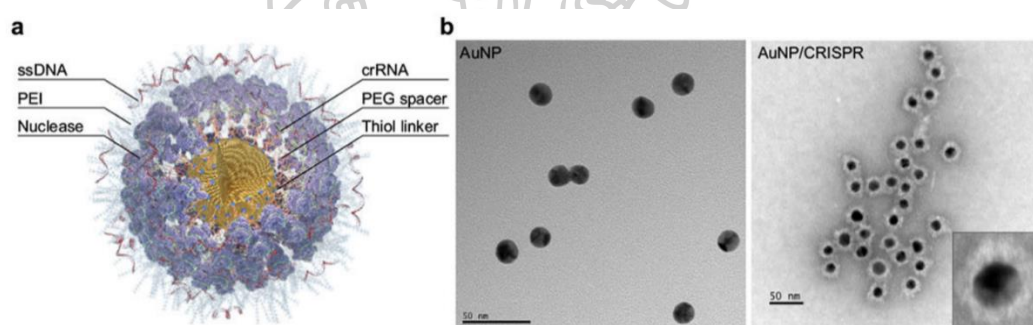


Figure 35 (a) Schematic representation of AuNP/CRISPR nanoformulation (b) TEM images of AuNP and AuNP/CRISPR nanoformulations (124).

AuNPs as protein delivery

The delivery using AuNPs is not limited to drug and gene only, AuNPs are also reported as a good candidate for protein carriers. Precision medicine, including antigen-based immunotherapy, has become a novel approach for the treatment of complex diseases. Type 1 diabetes has been recently considered to involve with immune disorders. With the aim to be used as a treatment of autoimmune type 1 diabetes, AuNPs coupled with human proinsulin peptide have been developed and currently being studied in the patients (125). Previously, Joshi et

al. (2006) obtained insulin-functionalized AuNPs (Au-insulin NPs) for the treatment of diabetes in rat model. AuNPs in this study were covered with non-toxic biopolymer which provided effective insulin delivery via transmucosal route (126). In addition, AuNPs have been proposed for vaccine delivery which featured as both drug delivery carriers and adjuvants. Functionalized AuNPs were easily endocytosed by antigen presenting cells and required lower antigen dosage (127). Besides, the applications of AuNPs for cancer therapy includes the delivery drugs, genes, and proteins (Figure 36) (93). Rathinaraj et al. (2015) successfully developed Herceptin[®] immobilized on AuNPs (GNP-Her). The results from cell culture experiment and confocal laser scanning microscope revealed that GNP-Her was bound precisely to breast cancer cell membrane and led to the cells death (128).

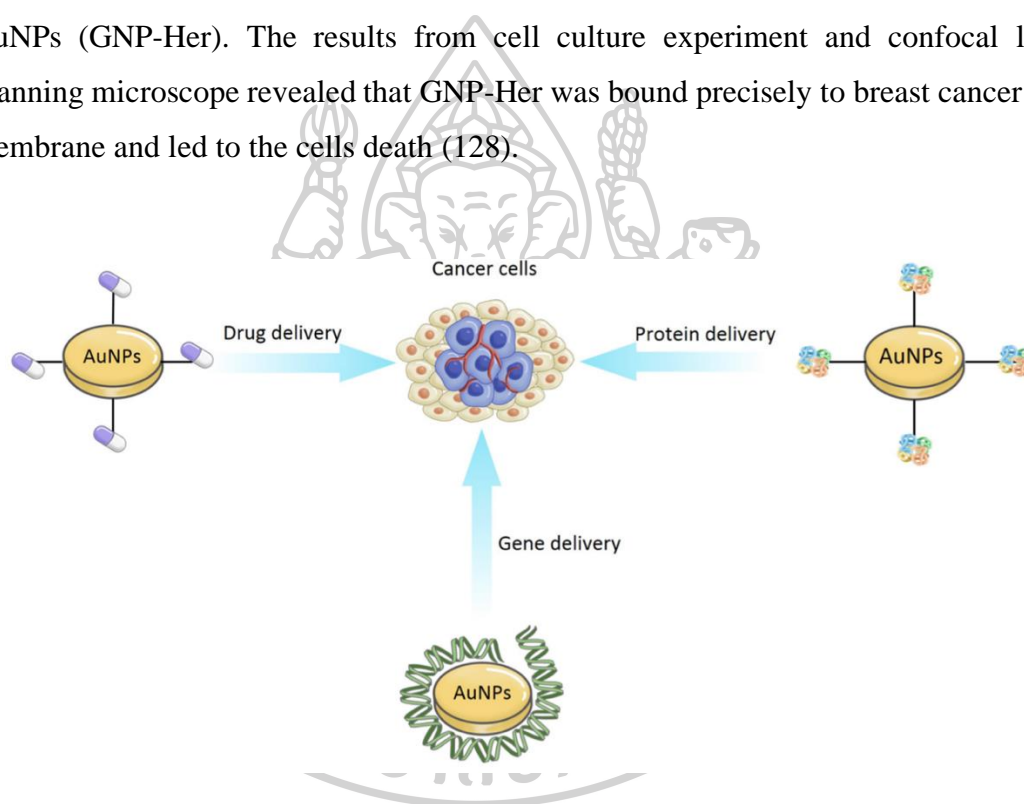


Figure 36 The application of AuNPs as a delivery carrier for cancer therapy (88).

2.3.3.2 AuNPs for diagnostic, biosensing, and imaging

Diagnostics are important examinations in medical sciences to overcome patients' illness. However, some diagnostic methods have low sensitivity and inaccuracy. Nanotechnologies are applied to improve the specificity and sensitivity. With the unique properties of AuNPs including the surface-enhanced Raman scattering (SERS), surface plasmon resonance (SPR), and high surface modification, AuNPs became a great nanomaterial for diagnosis (biosensors and bioimaging). The

SPR phenomenon of AuNPs explained that the NPs can absorb the light energy and generate resonance with the peak in the visible region (~500 nm or 800-1200 nm) (129). For example, AuNPs have been applied for the diagnosis of heart problems such as myocardial infarction (MI). SPR biosensors-based AuNPs have shown to detect the MI biomarkers with high selectivity and sensitivity, which is useful for the early detection of the disease and allowing an appropriate prognosis on the disease severity. (130) The polymerase chain reaction (PCR) has been widely used for diagnostic. Ei et al. (2016) developed AuNPs-assisted PCR technique using citrated-capped AuNPs. The results showed that the AuNPs-assist technique was highly sensitive, efficient, and specific for detection of equine herpes virus 1 (EHV-1) compared to the conventional PCR (131). AuNPs are also applicable for computed tomography (CT) and x-ray imaging since they are qualified as a contrasting agent (Figure 37). Currently, iodinated molecules are being used as conventional contrasting agent due to their exclusive x-ray absorption coefficient. But their limitations are comprised of rapid renal clearance, short imaging times, and toxicity. Therefore, novel materials were need to be explored, and AuNPs showed to be good candidate for this role. Because of the SPR effect, AuNPs can enhance x-ray absorption and convert the light energy to heat (132). AuNPs are superior to iodinated compounds in terms of safety, higher electron density, higher x-ray absorption coefficient, and simple synthesis method (133, 134). AuNPs were able to migrate and accumulate at the target sites, allowing the tracking and visualizing of the cells (135, 136).

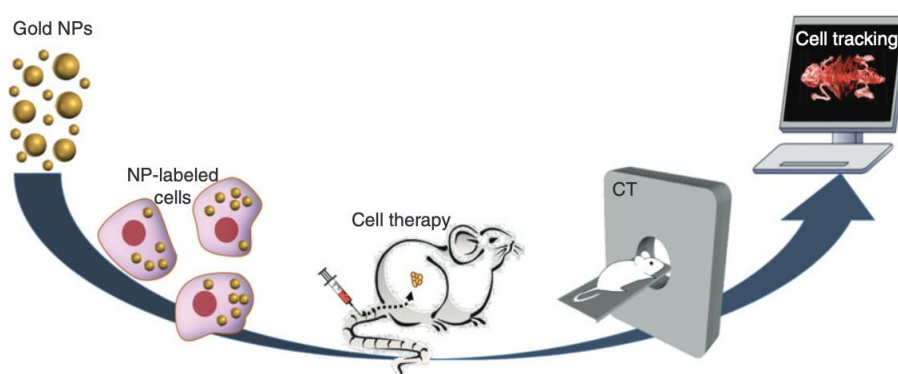


Figure 37 Schematic of in cell tracking by AuNPs and CT imaging (135).

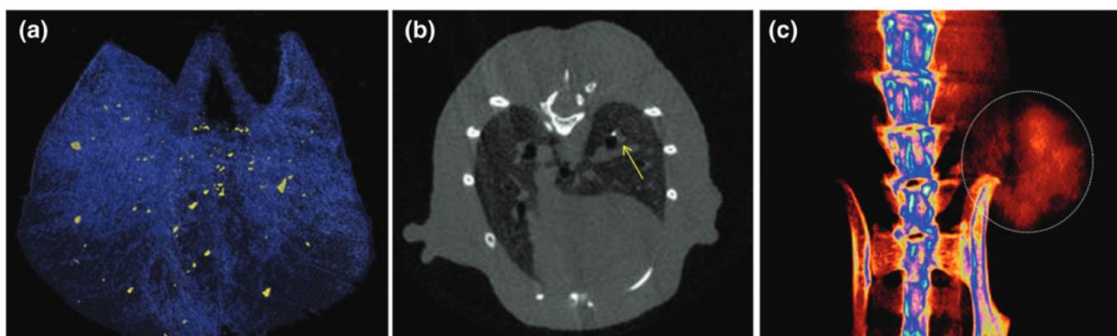


Figure 38 CT scans demonstrated AuNPs migration (a) 3D CT image of AuNPs accumulation in the lungs (b) 2D CT image of AuNPs in lung (c) Accumulation of AuNPs in tumor (135).

2.3.3.3 AuNPs for therapy

Owing to AuNPs capability to convert light to heat energy, they can be used in the cancer treatment via photothermal therapy (PTT) (also known as optical hyperthermia or thermal ablation). In details, AuNPs were injected, then accumulated in the tumor site. When accumulated, AuNPs were exposed to the radiation from light energy which would be converted into heat energy and caused the damages to the cancer cells (137, 138). Additionally, photodynamic therapy (PDT) is another strategy of light therapy involving oxygen molecules. Its principle involved the absorption of AuNPs, as a photosensitizer, by tumors. Once AuNPs have exposed to the light, the reactive oxygen species (ROS) are generated by energy transfer from the light via AuNPs and results in cells death (139, 140). Furthermore, AuNPs have been studied for radiation therapy (RT), which encompasses with the ionizing radiations (e.g., X-rays) and the production of ROS. AuNPs have been reported to enhance the ROS production by their surface electrons and led to the destruction of tumor cells. With the advantages of higher ROS production, total dose of radiation can be reduced ensuing reduced side effects (141, 142).

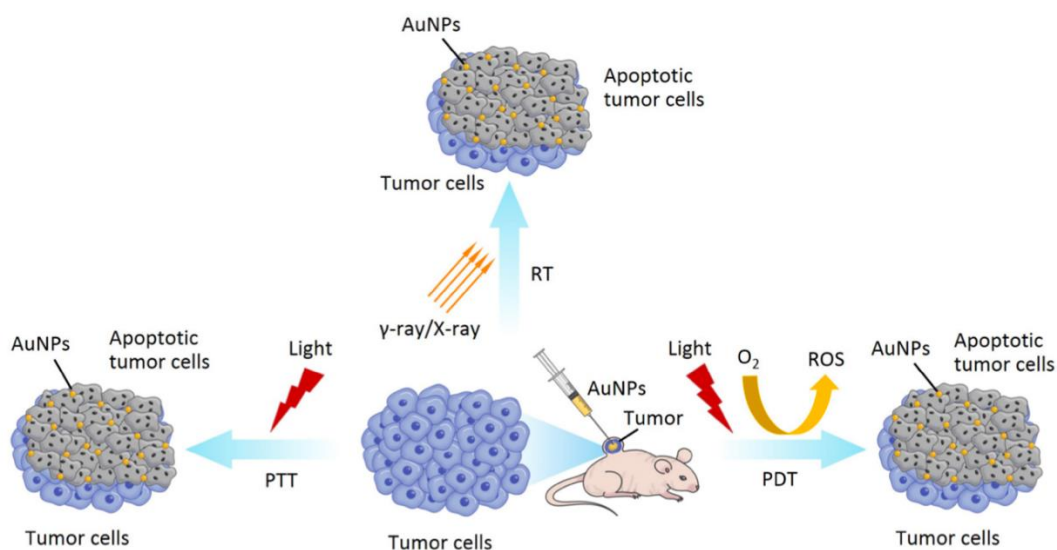


Figure 39 The application of PTT, PDT and RT for AuNPs (88).

2.3.3.5 AuNPs for transdermal delivery

AuNPs have been extensively studied in transdermal delivery. The skin permeability of AuNPs is related to several factors i.e., particles size, surface charge, chemical functionalization, and aggregation state. An effect of particle size on skin penetration was investigated by Raju et al (2018). The study was performed using Franz diffusion cell. As a result, AuNPs pass through the skin in a size dependent manner where small particles are more likely to pass through the stratum corneum. (12) The surface charge also played an important role for skin penetration. The effect of surface charge was investigated by Hao et al (2017). In this study, AuNPs with three different surface charges were tested. AuNPs were functionalized with cetyltrimethylammonium bromide (CTAB), PVP, and citrate ions referring to the positively, neutral, and negatively charged particles, respectively (14). The result demonstrated that AuNPs with a positive surface charge showed a more efficient penetration through the skin compared to the negatively and neutral charged particles. That is because the skin is biologically negative, so the positively charge particles would be attracted (14). Moreover, the surface of AuNPs can be functionalized with a wide range of ligands, e.g., polymers, surfactants, thiolated hydrocarbon chain etc. (100). To improve the skin penetration, Hsiao et al (2016) modified the surface of

AuNPs with polyethylene glycol (PEG) and its oleylamine derivative (PEG-OAm). The result found that PEG and PEG-OAm AuNPs were able to permeate deeper into the subcutaneous layer, whereas citrate-stabilized AuNPs were rarely permeated the stratum corneum. The greater skin permeation was resulted from the hydrophilic chain (PEG) that could solvate the keratin and disrupt the skin structure. In addition, the hydrophobic chain (OAm) could merge with lipid matrix of the stratum corneum and induced conformational change of the lipid structure. In the end, AuNPs were able to pass through the stratum corneum (143).

Not only AuNPs could permeate through the skin itself, but also, they helped to increase the skin permeation of co-delivered drugs. Aniruthan et al. (2018) fabricated transdermal membranes incorporated with AuNPs and oleylamine-functionalized nano-diamonds (AuD). Ketoprofen was added in the AuD patch, and the skin permeation was conducted using Franz diffusion cell. The result from this study showed that higher amount of ketoprofen was delivered by AuD-incorporated films, suggesting that the skin permeation of ketoprofen was improved by AuD (Figure 40) (15).

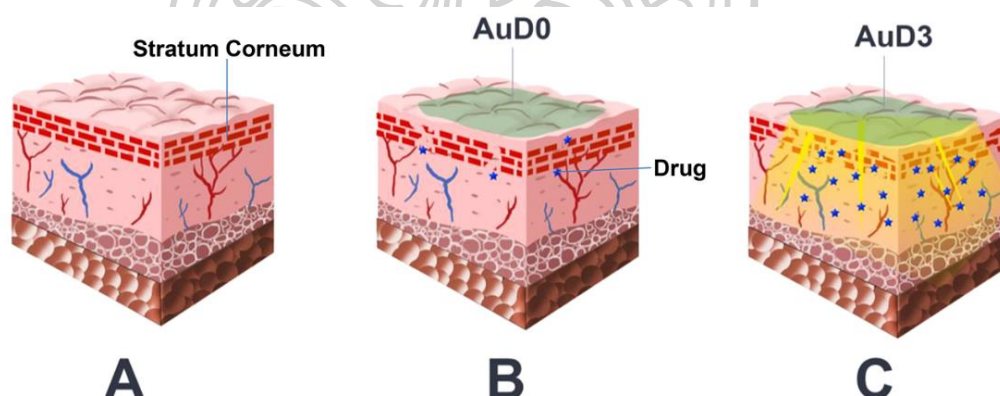


Figure 40 Graphical representation of (A) untreated skin, (B) skin treated with ketoprofen patch without AuD, and (C) skin treated with ketoprofen-incorporated AuD patch (15).

Additionally, there were evidences suggesting that AuNPs could also help the skin permeation of macromolecules such as proteins. The experiment on co-delivery of AuNPs and protein from Huang et al. (2010) revealed that AuNPs could enhance

the penetration of two model proteins, horseradish peroxidase (HRP) and β -galactosidase (β -gal), through the epidermis and dermis of mice skin. The enhancement was reported to result from the hydrophobic interaction between AuNPs and the skin lipid structure which created channels through the skin and allow exogenous compounds to penetrate (Figure 41). Additionally, this study demonstrated the potential of AuNPs for transcutaneous vaccination by a topical co-administration of AuNPs with ovalbumin (OVA) antigen. Mice treated with topical OVA combined with AuNP were highly immunized proved by similar anti-OVA antibody compared to intramuscular vaccination. On the other hand, the control group (mice treated with topical OVA without AuNPs) exhibited extremely low IgG level due to poor absorption of large molecules through the percutaneous route (17).

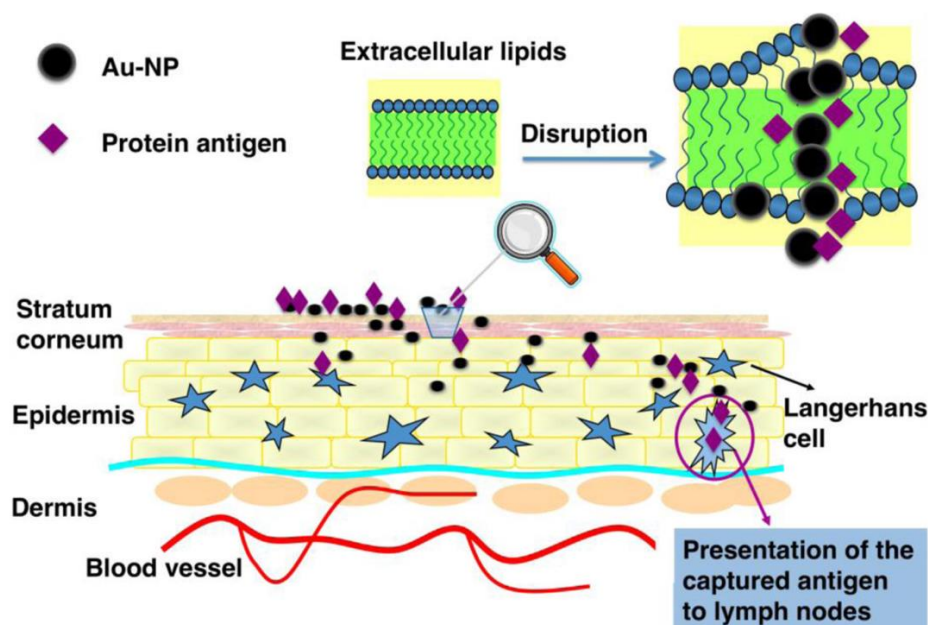


Figure 41 Schematic presentation of protein antigen transcutaneous delivery by AuNPs (17).

2.4 Method for evaluation skin delivery

The techniques for modelling skin penetration can be divided into quantitative and qualitative techniques. The quantitative techniques are usually performed to measure the amount of drug permeated through the skin over time. Diffusion cells are

used as a gold standard model for quantitative evaluation. Whereas, qualitative techniques are the use of microscopic and spectroscopic methods to evaluate drug penetration (144).

2.4.1 Diffusion cells

The diffusion cells are the classic method for skin penetration and permeation studies. This method required a skin membrane, which can be obtained from human, rat, rabbit, monkey, or snake. The diffusion cells can be classified into two classes which are static and flow-through cells. In static cells, the receptor medium is a constant reservoir where the perfusate is collected and replaced at each time point. On the other hand, the flow through cell uses a pump to pass the perfusate to the receptor chamber. The static diffusion cells can be further divided into 2 types based on the skin orientation which are vertical or horizontal cells. The vertical static diffusion cell, known as Franz diffusion cell, is popularly used to evaluate *in vitro* permeation of the transdermal delivery system. The Franz cell was named after the first inventor, Dr. Thomas J. Franz, in 1970 (144, 145).

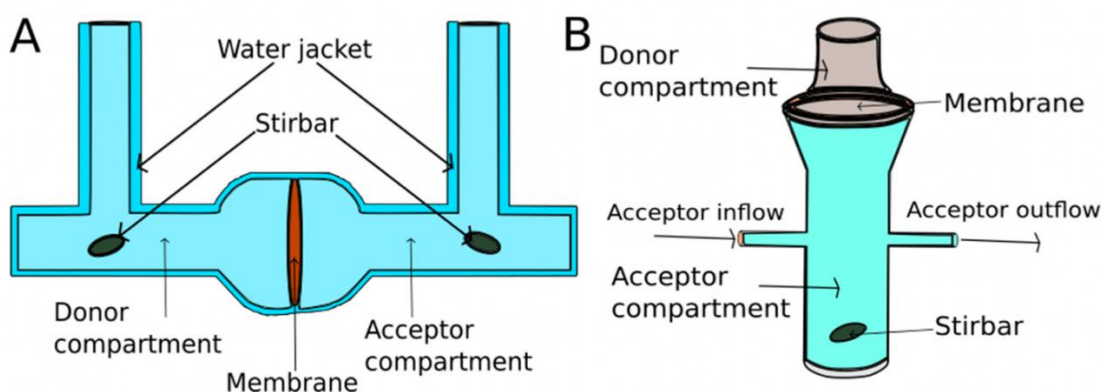


Figure 42 (A) Horizontal diffusion cell and (B) Flow-through cell (144).

Vertical static diffusion cell or Franz cell consists of three major components: (i) an upper donor cell for drug application, (ii) a skin membrane which the drug may diffuse, and (iii) a receptor chamber holding the medium which the permeated drug will be sampled and determined. To set up the experiment, the skin membrane is

placed with SC facing to the donor side where the drug will be applied, and the receptor chamber is filled with the medium. The skin is firmly fixed and clamped between upper and bottom cells to prevent the leakage. Several parameters should be considered to obtain the accurate and precise permeability data i.e., sink condition, incubation time, temperature, solution mixing, skin hydration, and active compound quantity. To achieve sink condition, the receptor medium should be able to freely dissolve the drug and the drug concentration in the receptor chamber should not exceed 10% of drug solubility. The receptor fluid is needed to be replaced with fresh medium after each sampling to maintain the condition. Moreover, the receptor medium should be kept stirring continuously to ensure that the drug is properly mixed. In general, the fluid needs to be capable of maintaining the skin viability for the entire experiment at physiological pH. In case of hydrophilic drug, buffer saline solution is recommended. However, for lipophilic drugs, it is difficult to hold the sink condition due to the aqueous solubility limitation. Thus, the solubilizing agents, such as bovine serum albumin, ethanol, and nonionic surfactant, may be acquired (146).

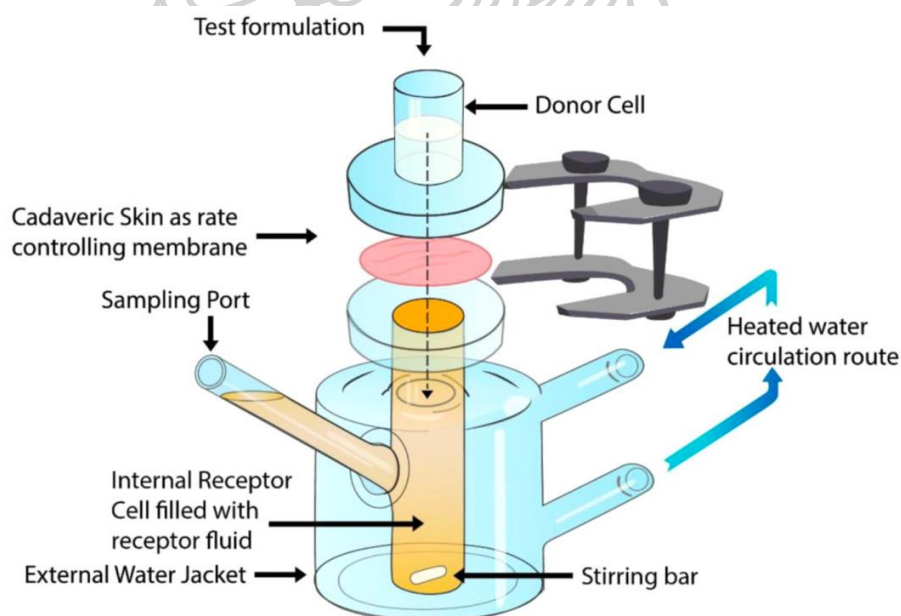


Figure 43 Graphical diagram of vertical static diffusion cell (146).

Once the formulation is applied, the active ingredient permeates across the skin to the receptor chamber. The temperature of the receptor fluid should be controlled by the circulating water in the water jacket to mimic the physiological skin

surface temperature of human at $32\pm 1^\circ\text{C}$. Permeated molecules are collected at each time point, analyzed, and examined on the permeation profile. Cumulative drug permeated is plotted against time. The transdermal flux (J), which is the permeation rate, is obtained from slope of the graph (146, 147).

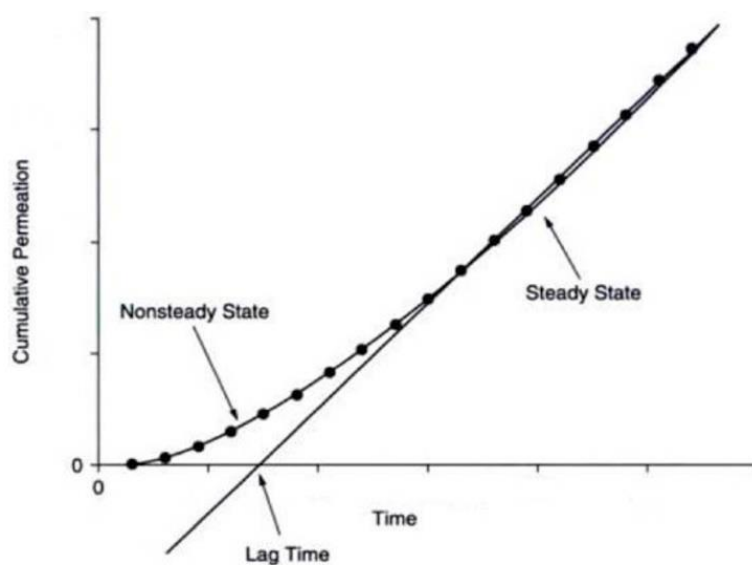


Figure 44 Typical plot of skin permeation study (147).

2.4.2 Tape stripping

Tape stripping technique is a widely used method to assess topical formulations. This technique involves the sequential application and removal an adhesive tape to collect the stratum corneum. Pressure and the speed of application should be the same during the entire process to assure the homogeneity of the relative amount of stratum corneum removed. Later, the collected tape pieces are analyzed for the drug amount (144, 148).

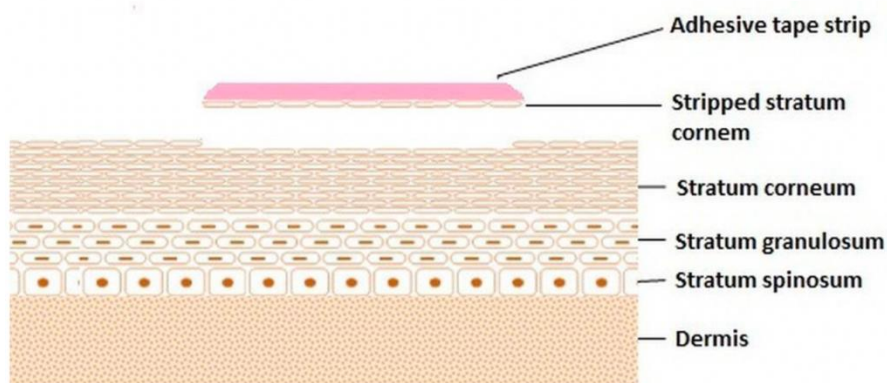


Figure 45 Tape stripping of stratum corneum (148).

2.4.3 Confocal Laser Scanning Microscope (CLSM)

Confocal laser scanning microscope (CLSM) is a microscopic technique that is important for skin penetration assessment. CLSM is based on a laser source that emits a monochromatic beam to excite the fluorescent markers. The fluorescence emitted by the fluorescent-containing specimen in a single plane is filtered through a dichroic mirror to reach the objective lens, and the detector which gives a high-resolution image. The fluorescence markers may be incorporated, labelled, or co-delivered with the particles. The drug penetration pathway can be visualized through CLSM (149).

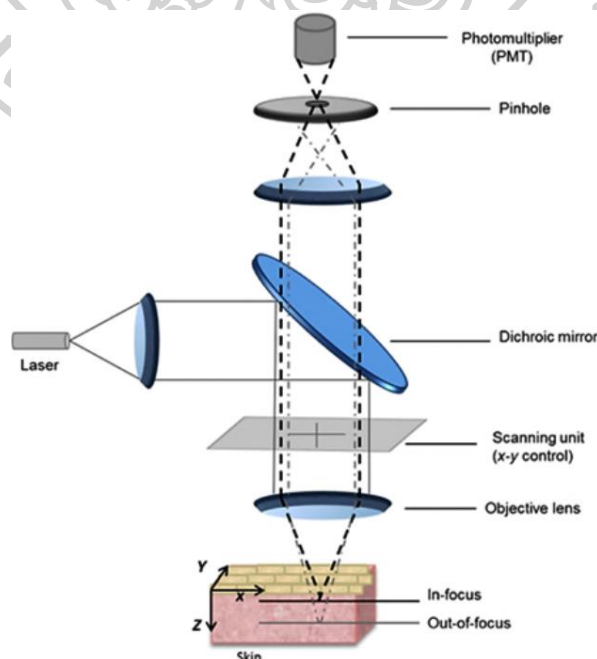


Figure 46 Schematic diagram of CLSM (149).

Fluorescein sodium salt (NaFI) is a small hydrophilic molecule (MW 376 Da, log P -1.52) that exhibit fluorescent property and commonly used as a diagnostic tool in topical applications (150). Albumin-fluorescein isothiocyanate conjugate (FITC-BSA) is a bulky structured protein linked to a fluorescence marker (151). NaFI and FITC-BSA represented small and large hydrophilic molecule, respectively, and are often used as fluorescence tracers in skin delivery studies.



CHAPTER 3

MATERIALS AND METHODS

3.1 Materials

- Albumin-fluorescein isothiocyanate conjugate (FITC-BSA; MW of 66 kDa) (Sigma-Aldrich, MA, USA)
- Bovine serum albumin (BSA; ThermoFisher Scientific, MA, USA)
- Chitosan (75%–85% degree of deacetylation, low molecular weight 50-190 kDa) (Sigma-Aldrich, MA, USA)
- Cryostat embedding medium (Bio-Optica Milano Spa, Milano, Italy)
- Fast drying mounting medium for cover slipping (Bio-Optica Milano Spa, Milano, Italy)
- Fluorescein sodium salt (NaFI; MW of 376.27 Da) (Sigma-Aldrich, MA, USA)
- Glutaraldehyde (EM grade) (Ted Pella Inc, CA, USA)
- Gold(III)chloride or tetrachloroauric acid trihydrate ($\text{HAuCl}_4 \cdot 3\text{H}_2\text{O}$) (Sigma-Aldrich, MA, USA)
- Hyaluronic acid (HA; MW of 1200-1800 kDa) (P.C.Drug Center, Bangkok, Thailand)
- Nitric acid (Sigma-Aldrich, MA, USA)
- Polyvinyl alcohol (PVA; hydrolyzed, MW of 89-98 kDa) (Sigma-Aldrich, MA, USA)
- Polyvinyl pyrrolidone K90 (PVP K-90) (Sigma-Aldrich, MA, USA)
- Potassium chloride (KCl; Sigma-Aldrich, MA, USA)
- Potassium dihydrogen orthophosphate (KH_2PO_4 ; Sigma-Aldrich, MA, USA)
- Sodium chloride (NaCl; Sigma-Aldrich, MA, USA)
- Sodium dihydrogen orthophosphate (NaH_2PO_4 ; Sigma-Aldrich, MA, USA)
- Tri-Sodium citrate dihydrate (Merck, USA)
- All chemical agents were analytical grade.

3.2 Equipments

- 96-well flat bottom microplates (Corning®, Corning Inc., MA, USA)
- Aluminum foil
- Analytical balance (Sartorius® series-CP224S) (Data Weighing Systems, Inc., IL, USA)
- Bath sonicator (Transsonic series 890/H, Singen, Germany)
- Beakers (50, 100, 250, and 1000 mL) (Pyrex, AZ, USA)
- Centrifuge (Eppendorf^f™ 5804 Benchtop centrifuge, Hamburg, Germany)
- Centrifuge tubes (15 ml, and 50 ml)
- Confocal Laser Scanning Microscope (CLSM; Zeiss LSM 800-Airy scan, Carl Zeiss, Jena, Germany)
- Cryomicrotome (Leica 1850, Leica Instruments GmbH, Nussloch, Germany)
- Cylinders (25, 50, and 100 mL) (Pyrex, AZ, USA)
- Desiccator
- Digital microscope (Dino-Lite Edge AM7915 Series, New Taipei city, Taiwan)
- Dinocapture 2.0 software
- Disposable syringes (NiproTM, Ayutthaya, Thailand)
- DLS instrument (Zetasizer Nano ZS, Malvern, UK)
- Franz diffusion cells
- Frozen section medium (Neg 50, Microm International, Waldorf, Germany)
- Glass bottles (500, and 1000 mL)
- Glass slides and cover slips
- Inductive coupled plasma – Mass spectroscopy (ICP-MS; Agilent Technologies, 1100 series, Santa Clara, CA, USA)
- Inverted Fluorescence Microscope (Nikon® TE2000-U, Nikon Instech Co., Ltd., Kanagawa, Japan)
- Microcentrifuge tubes (Eppendorf^f™ microcentrifuge tube, Bangkok, Thailand)
- Micropipette and micropipette tips
- Microplate reader (VICTOR NivoTM Multimode Plate Reader, PerkinElmer, Germany)

- Microwave synthesizer (Discover SP, CEM Corporation Inc., NC, USA)
- Nebulizer (PEEK Mira-Mist Nebulizer, PerkinElmer Inc., Canada)
- pH meter (LAQUAtwin-pH-22, Japan)
- Polydimethylsiloxane (PDMS) micro-mold (Blueacre technology, Ireland)
- Polymeric film (Parafilm M[®], Bemis, NA, USA)
- Probe sonicator (Sonics VibraCell[™], Sonic and Materials Inc., CT, USA)
- Refrigerated bath circulator (WiseCircu[®] WCR-P6, Daihan Scientific Co., Seoul, South Korea)
- Refrigerator (4-8°C) and Freezer (-20°)
- Scanning electron microscope (SEM; S-3400N, Hitachi Hi-Tech, Kanagawa, Japan)
- Scissors, surgical blades, and forceps
- Stirring rods
- Texture analyzer (TA. XT plus, Stable Micro Systems, UK)
- Transmission electron microscope (TECNAI 20, Philips, OR, USA)
- Vortex mixer
- Water bath (Hetofrig CB60; Heto High Technology, FL, USA)
- Zen blue edition software

3.3 Methods

3.3.1 The study of AuNPs

3.3.1.1 Synthesis of AuNPs

i. Citrate-stabilized AuNPs (Ci-AuNPs)

Ci-AuNPs were prepared by heating 95 mL of chloroauric acid solution (containing 5 mg of Au) to the boiling point. Then, 5 mL of 1 %v/v sodium citrate solution was added to the boiling solution with energetic mechanical stirring. The color of the solution gradually darkened over time and the heating was continued until a deep wine-red color (indicating colloidal gold solution) was obtained. The colloidal gold solution was stored at 4°C in a refrigerator until used.

ii. Chitosan-capped AuNPs (CS-AuNPs)

Firstly, a 0.1 %w/v chitosan solution was prepared using a low molecular weight chitosan (50-190 kDa, Sigma-Aldrich, MA, USA). The polymer was weighed (0.1 g) and dissolved in 1 %v/v acetic acid, then the volume was adjusted to 100 mL. The solution was stirred with a magnetic bar until completely dissolved. Gold (III) chloride solution was prepared at a concentration of 10 mM by dissolving gold (III) chloride ($\text{HAuCl}_4 \cdot 3\text{H}_2\text{O}$, Sigma-Aldrich, MA, USA) in deionized water at room temperature. A microwave synthesizer (Discover SP, CEM Corporation, USA) was used to synthesize CS-AuNPs. Briefly, 750 μL of 10 mM chloroauric acid solution and 5 mL of chitosan solution was mixed in a glass reaction tube. Then, the mixture solution was irradiated in the microwave at 125 °C with a total reaction time of 1 min 40 s. The gradual change of color to a red-wine solution indicated the formation of CS-AuNPs. The resulting solution was cooled immediately by placing in an ice bath and stored at 4 °C until used.

3.3.1.2 Characterization of AuNPs

i. Hydrodynamic diameter, polydispersity index (PDI), and zeta potential measurement

The AuNPs solution was diluted (1:99) with distilled water and subsequently measured for hydrodynamic diameter, PDI, and zeta potential using a Zetasizer (Nano-ZS, Malvern Instrument, Worcestershire, UK). The measurements were carried out in triplicate.

ii. Morphology and particle size measurement

The morphology of AuNPs was visualized under TEM (TECNAI 20, Philips, OR, USA). A droplet containing AuNPs was dried on a copper grid, and the samples were visualized under the microscope at 100 kV using 300 k \times magnification.

iii. UV Absorbance

To determine the SPR bands of AuNPs, the UV spectra of Ci-AuNPs and CS-AuNPs were recorded by a multimode microplate reader (VICTOR NivoTM Multimode Plate Reader, PerkinElmer, Germany).

3.3.1.3 Effect of AuNPs on skin penetration

i. Preparation of porcine skin

Naturally died neonatal pigs were received from Charnchai Farm (Ratchaburi, Thailand) and the skin from abdominal area was excised on the same day of their arrival. The subcutaneous layer of the porcine skin was carefully removed using scissors and surgical blade, then the skin was kept in an aluminum foil at -20°C and used within 1 month. The skin samples were cut into a circle shape with a 3.5 cm in diameter and thawed in PBS pH 7.4 at room temperature for 2 h before use.

ii. *In vitro* skin permeation test

The porcine skin was prepared as described in section 3.2.1.3 (i.) and the skin integrity was checked prior to the experiment. Vertical Franz diffusion cells with the diffusion area of 2.27 cm^2 were used to examine skin permeability. The receptor chamber was filled with 6.5 mL of PBS pH 7.4 and the receptor fluid was agitated with a magnetic bar at a rate of 500 rpm. The dissected porcine skin was fixed between the donor and receptor compartments in a way that the SC facing up toward the donor side and fixed with a clamp to firmly hold the skin. The diffusion cells were connected to the refrigerated bath circulator (WiseCircu[®] WCR-P6, Daihan Scientific Co., Seoul, South Korea) and the receptor compartments were circulated with water through the water jacket to maintain the temperature of the skin surface at $32\pm 1^{\circ}\text{C}$ throughout the experiment. The porcine skin samples were allowed to equilibrate for 2 h, then 1 mL of the donor solution was loaded to the donor reservoirs and 0.5 mL of the receptor fluid was collected at predetermined time points (0.5-24 h) to quantify the content of permeated drug. The receptor medium was replaced with an equivalent volume of fresh PBS after each withdrawal to maintain a constant volume. NaFI and FITC-BSA (1 mg/mL) were used as small and large molecule model drugs, respectively. In this study, their aqueous solutions without the AuNPs were used as controls. Ci-AuNPs, CS-AuNPs, and low MW chitosan were simply mixed with the model drugs, and their effect on skin permeation were investigated. The AuNPs with superior enhancement effect on skin permeation was selected and the optimal concentration of AuNPs for the co-delivery with the drug was examined.

Cumulative amount of permeated drugs through the skin per unit area was plotted against the time. The transdermal flux at the steady state (J_{ss}) was

determined from the slope of the linear portion. The enhancement ratio of AuNPs (ER_{AuNPs}) was computed using the Eq. 1. ER_{AuNPs} was used to determine the penetration enhancement ability of AuNPs compared to the control.

$$ER_{AuNPs} = \frac{J_{AuNPs}}{J_{control}} \quad \text{Eq. 1}$$

Where, J_{AuNPs} is the transdermal flux of the hydrophilic compound co-delivered with AuNPs and $J_{control}$ is the transdermal flux of the hydrophilic compound in an aqueous solution.

3.3.1.4 AuNPs distribution in skin layers

After 24-h period of the skin permeation study, the skin was collected, washed with PBS pH 7.4, and wiped to remove the excess formulations on its surface. To analyze the distribution of AuNPs, the skin, epidermis, and dermis layers were separated using heat. First, the collected skin samples were immersed in PBS at $60 \pm 1^\circ\text{C}$ for 60 s. Next, the epidermis was removed using a scalpel. The epidermis and dermis were cut into small pieces and placed in separate glass vials. Also, 250 μL of the receptor fluid was collected for Au analysis. To validate the extraction method, the recovery study was also performed by dropping a certain volume of AuNPs onto the skin and air dried for several hours. Then, the skin was cut into small pieces and place in a glass vial for Au analysis.

i. Quantitative analysis of AuNPs by inductively coupled plasma-mass spectrometry (ICP-MS)

The collected samples contained in the glass vials were digested by heating with 1 mL of concentrated nitric acid at 90°C for 2 h. Then, the digested samples were transferred to 10-mL volumetric flasks, and made to volume with ultrapure water. The prepared samples were subjected to Au analysis using an ICP-MS (Agilent 1100 series, Santa Clara, CA, USA). Quantitative analysis of Au was performed using argon as a carrier gas at a rate flow of 0.86 L/min and make-up gas 0.2 L/min. The samples were formed as a mist by passing through a nebulizer (PEEK Mira-Mist Nebulizer, PerkinElmer Inc., Canada) and heated to ionized. The ions were extracted

into a mass spectrometer, separated based on mass-to-charge ratio, and the amount of ^{198}Au isotope was determined.

3.3.1.5 Skin penetration pathways

The porcine skin was treated with the mixture solution of the model drugs and the selected AuNPs for 1-2 h using the diffusion cells. Then, the skin was collected, washed three times with PBS pH 7.4, wiped with a lens wipe (KIMTECH Science, Ontario, Canada), cut into small pieces, and kept in freezer at -20°C prior to the microscopical investigation.

i. Confocal laser scanning microscopy (CLSM) study

CLSM was employed to elucidate skin penetration pathway of the model drugs. To visualize the penetration depth of the fluorescence compounds (NaFI and FITC-BSA), the skin tissue was placed on a glass slide cover slip with the SC facing upwards the microscope condenser and soaked with methyl salicylate as an immersion oil. The visualization was carried out by CLSM (Zeiss LSM 800-Airy scan, Carl Zeiss, Jena, Germany). Images from the region of interest were taken in an x - y plane along the z axis to generate a 3D information from the skin samples using ZEISS ZEN Blue edition software.

3.3.1.6 Visualization of AuNPs in the skin by TEM

After the skin permeation study, the collected skin was cut into small pieces and soaked in 2.5 % glutaraldehyde solution in 0.1 M PBS at 4°C for 4 h to preserve the protein structure. Then the skin samples were washed and immersed in 0.1 M PBS at 4°C . A piece of skin sample was trimmed to 1×1 mm size and fixed with 1 % Osmium tetroxide to preserve the lipid structure. Afterwards, the samples were dehydrated with ethanol and embedded in a pure Araldite 502 resin. The resin containing skin sample was polymerized at 60°C for 24 h. Then the resin-embedded skin samples were cut by an ultramicrotome (thickness 60-90 nm) and placed on a copper grid to observe under TEM at 75 kV (TECNAI 20, Philips, OR, USA).

3.3.1.7 Cytotoxicity of AuNPs

MTT assay was used to assess cytotoxicity of AuNPs. Human fibroblasts and keratinocytes were used as representatives of human skin cells. CS-AuNPs were freeze dried and redispersed in sterile water prior to the MTT assay. In brief, the cells were seeded at 10,000 cells/well in a 96-well plate and incubated at 5% CO₂ 37 °C for 24 h. Then, the cells were treated with 100 μL of AuNPs at various concentrations (12.5-100 μg/mL) and the cell viability was assessed after 24-h treatment. The old medium was replaced with 100 μL of fresh medium and 25 μL of MTT solution (0.5 mg/mL in PBS) and the cells were placed in an incubator for 3 h. Subsequently, the medium was removed and replaced with 100 μL of DMSO. The formazan crystals were dissolved, yielding a purple solution, and the absorbance was measured at 550 nm using a spectrophotometer. The untreated cell was used as a control. Cell viability was calculated as a percentage relative to untreated control using the Eq. 2.

$$\% \text{ Cell viability} = \frac{A_{\text{sample}}}{A_{\text{control}}} \times 100 \quad \text{Eq. 2}$$

Where, A_{sample} is the absorbance of cells treated with samples and A_{control} is the absorbance of untreated control cells.

3.3.1.8 Stability of AuNPs

Ci-AuNPs and CS-AuNPs were kept in the dark at 4 °C. Their stability was evaluated every 7 days for 28 days, measuring the changes in the hydrodynamic diameter and zeta potential using a Zetasizer (Nano-ZS, Malvern Instrument, Worcestershire, UK).

3.3.2 Development and Fabrication of DMNs

3.3.2.1 Preparation of polymer solutions

DMNs were made of hydrophilic polymers at a fixed concentration which were 10 %w/w polyvinyl alcohol (PVA), 40 %w/w polyvinyl pyrrolidone K90 (PVP

K90), and 5 %w/w hyaluronic acid (HA). HA and PVP K90 were prepared by dissolving in deionized water, whereas PVA was dissolved in hot water (~80 °C) and stirred until a homogeneous solution was obtained. Subsequently, the polymer solutions were centrifuged at 4,000 rpm for 20 min to remove the air bubbles.

3.3.2.2 Fabrication of DMNs

To fabricate the DMNs, the polymer-blended solutions were cast in a silicone micromold (11×11 conical-shaped arrays with the height of 600 μm and base width of 300μm, Blueacre technology, Ireland) and centrifuged at 4,000 rpm for 20 min to fill the polymer solution into the mold cavities. The fabrication was carried out at 25°C and 75 %RH. Then, the samples were dried in a desiccator for 48 h. The MNs were separated from the mold and kept in a desiccator until use.

3.3.2.3 Fabrication of AuNPs-loaded DMNs (Au-MNs)

AuNPs solution was incorporated into the mixture of polymer blend at various concentrations. Other processes were carried out as described in section 3.3.2.2. The formulation that provided the desirable mechanical strength as well as physical properties was selected for *in vitro* skin permeation study.

3.3.2.4 Characterization of DMNs and Au-MNs

i. Morphology

The physical appearance of the fabricated microneedles was captured by a digital microscope (Dino-Lite Edge/5MP, Hsinchu, Taiwan), and their dimensions (width, height, and interspace) were measured using Dinocapture 2.0 software. In addition, scanning electron microscope (SEM) was used to confirm the complete fabrication of Au-MNs and DMNs. SEM was performed at 10 kV and 225 × magnification.

ii. Mechanical strength

The mechanical strength is considered as an important characteristic of MNs because it has a great impact on the application on the skin. The mechanical

strength of the MNs was evaluated by a texture analyzer (TA.XT plus, Stable Micro Systems, UK) using a compression mode. The compression force was set at 10.769 N per 121 needles with the speed of 0.5 mm per second. The DMNs patch was attached to a cylindrical probe and compressed onto a flat aluminum block. Photos of the needles before and after the compression were taken with Dino-Lite microscope. The height of each needle was measured using Dinocapture 2.0 software. The percentage of height reduction was calculated using Eq. 3 and expressed as mean \pm SD.

$$\% \text{ Height reduction} = \frac{H_B - H_A}{H_B} \times 100 \quad \text{Eq. 3}$$

Where, H_B is the height of needles before the compression and H_A is the height of needles after the compression.

iii. Skin insertion

The skin samples were thawed in PBS pH 7.4 at room temperature prior to the experiments. The hairs on the skin were trimmed using scissors, then the porcine skin was placed on a wax sheet with the epidermis facing upward. The skin was then equilibrated with PBS pH 7.4 at room temperature for 1 h.

DMNs and Au-MNs were manually pressed into the skin for 30 s with a thumb. Subsequently, the MNs were carefully removed from the skin and the applied area was dyed with 1 % methylene blue solution. Blue stained holes on the skin indicated the complete insertion of the MNs. The percentage of penetration was determined from the number of blue stained holes using Eq. 4.

$$\% \text{ Penetration} = \frac{\text{The number of blue staining holes}}{\text{The total number of needles}} \times 100 \quad \text{Eq. 4}$$

iv. Ex vivo skin dissolution study

The frozen porcine skin was prepared as described in section 3.3.2.4 (iii). Then, the DMNs and Au-MNs were inserted into the skin by pressing manually with a thumb for 30 s and a 10 g-steel weight was placed on the MN patch to prevent the separation. Then, the skin was immediately placed in an incubator at 37 ± 1 °C. The

MNs were removed from the skin at predetermined time. The remaining needles were captured by a Dino-Lite microscope.

3.3.2.5 *In vitro* skin permeation of AuNPs loaded MNs (Au-MNs)

The frozen porcine skin was prepared as described in section 3.3.2.4 (iii). Then, DMNs and Au-MNs were applied on the porcine skin using a thumb pressure and fixed with adhesive tape. Subsequently, the porcine skin was mounted between the donor and receptor compartments which was filled with 6.5 mL of PBS pH 7.4. The receptor fluid was constantly agitated with a magnetic bar at a rate of 500 rpm. A clamp was used to fix the donor and receptor compartments. The diffusion cells were connected to the refrigerated bath circulator (WiseCircu[®] WCR-P6, Daihan Scientific Co., Seoul, South Korea), and the receptor compartments were circulated with water in a water jacket to maintain the skin surface at 32 ± 1 °C throughout the experiment. At predetermined time points (0.5-24 h), 0.5 mL of receptor fluid was then collected for the analysis of the model drugs. The receptor medium was replaced with an equivalent volume of fresh PBS after each withdrawal to maintain a constant volume. The skin permeation profile of DMNs and Au-MNs (cumulative amount of drug permeated through the skin per unit area vs time) were plotted.

3.3.2.6 Stability of Au-MNs

The stability of Au-MNs was evaluated based on their physical appearances (color and shape) and the mechanical strength. The Au-MNs were packed with silica gel in a zipper pouch and stored at 25 ± 2 °C and 75 ± 5 %RH. The stability was assessed at 0, 1, 3, and 6 months

3.3.3 Quantitative assay of hydrophilic compounds

3.3.3.1 Fluorescein sodium (NaFI)

The amount of NaFI was evaluated by fluorescence spectrophotometer (VICTOR Nivo[™] Multimode Plate Reader, PerkinElmer, Germany). One hundred microliter of each collected samples was transferred to 96-well plate and subjected for fluorescence detection at an excitation wavelength and emission wavelength of 485

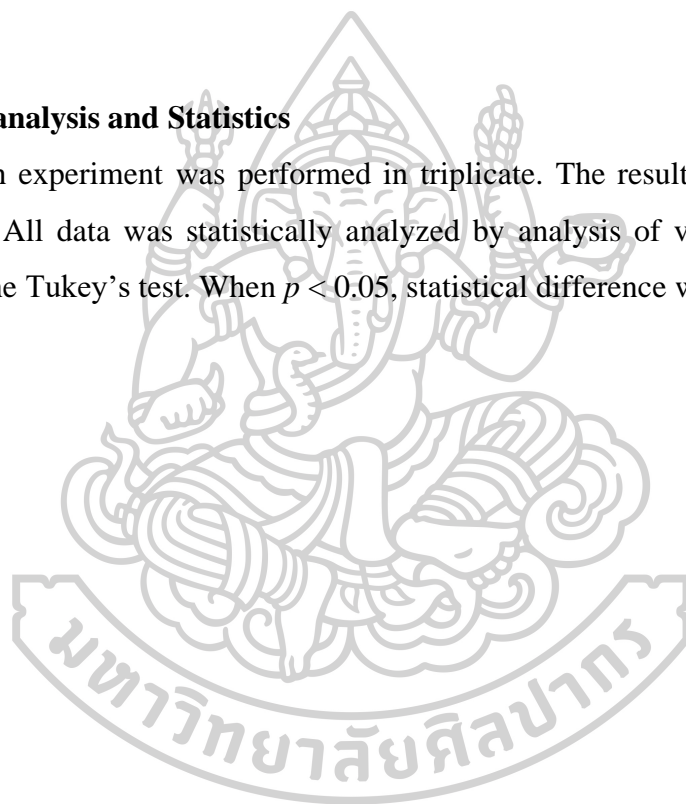
nm and 535 nm, respectively. A standard curve in the range of 10-500 ng/mL with $R^2 > 0.999$ was used to calculate the concentration of NaFl.

3.3.3.2 Albumin-fluorescein isothiocyanate conjugate (FITC-BSA)

The concentration of FITC-BSA was determined by fluorescence spectrophotometer (VICTOR Nivo™ Multimode Plate Reader, PerkinElmer, Germany) at an excitation wavelength and emission wavelength of 460 nm and 515 nm, respectively. A standard curve in the range of 10-50 $\mu\text{g/mL}$ with $R^2 > 0.999$ was used to calculate the FITC-BSA concentration.

3.3.4 Data analysis and Statistics

Each experiment was performed in triplicate. The results were expressed as mean \pm S.D. All data was statistically analyzed by analysis of variance (ANOVA), follow by the Tukey's test. When $p < 0.05$, statistical difference was noted.



CHAPTER 4

RESULTS AND DISCUSSION

4.1 The study of AuNPs

4.1.1 Characterization of AuNPs

AuNPs functionalized with chitosan (CS-AuNPs) and citrate ions (Ci-AuNPs) were used as skin penetration enhancers in this study. AuNPs were synthesized using chemical reduction approach. In brief, Au^{3+} was reduced by a reducing agent and stabilized by the ligands. Low MW chitosan and sodium citrate were functioned as reducing and stabilizing agents for CS-AuNPs and Ci-AuNPs, respectively. CS-AuNPs were synthesized based on the microwave-assisted technique using green chemistry approach, whereas Ci-AuNPs were produced using a conventional Turkevich method. The synthesized Ci-AuNPs and CS-AuNPs exhibited a ruby red color with the SPR bands illustrated the maximum absorption at 520 nm (Figure 47) which comply to the ruby red reflection confirming the success of AuNPs colloidal dispersion formation. During synthesis, the solution containing Au^{3+} exhibited a yellowish solution, and it was gradually changed to light pink and became darkening as being converted to the zero-valence state (Au^0). Finally, the synthesized AuNPs colloidal dispersion appeared in ruby red color, which was attributed to the surface plasmon resonance phenomenon (SPR). With the exposure to light, the oscillations of free electrons in the electron cloud are induced in resonance with the frequency of visible light and causes an absorption of the light in the blue-green region, reflecting the red light (94, 95, 152).

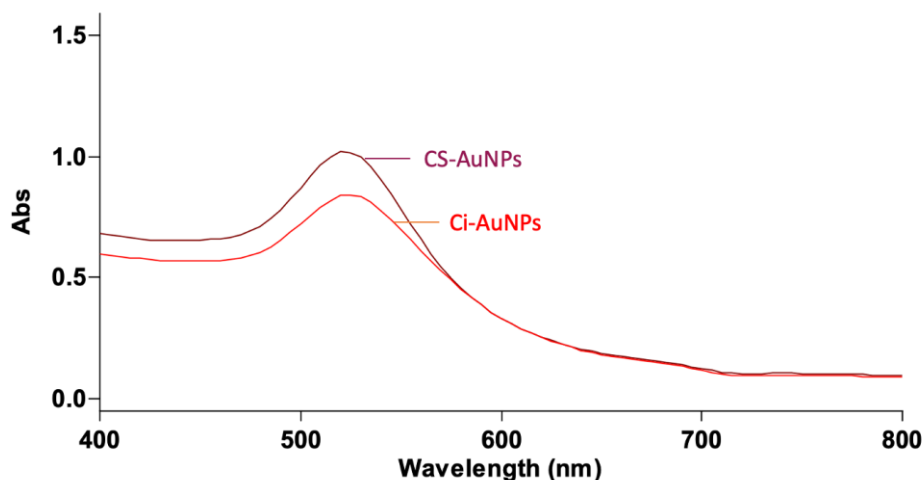


Figure 47 Ci-AuNPs and CS-AuNPs exhibited ruby red color with the SPR absorption band at 520 nm.

The hydrodynamic diameter, polydispersity index (PDI), and zeta potential (ZP) of CS-AuNPs and Ci-AuNPs were presented in Table 1. As reported by the dynamic light scattering (DLS) measurement, the obtained AuNPs had narrow size distribution (PDI < 0.4) within a nano-sized range (< 100 nm). The visualization under TEM (Figure 48) also confirmed that CS-AuNPs and Ci-AuNPs were nano-scaled solid spherical particles. CS-AuNPs had a positive ZP of +30 mV that was attributed to the protonated amine group ($-\text{NH}_3^+$) of the glucosamine on the chitosan structure, whereas Ci-AuNPs showed a negative surface charge of -60 mV due to the surrounding citrate ions on the surface. Therefore, the AuNPs had a desirable physicochemical property with potential colloidal stability owing to their high ZP values.

Table 1 Hydrodynamic diameter, PDI, and ZP of AuNPs.

AuNPs	Hydrodynamic diameter (nm)	PDI	ZP (mV)
CS-AuNPs	38.4±0.7	0.32±0.01	+30.7±1.2
Ci-AuNPs	32.2±0.7	0.33±0.01	-60.2±0.4

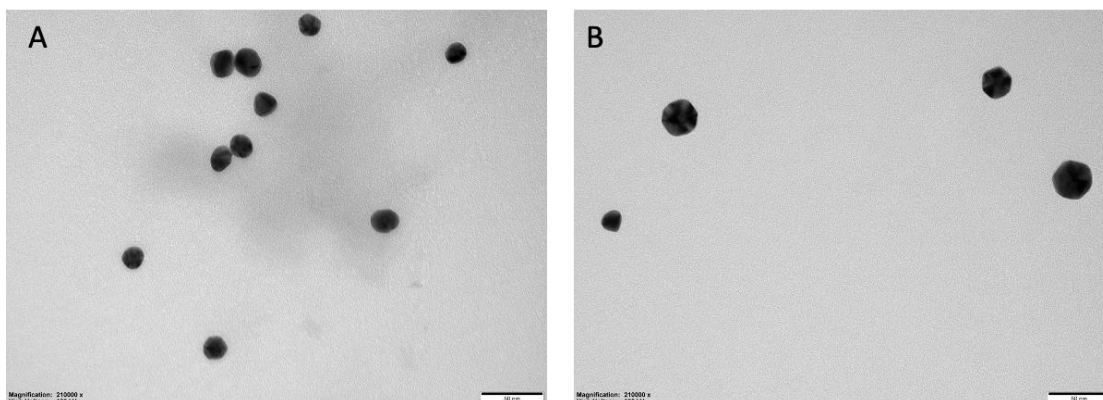


Figure 48 TEM images of (A) Ci-AuNPs and (B) CS-AuNPs at 300k magnification.

4.1.2 *In vitro* skin permeation study

4.1.2.1 Effect of AuNPs on skin penetration

Skin permeation of hydrophilic permeants with the presence of skin penetration enhancers (CS-AuNPs, Ci-AuNPs, and CS) through porcine skin was evaluated using vertical Franz diffusion cells. The permeation profile, transdermal flux at steady state (J_{ss}), and enhancement ratio (ER) of model permeants were determined.

i. Skin penetration of small hydrophilic permeants: NaFI

The permeation profile, transdermal flux at steady state (J_{ss}), and enhancement ratio (ER) of NaFI were shown in Figure 49, 50(A), and 50(B), respectively. The results revealed that among these penetration enhancers, CS-AuNPs provided the highest permeation of NaFI with an ER of 38.2 ± 7.5 followed by Ci-AuNPs and CS solution with the ER of 18.2 ± 0.5 and 5.0 ± 0.6 , respectively. From Figure 49 and 50, the skin permeation of NaFI across the porcine skin was significantly improved by CS-AuNPs and Ci-AuNPs. Previous research suggested that the presence of AuNPs may interfere lipid organization and facilitate the penetration of external substances into the SC (15, 17). Also, CS is a biocompatible polymer that has been reported to have skin penetration enhancement effect. (153-155) In concordance with those reports, our finding suggested that CS alone could enhance the skin permeation of NaFI approximately 5 times (Figure 50).

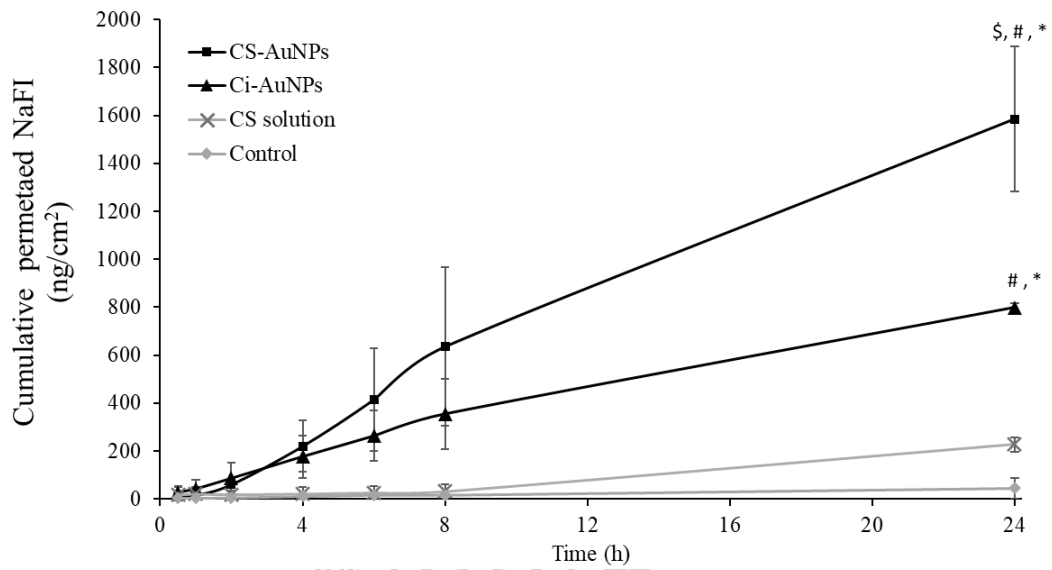
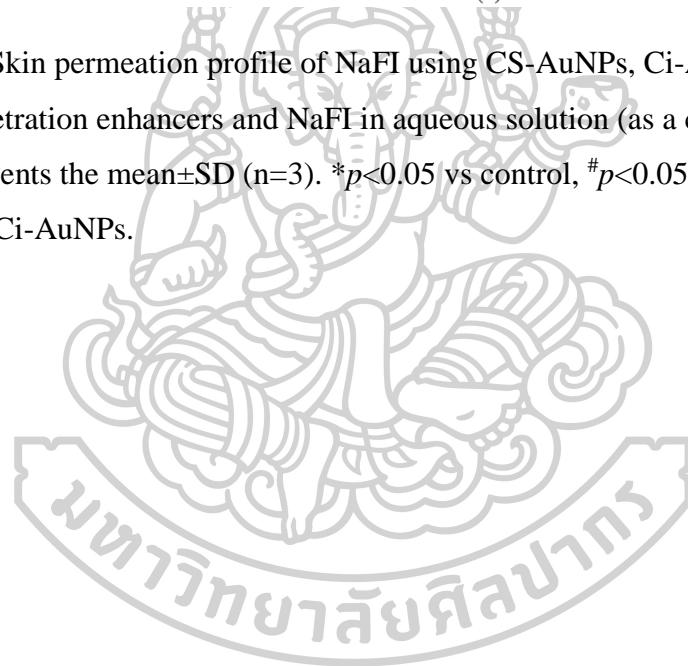


Figure 49 Skin permeation profile of NaFI using CS-AuNPs, Ci-AuNPs, CS solution as skin penetration enhancers and NaFI in aqueous solution (as a control). Each data point represents the mean±SD (n=3). * $p < 0.05$ vs control, # $p < 0.05$ vs CS solution, and \$ $p < 0.05$ vs Ci-AuNPs.



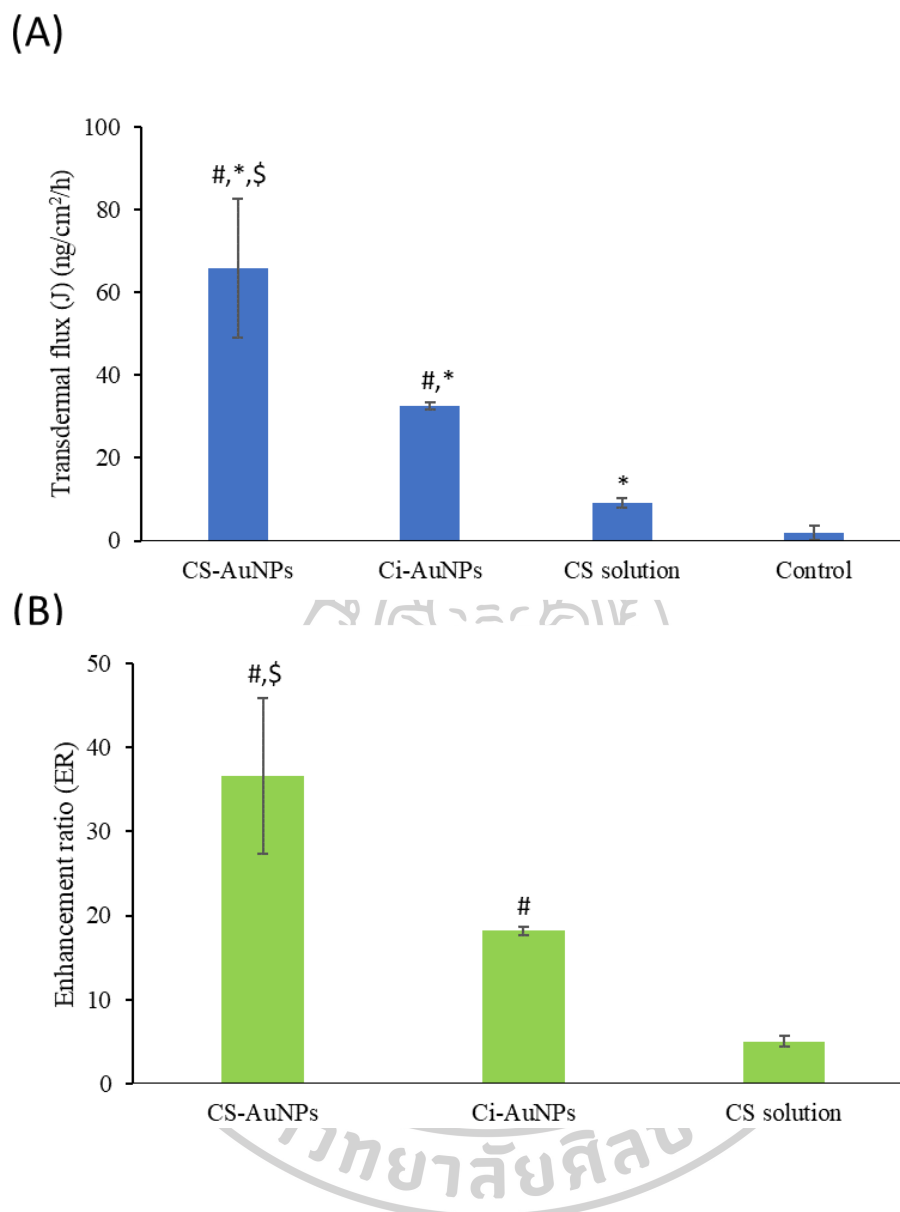


Figure 50 (A) J_{ss} and (B) ER of NaFI using CS-AuNPs, Ci-AuNPs, CS solution as skin penetration enhancers, and NaFI in aqueous solution (as a control). Each value represents the mean \pm SD (n=3). * p <0.05 vs control, # p <0.05 vs CS solution, \$ p <0.05 vs Ci-AuNPs.

ii. Skin penetration of large hydrophilic permeants: FITC-BSA

The permeation profile, transdermal flux (J), and enhancement ratio (ER) of FITC-BSA were shown in Figure 51, 52(A), and 52(B), respectively. From

the results, only CS-AuNPs showed a significant enhancement ($p < 0.05$ vs control) of FITC-BSA permeability across the porcine skin with the an ER of 3.51 ± 1.27 . On the other hand, no significant improvement was noted from Ci-AuNPs nor CS solution.

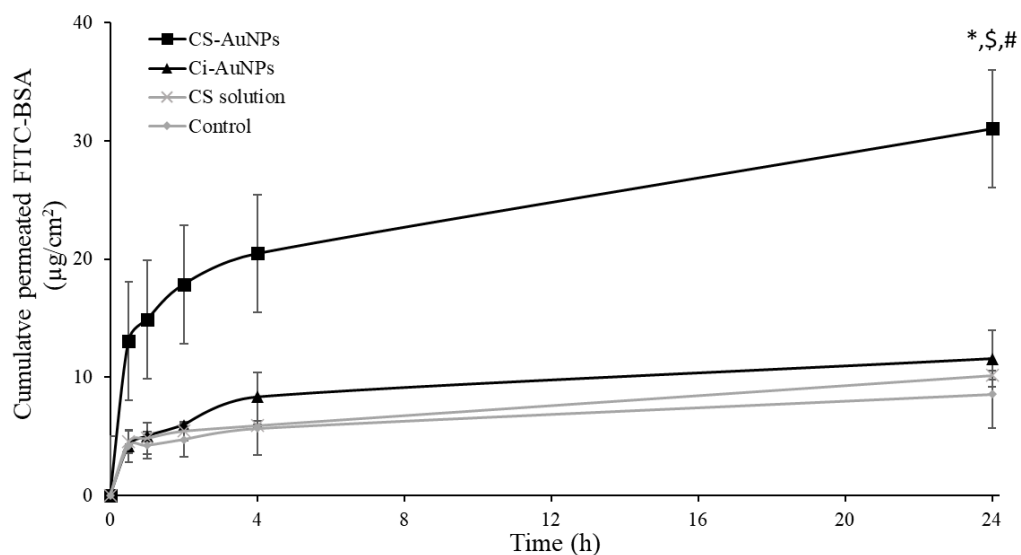


Figure 51 Skin permeation profile of FITC-BSA using CS-AuNPs, Ci-AuNPs, CS solution as skin penetration enhancers and FITC-BSA in aqueous solution (as a control). Each data point represents the mean \pm SD (n=3). * $p < 0.05$ vs control, # $p < 0.05$ vs CS solution, $^s p < 0.05$ vs Ci-AuNPs.

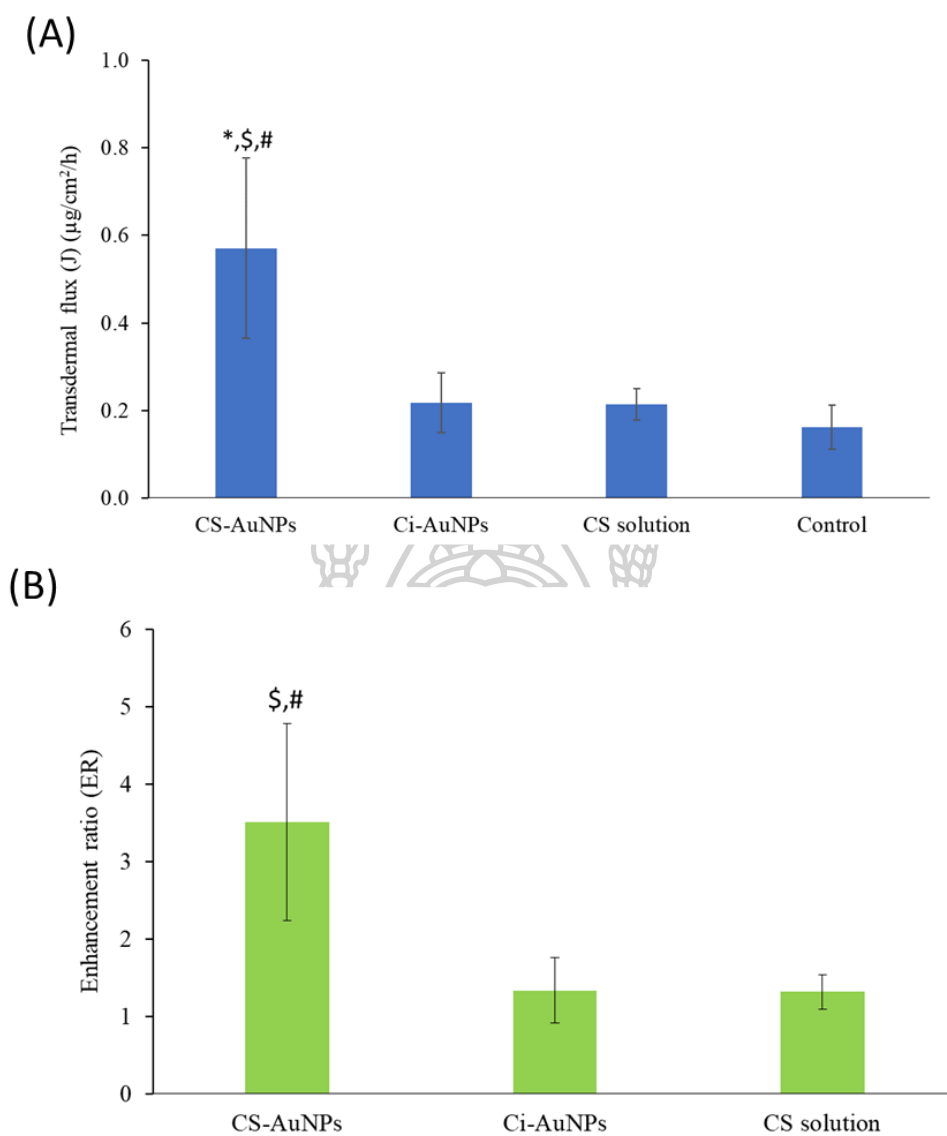


Figure 52 (A) J_{ss} and (B) ER of FITC-BSA using CS-AuNPs, Ci-AuNPs, CS solution as skin penetration enhancers and FITC-BSA in aqueous solution (as a control). Each value represents the mean \pm SD (n=3). * p <0.05 vs control, # p <0.05 vs CS solution, \$ p <0.05 vs Ci-AuNPs.

The precise mechanism of AuNPs to enhance skin delivery was not well-defined yet and remained unclear. Still, it has been proposed that AuNPs could cause the disruption of skin structure by forming reversible channels through the SC layers, resulting in the allowance of exogenous substances (15, 17). Furthermore, surface functionalization of AuNPs could be an important key to improve the skin delivery.

Our findings demonstrated that CS-AuNPs provided higher permeability of small and large permeants across porcine skin membranes. Therefore, the skin enhancement effect could be related to the positively charged surface of CS-AuNPs since it could promote the interactions between the negatively charged skin under physiological conditions. Such interactions could cause the disorder of the tight junction-associated proteins in the SC, thus increasing the drug permeation (155, 156).

Based on the findings from the permeation study, it was discovered that the combination of Ci-AuNPs and CS solution had a minor impact on enhancing skin permeation of small hydrophilic permeants but have no enhancement effect on large hydrophilic proteins. Since CS-AuNPs could effectively improve the skin permeation of both small and large hydrophilic molecules, they were considered the most effective skin penetration enhancer compared to Ci-AuNPs and CS solution. Hence, further skin studies were conducted using CS-AuNPs.

4.1.2.2 Effect of the concentration of CS-AuNPs on skin penetration

The effects of concentration of CS-AuNPs on permeation profile of small (NaFI) and large (FITC-BSA) hydrophilic permeants were also investigated using vertical Franz diffusion cells. The mixture of model drugs with 3 different concentrations of CS-AuNPs (ranging from 25 to 75 $\mu\text{g/mL}$) were used as donor solutions. The skin permeation profiles, transdermal flux at steady state (J_{ss}), and enhancement ratio (ER) of NaFI and FITC-BSA with various concentrations of CS-AuNPs were presented in Figure 53 to 56.

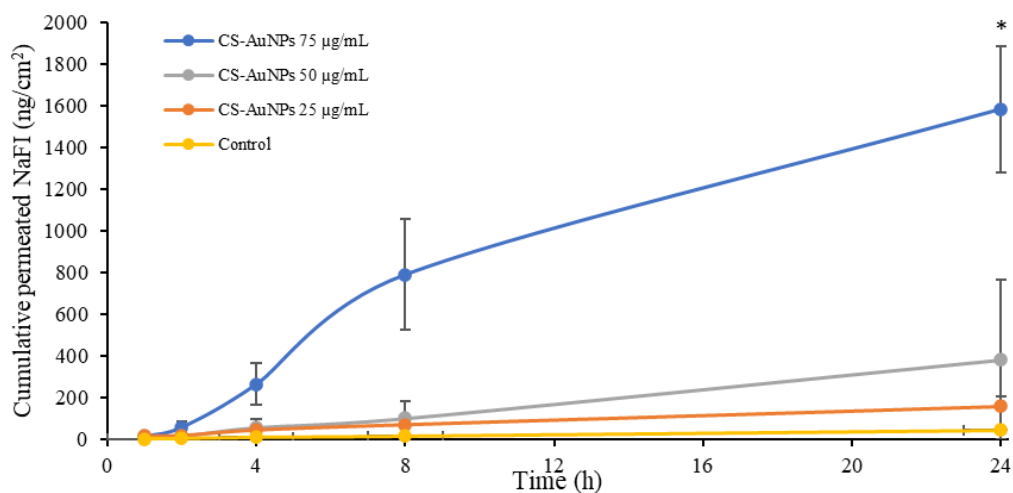


Figure 53 Skin permeation profile of NaFI with different concentrations of CS-AuNPs. NaFI in aqueous solution was used as a control. Each data point represents the mean \pm SD (n=3). * p <0.05 vs control.

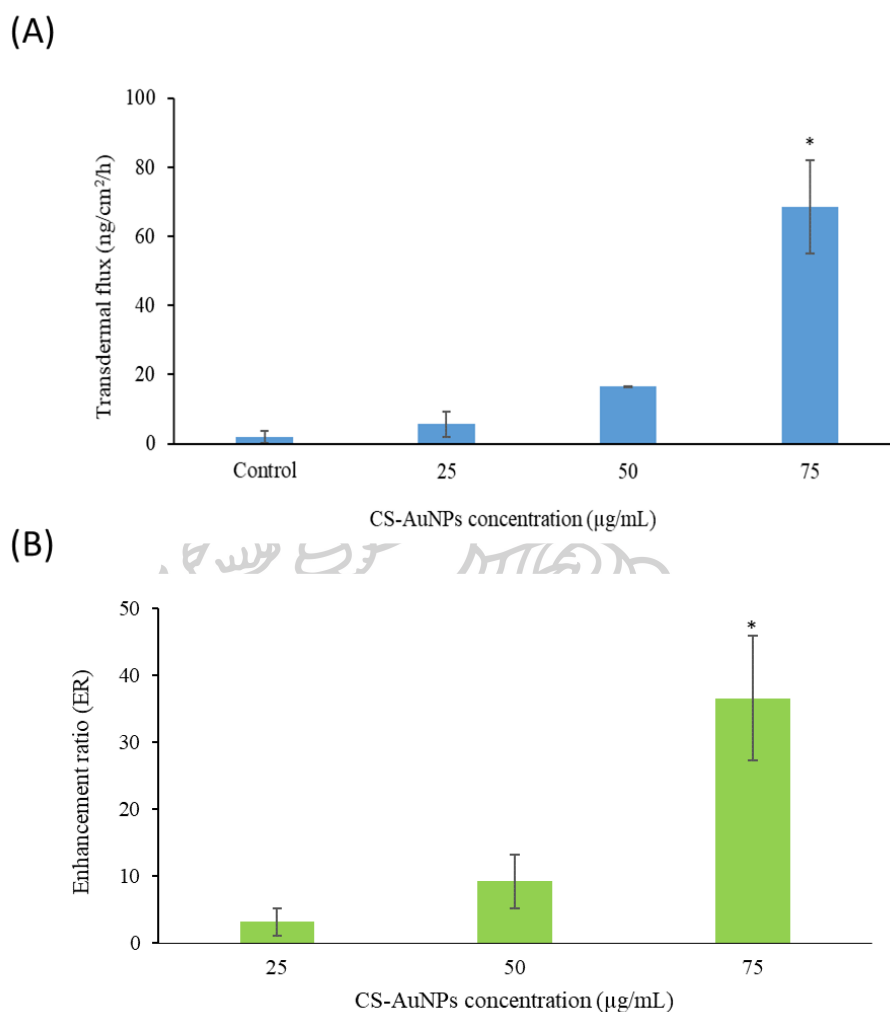


Figure 54 (A) J_{ss} and (B) ER of NaFI with different concentrations of CS-AuNPs. NaFI in aqueous solution was used as a control. Each data point represents the mean \pm SD (n=3). * p <0.05 vs control.

Among the three concentrations of CS-AuNPs, the concentration at 75 µg/mL provided the highest skin permeation of NaFI with an ER of 36.61 ± 9.31 , followed by

the concentrations of 50 and 25 $\mu\text{g/mL}$ with an ER of 9.24 ± 4.00 and 3.15 ± 2.06 , respectively (Figure 54).

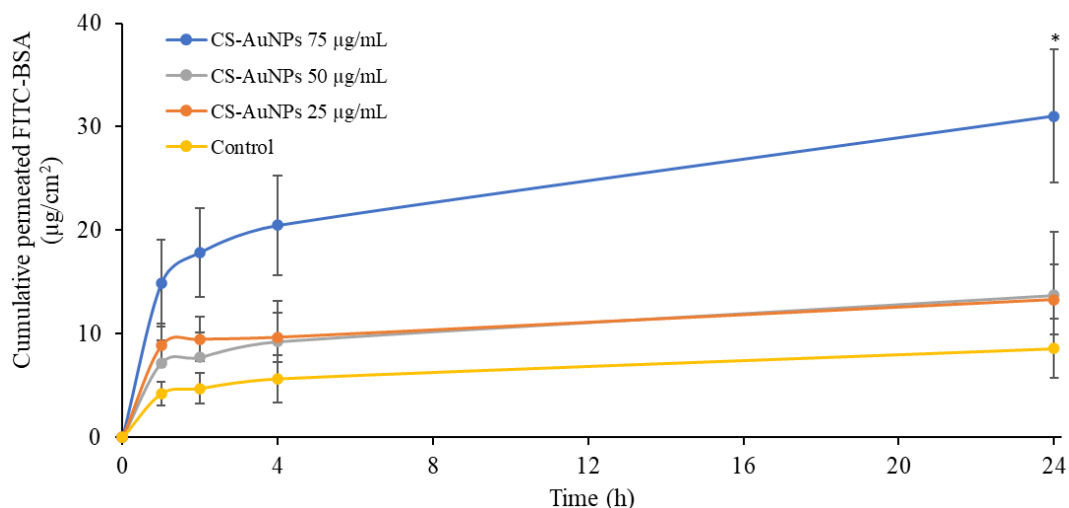


Figure 55 Skin permeation profile of FITC-BSA with different concentrations of CS-AuNPs. FITC-BSA in aqueous solution was used as a control. Each data point represents the mean \pm SD (n=3). * $p < 0.05$ vs control.

Similarly, the highest concentration of CS-AuNPs (75 $\mu\text{g/mL}$) displayed the highest skin permeability of FITC-BSA with an ER of 3.51 ± 1.27 , followed by the concentrations of 50 and 25 $\mu\text{g/mL}$ with an ER of 1.2 ± 0.6 and 1.01 ± 0.2 , respectively (Figure 56). All in all, CS-AuNPs showed the concentration-dependent permeation through the porcine skin membrane for both small and large hydrophilic permeants.

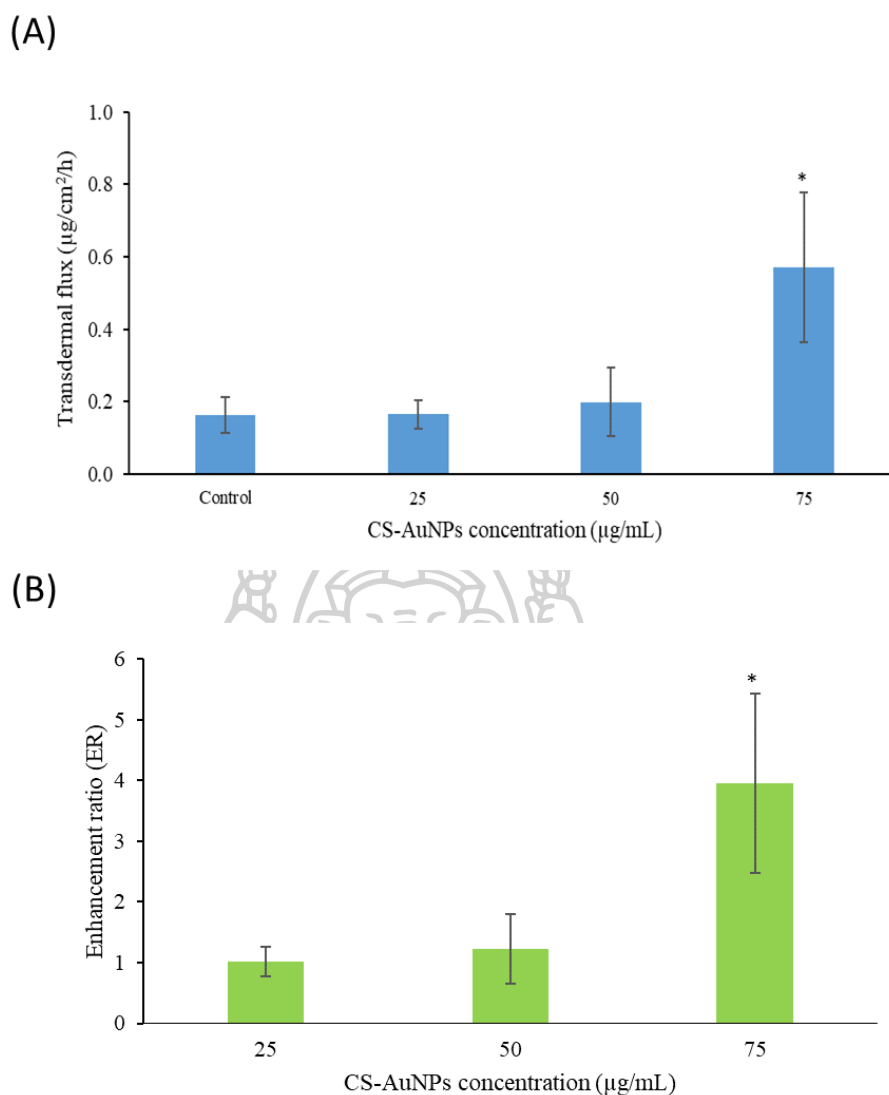


Figure 56 (A) J_{ss} and (B) ER of FITC-BSA with different concentrations of CS-AuNPs. FITC-BSA in aqueous solution was used as a control. Each data point represents the mean \pm SD (n=3). * p <0.05 vs control.

The skin permeation of both small and large hydrophilic molecules across the porcine skin was significantly improved by CS-AuNPs in a concentration dependent manner. The results in the present study were similar to the previous report. Anirudhan and Nair (2018) also demonstrated that the concentration of AuNPs influenced the skin permeability of ketoprofen from transdermal patch. The higher amount of drug was delivered as the amount of AuNPs in the transdermal delivery films increased (15).

4.1.3 CS-AuNPs distribution in skin layers

Following the 24-h skin permeation study, quantitative analysis of Au that resided in the skin and permeated through skin were conducted by ICP-MS. The total recovery of CS-AuNPs in porcine skin was $88.54 \pm 5.30\%$. The results of Au distribution were expressed as percentage in relative to the amount of Au in the donor solutions, as displayed in Figure 57. It was found that $2.62 \pm 0.99\%$ and $0.14 \pm 0.09\%$ of CS-AuNPs were found in the epidermal and dermal layers, respectively. The results from Figure 57 and 58 indicated that CS-AuNPs were mostly retained on the skin surface and penetrated the skin at a very low percentage relative to the of the applied CS-AuNPs ($<5\%$). Also, only $0.03 \pm 0.01\%$ was detected in receptor fluid, suggesting that CS-Au particles could not effectively diffuse across the skin.

Physicochemical properties (size, shape, charge, and surface modification) are important factors that impact the skin absorption of the NPs. It was previously suggested that NPs with particle size less than 4 nm can penetrate the intact skin, whereas NPs larger than 45 nm in size cannot penetrate intact and damaged skin. (157) Additionally, NPs with positive charges are more likely to interact with the cells in the skin. Metallic NPs have been introduced to cosmetology and dermatology for more than 10 years, but their safety has been a concern (158). Cytotoxicity of AuNPs towards human dermal fibroblasts was evaluated previously, AuNPs were not found to reduce the cell viability nor change cell morphology (159). However, AuNPs have been reported to show systemic toxicities to the liver, spleen, and kidney (160). In the present study, owing to the size (>4 nm) and the positively charged surface of CS-AuNPs, they were localized only at the upper skin layers and did not transport across the skin. This suggests that CS-AuNPs would not reach systemic circulation following the topical application. Still, the possible systemic toxicity of CS-AuNPs should be investigated to confirm their safety.

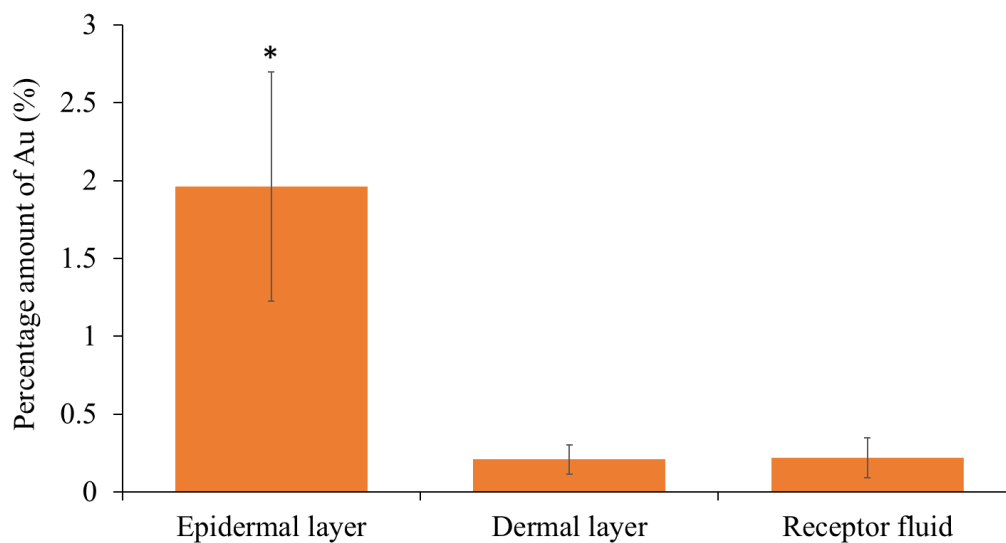


Figure 57 The percentage amount of Au found in the epidermal layer, dermal layer, and receptor fluid after 24-h skin permeation test. *Significant difference ($p < 0.05$) vs receptor fluid.



Figure 58 TEM images of CS-AuNPs (shown as small particles in the circled area) in the SC layer of porcine skin.

4.1.4 Skin penetration pathways

Generally, there are two pathways that skin allows the external substances to penetrate, namely transappendageal and transepidermal route. The transappendageal route is the diffusion through sweat ducts and hair follicles, where the polar as well as

large compounds can utilize. Whereas, transepidermal pathway includes the penetration through the lipid layers surrounding the corneocytes and the transportation across alternate layers of skin cells and lipid matrix. Low MW lipophilic permeants typically diffuse through intercellular lipids, while most hydrophilic permeants are precluded (161). CS-AuNPs were selected as skin penetration enhancer. The model permeants were visualized using CLSM which can be seen as green fluorescence. The regions of interest were the follicular segment and the surrounding area.

The skin samples treated with the model drugs in the aqueous solution (controls) and the combination of each model drug with CS-AuNPs were investigated by CLSM. From CLSM images of NaFI in Figure 59, higher fluorescence signal was observed at the non-follicular areas when the drug was delivered with CS-AuNPs (Figure 59(C)) compared to control (Figure 59(D)). However, no significant difference was noticed between the two groups at the areas close to the follicles (Figure 59(A) and (B)).

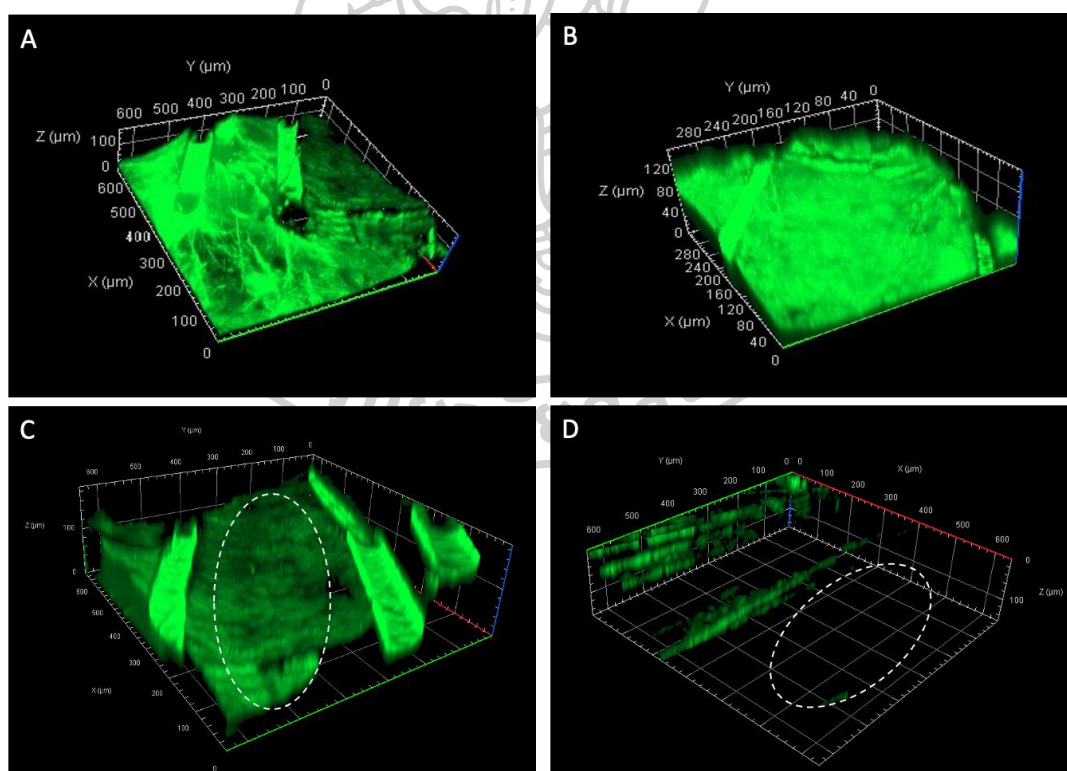


Figure 59 CLSM images of NaFI penetration at the area near the hair follicle of (A) CS-AuNPs group (B) control, and the penetration at non-follicular region (the circled

area) of (C) CS-AuNPs group and (D) control. The semi-cylindrical structures are related to hair shafts.

Accordingly, the greater fluorescence intensity of FITC-BSA was also noted at the non-follicular regions, but not the hair follicle area when treated with CS-AuNPs (Figure 60).

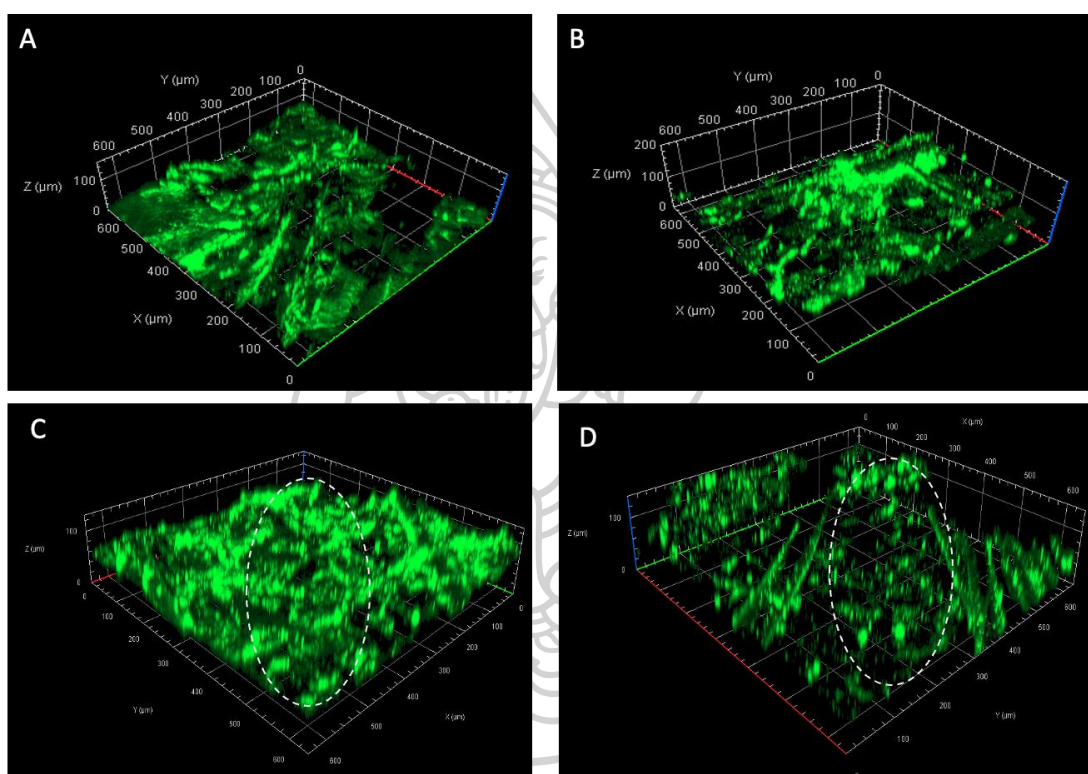


Figure 60 CLSM images of FITC-BSA penetration at the area near the hair follicle of (A) CS-AuNPs, (B) control, and the penetration at non-follicular region (the circled area) of (C) CS-AuNPs group, and (D) control. The semi-cylindrical structures are related to hair shafts.

Hydrophilic molecules, like NaFI and FITC-BSA, commonly diffuse via the hair follicles to reach the deeper layers of skin and are mostly excluded from the transepidermal route due to the SC lipid barrier. Above all, the CLSM results suggested that CS-AuNPs could improve skin penetration of small and large hydrophilic permeants through the transepidermal route and not predominately via the

follicular route. Previous studies suggested that AuNPs can disturb lipid organization and enable exogenous substances to penetrate the SC (15, 17). Also, the enhancement effect could link to the electrostatic interaction between the positive charge on the surface of CS-AuNPs and the negative charge of the skin, thus the skin structure was interrupted. Moreover, the tight junctions (TJ) that are located at the stratum granulosum, the outermost viable layer of the epidermis, are also considered a barrier for transdermal absorption (162, 163). In addition to skin, TJs are also found at other epithelia (e.g., inner ear membranes, GI cavities, and blood vessels) (162-164). A study in mice showed that CS-AuNPs could cause the impairment of TJ proteins (occludin and ZO-1 protein) of the inner ear membranes in mice and resulted in a greater paracellular permeability (165). Furthermore, other studies also showed that AuNPs could alter the TJ proteins at the blood-brain barrier (166) and the colorectal endothelial cells (167). However, the effects of CS-AuNPs on skin TJs are not yet explored and further studies are required.

4.1.5 Cytotoxicity of CS-AuNPs

To initially determine the safety of CS-AuNPs towards human skin cells, cytotoxicity was evaluated using MTT assay. The cell viability of normal human fibroblasts (NHF) and keratinocytes (HaCaT) following 24-h treatment with CS-AuNPs at the concentration ranging from 10 to 100 $\mu\text{g/mL}$ are presented in Figure 61.

For NHF, no significant depletion of cell viability was observed for CS-AuNPs at all tested concentrations, as demonstrated in Figure 61(A). On the other hand, the viability of HaCaT cells was significantly reduced to $77.29 \pm 6.16\%$ and $39.50 \pm 6.35\%$ at the concentration of 75 and 100 $\mu\text{g/mL}$, respectively, as shown in Figure 61(B). According to the ISO guidance (ISO 10993-5), the viability of $<70\%$ of the blank indicates a cytotoxic potential. Thus, CS-AuNPs at the concentration more than 100 $\mu\text{g/mL}$ might cause the cytotoxicity toward human keratinocytes. However, CS-AuNPs were considered safe at the concentration $\leq 75 \mu\text{g/mL}$ despite the significant decrease in cell viability, whereas 75 $\mu\text{g/mL}$ was the concentration of CS-AuNPs used in skin permeation study.

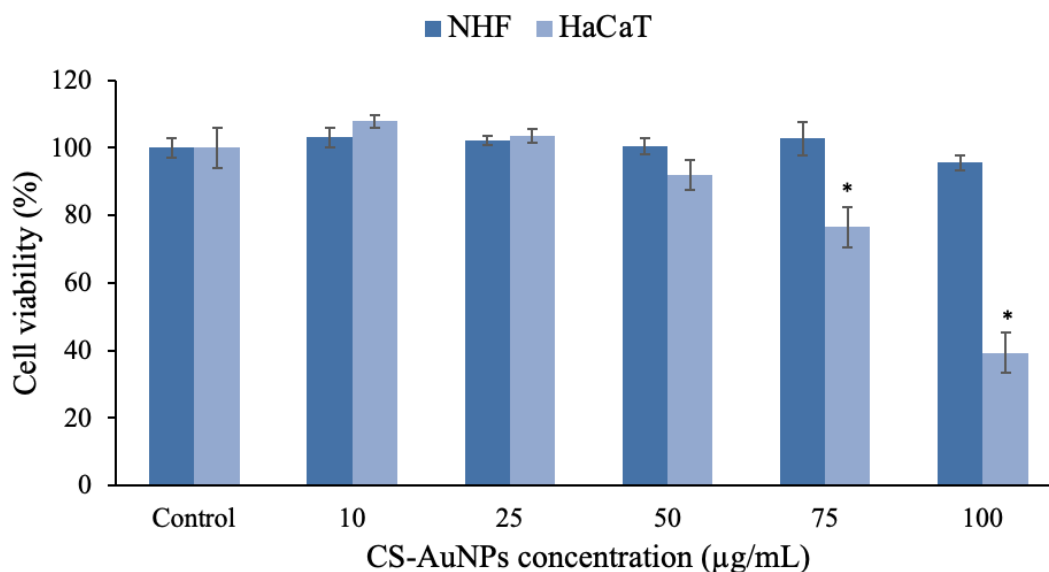


Figure 61 Cell viability of NHF and HaCaT following the 24 h-treatment with CS-AuNPs at different concentrations *Statistically significant ($p < 0.05$) vs untreated control.

4.1.6 Stability of AuNPs

The synthesized AuNPs were well-preserved at 4°C and the stability was evaluated every 7 days up to 28 days. Particle size, polydispersity index (PDI) and zeta potential (ZP) were measured using a Zetasizer, and the results are shown in Table 2. The characteristics of CS-AuNPs had no significant changes for up to 14 days, however, significant increase in the particle size, PDI, and ZP were observed on day 21. Still, CS-AuNPs remained in a nano-size range (1-100 nm) over a period of 28 days; whereas the significant increase in the particle size and PDI of Ci-AuNPs was noticed on day 7, and the size became larger than 100 nm on day 14.

The particle stability and aggregation depend on the properties of the surface. The methods that are widely applied to prevent the agglomeration of particles include electrostatic repulsion and steric exclusion. Electrostatic stabilization involves the repulsive force of either positive or negative charge on particle surfaces, whereas steric stabilization employs the adsorption of polymer to serve as a barrier that restrict the agglomeration of particles (168, 169). CS-AuNPs had chitosan, which is a long chain polymer with positive charge of protonated amine, adsorbed on its surface. The

adsorbing layers of chitosan provided AuNPs both electrostatic and steric stabilization against the coagulation of particles and resulted in greater repulsion force. Ci-AuNPs were surrounded by small molecules, citrate ions, which only electrostatic stabilization was accommodated. The schematic structure of CS-AuNPs and Ci-AuNPs were illustrated in Figure 62. With a ZP of less than -30 mV, Ci-AuNPs are considered stable because the electric repulsion is high enough to prevent aggregation (170). However, colloidal systems, such as AuNP dispersions, are thermodynamically unstable, so the particles tend to form larger clusters over time to reach the thermodynamic equilibrium state. As described by DLVO theory, when two particles approach each other, the Van Der Waals attraction force increases. To reduce their energy level, the particles may stay at the secondary minimum, where the particles are loosely packed and usually easily redispersed (flocculation). This phenomenon could account for the significant increase in DLS observed in Ci-AuNPs (170, 171).

Table 2 The stability of Ci-AuNPs and CS-AuNPs

Formulations	Properties	Day				
		0	7	14	21	28
CS-AuNPs	Particle size (nm)	38.23±0.59	38.21±0.20	38.25±1.06	43.41±0.16*	56.22±1.71*
	PDI	0.36±0.04	0.33±0.02	0.36±0.04	0.45±0.02*	0.44±0.01*
	ZP (mV)	30.37±0.83	30.80±0.85	30.03±0.74	34.80±1.14*	37.27±0.49*
Ci-AuNPs	Particle size (nm)	32.20±0.71	63.21±2.45*	110.31±5.10*	253.89±4.56*	279.91±8.78*
	PDI	0.33±0.01	0.54±0.15*	0.58±0.09*	0.73±0.05*	0.85±0.06*
	ZP (mV)	-60.21±0.41	-58.77±1.71	-61.28±0.53	-60.33±0.74	-65.37±1.58

*Statistically significant ($p < 0.05$) vs day 0

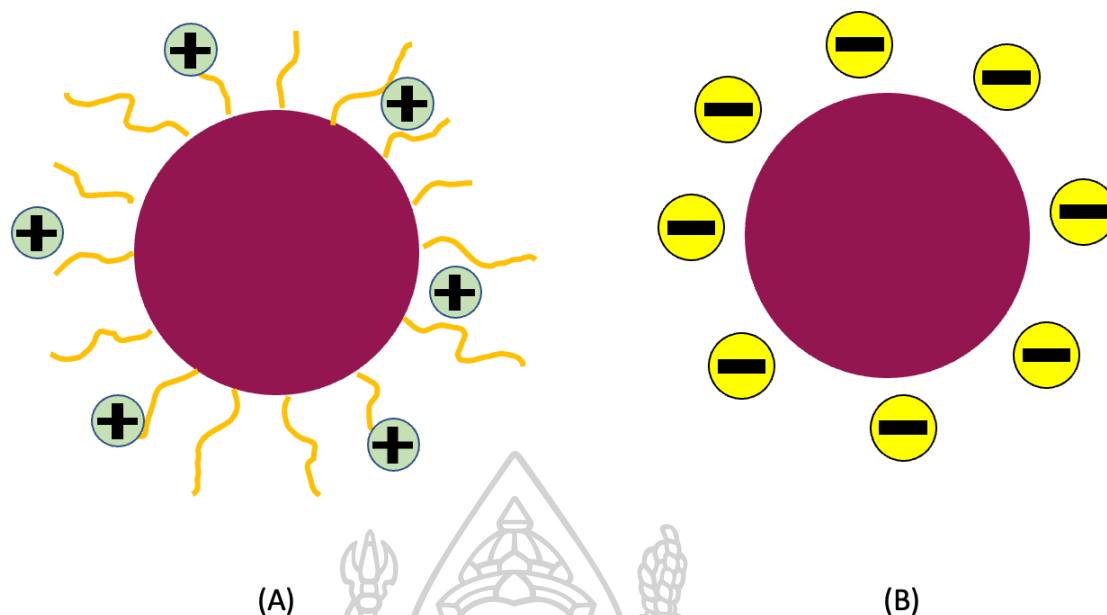


Figure 62 Illustrations of (A) CS-AuNPs and (B) Ci-AuNPs.

4.2 Development and fabrication of DMNs



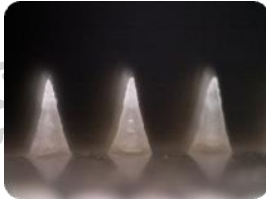
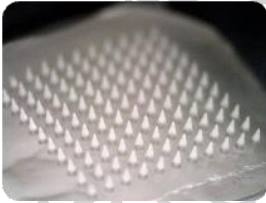

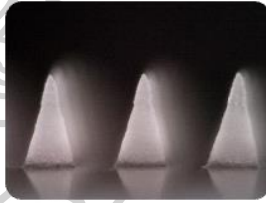
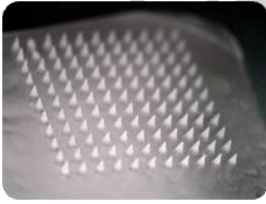

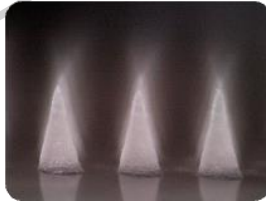


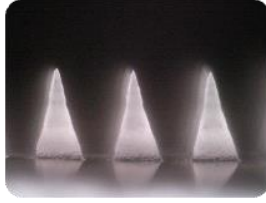
The MNs used in this study were made from 5 % HA, 10 % PVA, and 40 % PVP. At the preliminary stage, the polymers were mixed at three different ratios (1:0:2, 1:0.5:2, and 1:1:1) to fabricate the MNs and their dissolution time was evaluated. With the polymer ratio of 1:0:2 and 1:0.5:2, the fabricated MNs were completely dissolved at 30 and 20 min, respectively. Whereas at the ratio of 1:1:1, the MNs were not dissolved but swelled. Thus, the ratio of 1:0.5:2 was selected for MNs fabrication and used in further studies since it had the fastest dissolution time.

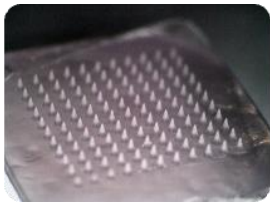





4.2.1 Physical appearance of DMNs and Au-DMNs

CS-AuNPs were selected as they showed potential for skin penetration enhancement. The CS-AuNPs dispersion was incorporated into the mixture of polymer blend at the amount ranging from 0.17 to 1.13 mg per MNs patch to fabricate the microneedles, and their physical appearance was visualized by a digital microscope (Dino-Lite™ Edge/5MP, Hsinchu, Taiwan), as presented in Table 3. Blank DMNs were completely formed with strong and elegant appearance. Also, CS-AuNPs could be loaded up to 15 %wt without causing any noticeable changes to the

needles. Also, the completion of MNs fabrication was confirmed by SEM performing at 10 kV and $225\times$ magnification, as demonstrated in Figure 63.

Table 3 Physical appearance of fabricated MNs under microscope

CS-AuNPs (mg) loaded in a MNs patch	Top view	Side view	Close-up view	Description
0 (blank)				All needles are fully formed with strong and elegant appearance.
0.17				All needles are fully formed with strong and elegant appearance.
0.40				All needles are fully formed with strong and elegant appearance.
0.57				All needles are fully formed with strong and elegant appearance.

0.85				All needles are fully formed with strong and elegant appearance.
1.13				All needles are fully formed and soft.

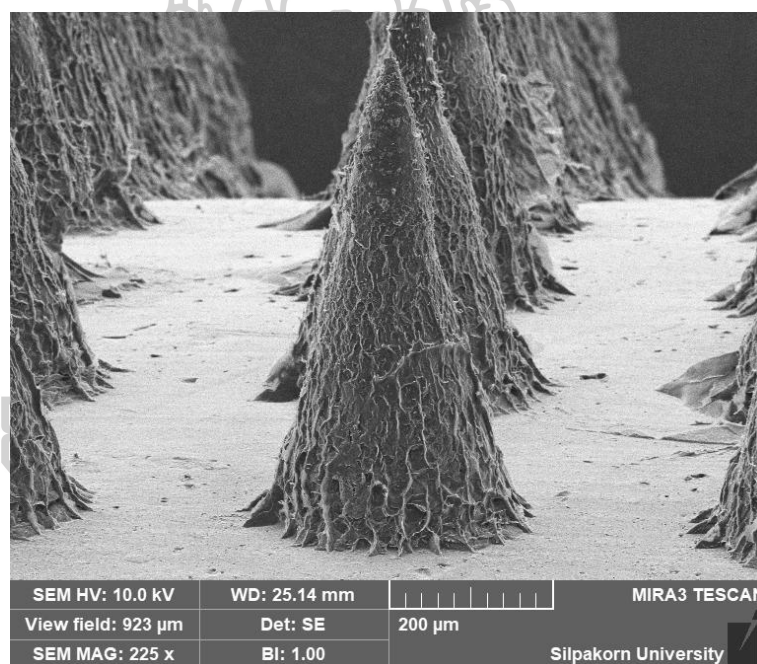


Figure 63 SEM image of 15%wt CS-AuNPs-loaded MNs performing at 10 kV and 225 \times magnification.

4.2.2 Mechanical strength evaluation

The mechanical strength of the MNs was evaluated using a texture analyzer in a compression mode. The compression force was set at 10.769 N per 121 needles with the speed of 0.5 mm per second. The percentage of height reduction was plotted and presented in Figure 64. From the evaluation result, a significant increase in %height

reduction was observed at 20 %wt incorporation of CS-AuNPs. This suggested that the combination of CS-AuNPs could reduce the mechanical strength of MNs. Thus, 15%wt was the optimal content that was selected for further studies.

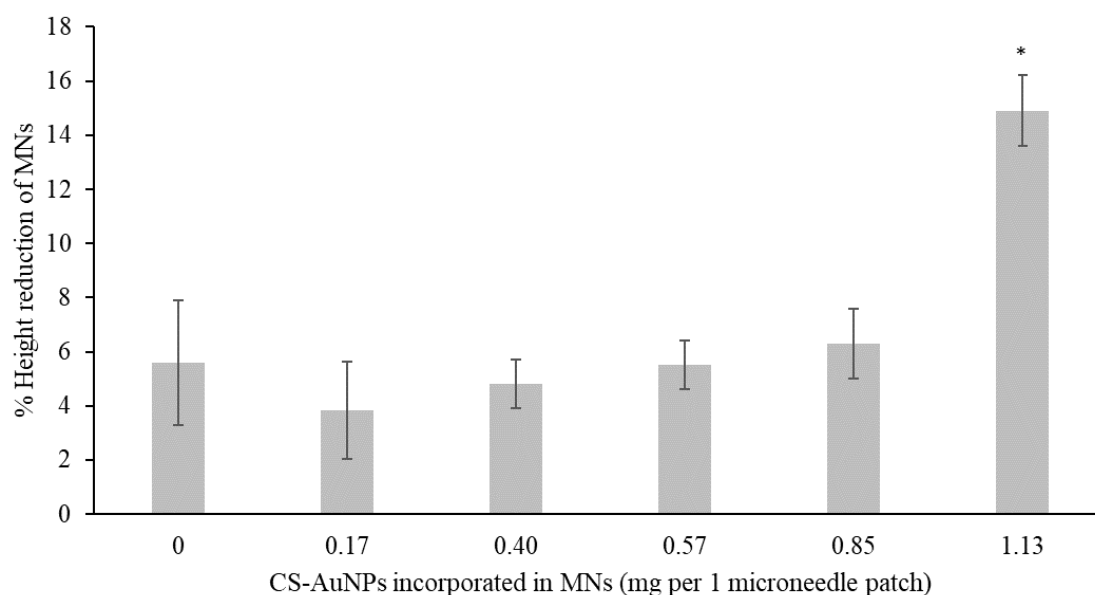


Figure 64 Percentage height reduction of MNs after compressing with the force at 10.769 N per 121 needles with the speed of 0.5 mm per second. *Statistically significant ($p < 0.05$) vs control (Blank MNs).

4.2.3 Skin insertion

The fabricated MNs were tested for their capability to be inserted into a full thickness of the neonatal porcine skin using thumb pressure. The microholes created by the MNs were stained with methylene blue and the percentage of penetration was calculated. From the result in Figure 65, DMNs and 15 %wt Au-MNs had %penetration of almost 100%. These results revealed successful and efficient insertion of MNs, indicated that the fabricated MNs were strong enough to pierce through the SC layers of skin.

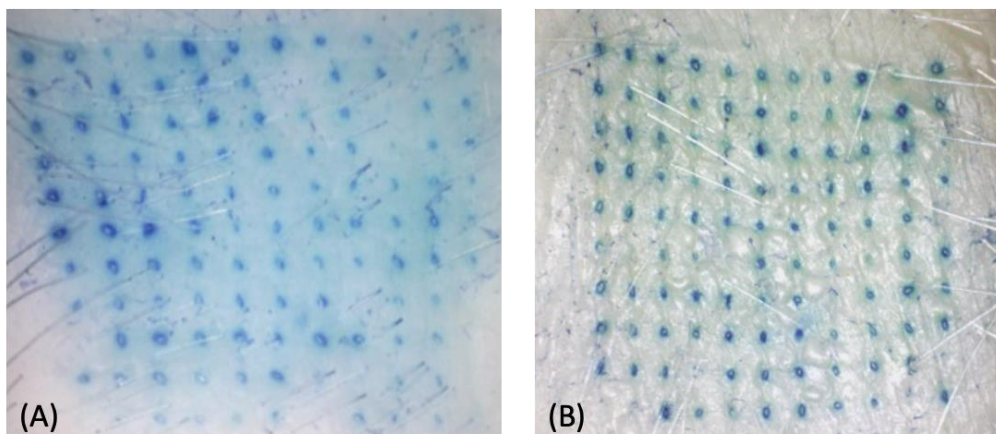


Figure 65 Stained microholes on porcine skin following the insertion of (A) DMNs and (B) 15% wt CS-AuNPs loaded MNs.

4.3.4. *Ex vivo* skin dissolution study

DMNs can dissolve in the skin physiological conditions where the entrapped drug is released. The *in vitro* skin dissolution study was performed to predict the drug release from the MNs. The results in Figure 66 showed the dissolution behavior of the fabricated MNs under the conditions that mimic the physiological environment. From the result, both DMNs and Au-MNs began to dissolve after 10 min and completely dissolved in 20 min. The result suggested the incorporation of CS-AuNPs did not affect the dissolution of polymer under physiological condition.

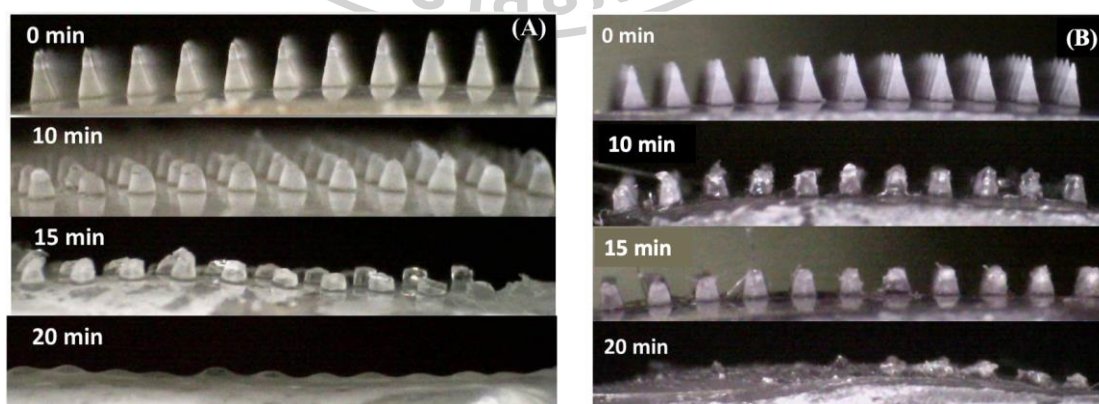


Figure 66 *Ex vivo* skin dissolution of (A) DMNs and (B) 15% wt CS-AuNPs loaded MNs at different time points in an incubator at the temperature of 37 ± 1 °C.

4.3.5 *In vitro* skin permeation of AuNPs loading MNs (Au-MNs)

The effects of Au-MNs on skin permeation of hydrophilic molecules were examined using vertical Franz diffusion cells. Skin permeation profiles of NaFI and FITC-BSA entrapped in DMNs and Au-MNs are presented in Figure 67 and 68, respectively. From the results, no significant difference of skin permeation was noted between DMNs (control) and Au-MNs groups for both NaFI and FITC-BSA.

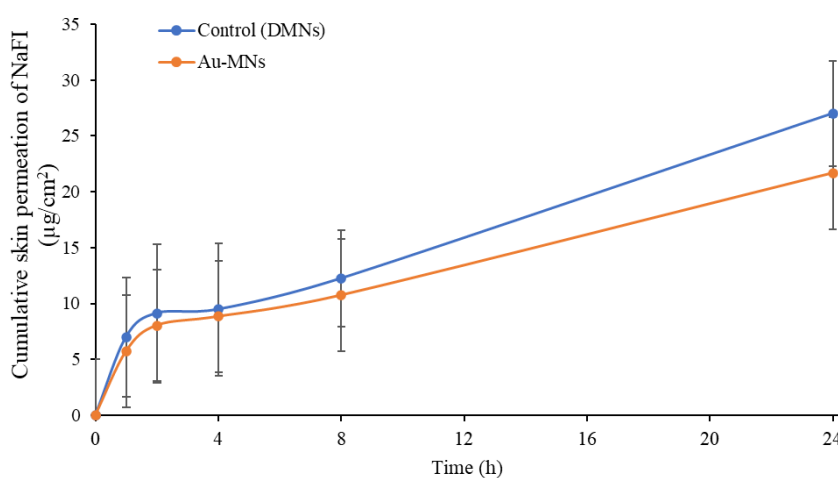


Figure 67 Skin permeation profile of NaFI entrapped in DMNs and Au-MNs. Each data point represents the mean \pm SD (n=3).

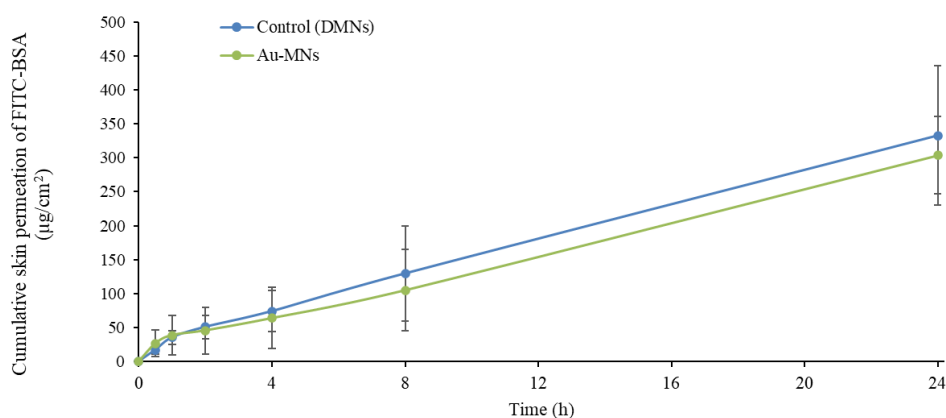


Figure 68 Skin permeation profile of FITC-BSA entrapped in DMNs and Au-MNs. Each data point represents the mean \pm SD (n=3).

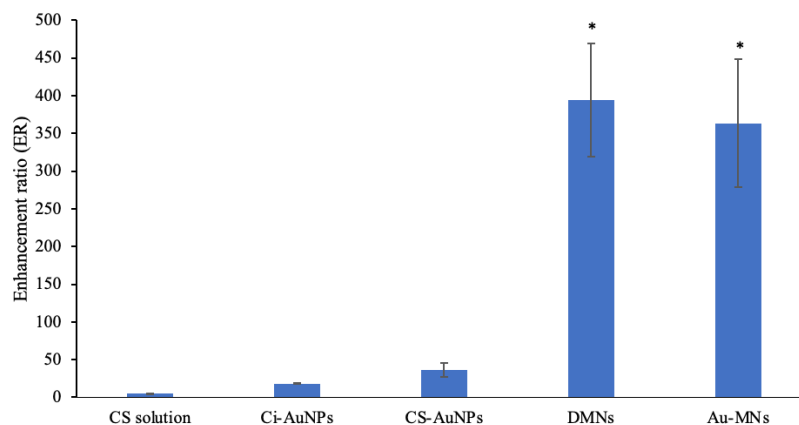


Figure 69 The enhancement ratios of NaFI entrapped in DMNS and Au-MNs compared to AuNPs. Each data point represents the mean \pm SD (n=3) *Statistically significant ($p<0.05$) vs CS-AuNPs.

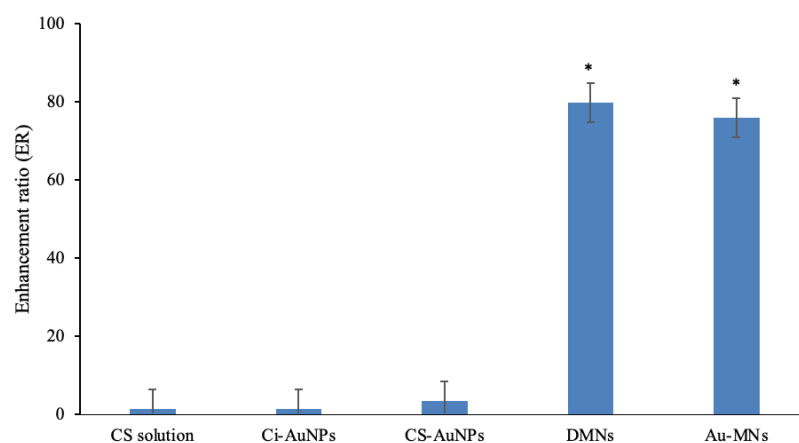


Figure 70 The enhancement ratios of FITC-BSA entrapped in DMNS and Au-MNs compared to AuNPs. Each data point represents the mean \pm SD (n=3) *Statistically significant ($p<0.05$) vs CS-AuNPs.

AuNPs acted as a skin permeation enhancer by disrupting the SC structure, so the drug permeation could be enhanced (172). However, compared to the CS-AuNPs, MNs provided much higher improvement in the skin permeation of the drugs. Most of the drug molecules permeated through the SC shortcuts created by the MNs and were directly delivered to the deep skin layer, regardless of AuNPs. Therefore, the

combination of AuNPs and MNs had no synergistic effect on the skin permeation enhancement.

4.3.6 Stability of Au-MNs

After being stored at 25 ± 2 °C and 75 ± 5 %RH, the fabricated Au-MNs showed good physical stability. The Au-MNs did not show changes in their color nor appearances. In addition, the Au-MNs remained their good mechanical strength during the 6-month period of the stability study (Figure 69).

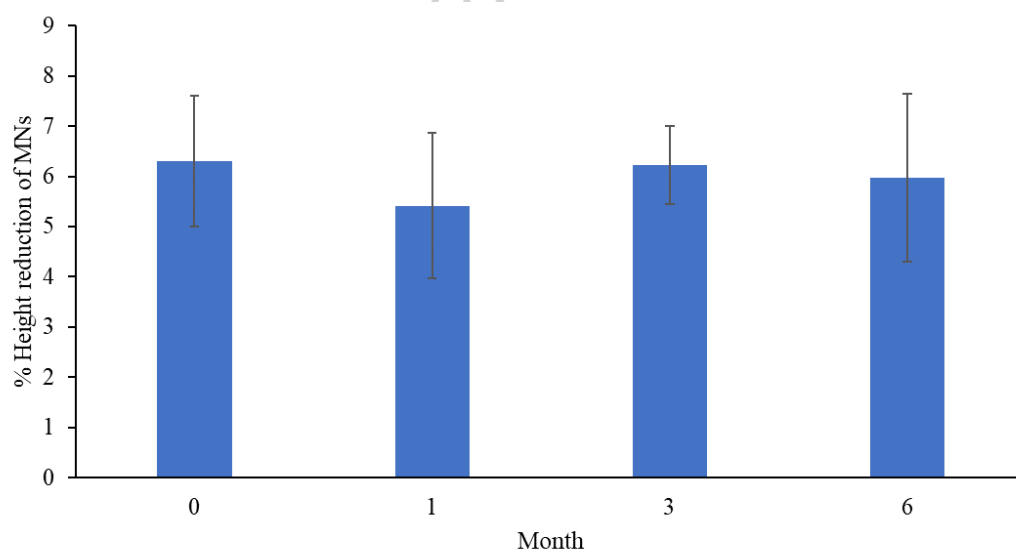


Figure 71 Mechanical strength during 6-month stability study of Au-MNs (expressed as percentage height reduction after compressing with the force at 10.769 N per 121 needles with the speed of 0.5 mm per second).

CHAPTER 5

CONCLUSIONS

5.1 The study of AuNPs on skin permeation

The synthesis of CS-AuNPs were achieved using a microwave synthesizer, whereas Ci-AuNPs were produced by Turkevich method. The particle size of obtained AuNPs were in a nanoscale. CS-AuNPs possessed a positive ZP attributed to the protonated amine on CS structure, while Ci-AuNPs had a negative ZP due to the surrounding citrate ions. In this study, the effect of Ci-AuNPs and CS-AuNPs on skin permeation of two hydrophilic model compounds were demonstrated. The result revealed that CS-AuNPs could improve the skin permeation of both small and large hydrophilic permeants. The CLSM study indicated that the permeation was increased by improving the delivery through transepidermal pathway. In terms of safety, several reports suggested that AuNPs could cause the systemic toxicity in animals following the oral and intraperitoneal administration. This study provided the safety information of CS-AuNPs toward human skin fibroblast assessed by MTT assay. The results indicated that CS-AuNPs were considered safe at the concentration used in the skin study. The distribution study also revealed that CS-AuNPs were mostly retained on upper skin layers and could not effectively transport across the skin. All in all, CS-AuNPs are a promising skin permeation enhancer of hydrophilic compounds in cosmeceutical and pharmaceutical application.

5.2 Development and Fabrication of DMNs

The DMNs were fabricated from 5 % HA, 10 % PVA, and 40 % PVP at the ratio of 1:0.5:2. CS-AuNPs-incorporated in DMNs (Au-MNs) were successfully developed with the maximum CS-AuNPs loading of 15 %wt. The obtained Au-MNs were strong enough to puncture the SC layers of the neonatal porcine skin, as demonstrated by approximately 100% skin insertion. Moreover, the *in vitro* skin dissolution showed that Au-MNs began to dissolve after 10 min and completely dissolved in 20 min. The fabricated Au-MNs also displayed good physical stability at 25 °C 75%RH during the 6-month period of the stability study. With the aim to improve drug delivery, the combination of AuNPs with physical method such as MNs

was suggested. In contrast, this study revealed that CS-AuNPs and MNs in a combination had no synergistic effect to increase skin drug delivery of hydrophilic molecules. However, the physical enhancement methods such as MNs can be used as a supporting tool for the delivery of drug conjugated-AuNPs.



REFERENCES

1. McCrudden MT, Singh TR, Migalska K, Donnelly RF. Strategies for enhanced peptide and protein delivery. *Ther Deliv*. 2013;4(5):593-614.
2. Schoellhammer CM, Blankschtein D, Langer R. Skin permeabilization for transdermal drug delivery: recent advances and future prospects. *Expert Opin Drug Deliv*. 2014;11(3):393-407.
3. Alkilani AZ, McCrudden MT, Donnelly RF. Transdermal drug delivery: innovative pharmaceutical developments based on disruption of the barrier properties of the stratum corneum. *Pharmaceutics*. 2015;7(4):438-70.
4. Anselmo AC, Mitragotri S. An overview of clinical and commercial impact of drug delivery systems. *J Control Release*. 2014;190:15-28.
5. Jeong WY, Kwon M, Choi HE, Kim KS. Recent advances in transdermal drug delivery systems: a review. *Biomater Res*. 2021;25(1):24.
6. N'Da DD. Prodrug strategies for enhancing the percutaneous absorption of drugs. *Molecules*. 2014;19(12):20780-807.
7. Supe S, Takudage P. Methods for evaluating penetration of drug into the skin: A review. *Skin Res Technol*. 2021;27(3):299-308.
8. Songkro S. An overview of skin penetration enhancers: penetration enhancing activity, skin irritation potential and mechanism of action. *Songklanakarin J Sci Technol*. 2009;31(3):299-321.
9. Mitchell MJ, Billingsley MM, Haley RM, Wechsler ME, Peppas NA, Langer R. Engineering precision nanoparticles for drug delivery. *Nat Rev Drug Discov*. 2021;20(2):101-24.
10. Darweesh RS, Ayoub NM, Nazzal S. Gold nanoparticles and angiogenesis: molecular mechanisms and biomedical applications. *Int J Nanomed*. 2019;14:7643-63.
11. Amina SJ, Guo B. A Review on the Synthesis and Functionalization of Gold Nanoparticles as a Drug Delivery Vehicle. *Int J Nanomed*. 2020;15:9823-57.
12. Raju G, Katiyar N, Vadukumpully S, Shankarappa SA. Penetration of gold nanoparticles across the stratum corneum layer of thick-Skin. *J Dermatol Sci*.

2018;89(2):146-54.

13. Sonavane G, Tomoda K, Sano A, Ohshima H, Terada H, Makino K. In vitro permeation of gold nanoparticles through rat skin and rat intestine: effect of particle size. *Colloids Surf B Biointerfaces*. 2008;65(1):1-10.
14. Hao F, Jin X, Liu QS, Zhou Q, Jiang G. Epidermal penetration of gold nanoparticles and its underlying mechanism based on human reconstructed 3D Episkin model. *ACS Appl Mater Interfaces*. 2017;9(49):42577-88.
15. Anirudhan TS, Nair SS. Gold nanoparticle and hydrophobic nanodiamond based synergistic system: a way to overcome skin barrier function. *Bioconjug Chem*. 2018;29(10):3262-72.
16. Gupta R, Kashyap N, Rai B. Transdermal cellular membrane penetration of proteins with gold nanoparticles: a molecular dynamics study. *Phys Chem Chem Phys*. 2017;19(11):7537-45.
17. Huang Y, Yu F, Park YS, Wang J, Shin MC, Chung HS, et al. Co-administration of protein drugs with gold nanoparticles to enable percutaneous delivery. *Biomaterials*. 2010;31(34):9086-91.
18. Zhang Y, Yu J, Kahkoska AR, Wang J, Buse JB, Gu Z. Advances in transdermal insulin delivery. *Adv Drug Deliv Rev*. 2019;139:51-70.
19. Aung NN, Myat YY, Ngawhirunpat T, Rojanarata T, Patrojanasophon P, Opanasopit P, et al. Evaluation of Thermally Crosslinked Poly(Acrylic Acid-Co-Maleic Acid) (PAMA)/Poly(Vinyl Alcohol) (PVA) Microneedle Arrays. *Key Eng Mater*. 2019;819:45-50.
20. Aung NN, Ngawhirunpat T, Rojanarata T, Patrojanasophon P, Opanasopit P, Pamornpathomkul B. HPMC/PVP Dissolving Microneedles: a Promising Delivery Platform to Promote Trans-Epidermal Delivery of Alpha-Arbutin for Skin Lightening. *AAPS PharmSciTech*. 2019;21(1):25.
21. Ita K. Transdermal Delivery of Drugs with Microneedles-Potential and Challenges. *Pharmaceutics*. 2015;7(3):90-105.
22. He X, Sun J, Zhuang J, Xu H, Liu Y, Wu D. Microneedle System for Transdermal Drug and Vaccine Delivery: Devices, Safety, and Prospects. *Dose Response*.

2019;17(4):1559325819878585.

23. Guillot AJ, Cordeiro AS, Donnelly RF, Montesinos MC, Garrigues TM, Melero A. Microneedle-Based Delivery: An Overview of Current Applications and Trends. *Pharmaceutics*. 2020;12(6).
24. Aung NN, Ngawhirunpat T, Rojanarata T, Patrojanasophon P, Opanasopit P, Pamornpathomkul B. Enhancement of transdermal delivery of resveratrol using Eudragit and polyvinyl pyrrolidone-based dissolving microneedle patches. *J Drug Deliv Sci Technol*. 2021;61.
25. Aung NN, Ngawhirunpat T, Rojanarata T, Patrojanasophon P, Pamornpathomkul B, Opanasopit P. Fabrication, characterization and comparison of alpha-arbutin loaded dissolving and hydrogel forming microneedles. *Int J Pharm*. 2020;586:119508.
26. Kanitakis J. Anatomy, histology and immunohistochemistry of normal human skin. *Eur J Dermatol*. 2002;12(4):390-9; quiz 400-1.
27. James WDBTGEDMORB. *Andrews' diseases of the skin : clinical dermatology*. Philadelphia: Saunders Elsevier; 2006.
28. Baroni A, Buommino E, De Gregorio V, Ruocco E, Ruocco V, Wolf R. Structure and function of the epidermis related to barrier properties. *Clinics in Dermatology*. 2012;30(3):257-62.
29. Kolarsick P, Kolarsick MA, Goodwin C. *Anatomy and Physiology of the Skin*. *Journal of the Dermatology Nurses' Association*. 2011;3:203-13.
30. Yang G, Seok JK, Kang HC, Cho Y-Y, Lee HS, Lee JY. Skin Barrier Abnormalities and Immune Dysfunction in Atopic Dermatitis. *Int J Mol Sci*. 2020;21(8):2867.
31. Chu DH. Chapter 7. Development and Structure of Skin. In: Goldsmith LA, Katz SI, Gilchrist BA, Paller AS, Leffell DJ, Wolff K, editors. *Fitzpatrick's Dermatology in General Medicine*, 8e. New York, NY: The McGraw-Hill Companies; 2012.
32. Prost-Squarcioni C, Freitag S, Heller M, Boehm N. Functional histology of dermis. *Ann Dermatol Venereol*. 2008;135(1 Pt 2):1s5-20.
33. Betzalel N, Feldman Y, Ishai P. The Modeling of the Absorbance of Sub-THz Radiation by Human Skin. *IEEE Transactions on Terahertz Science and Technology*.

2017;PP:1-8.

34. Mishra DK, Pandey V, Maheshwari R, Ghode P, Tekade RK. Chapter 15 - Cutaneous and Transdermal Drug Delivery: Techniques and Delivery Systems. In: Tekade RK, editor. *Basic Fundamentals of Drug Delivery*: Academic Press; 2019. p. 595-650.
35. Schmieder S, Patel P, Krishnamurthy K. Research Techniques Made Simple: Drug Delivery Techniques, Part 1: Concepts in Transepidermal Penetration and Absorption. *J Invest Dermatol*. 2015;135(11):1-5.
36. Razavi H, Darvishi M, Janfaza S. Silver Sulfadiazine Encapsulated in Lipid-Based Nanocarriers for Burn Treatment. *J Burn Care Res*. 2017;39.
37. Kováčik A, Kopečná M, Vávrová K. Permeation enhancers in transdermal drug delivery: benefits and limitations. *Expert Opin Drug Deliv*. 2020;17(2):145-55.
38. Marwah H, Garg T, Goyal AK, Rath G. Permeation enhancer strategies in transdermal drug delivery. *Drug Deliv*. 2016;23(2):564-78.
39. Al Hanbali OA, Khan HMS, Sarfraz M, Arafat M, Ijaz S, Hameed A. Transdermal patches: Design and current approaches to painless drug delivery. *Acta Pharm*. 2019;69(2):197-215.
40. Giri TK, Chakrabarty S, Ghosh B. Transdermal reverse iontophoresis: A novel technique for therapeutic drug monitoring. *J Control Release*. 2017;246:30-8.
41. Wang Y, Zeng L, Song W, Liu J. Influencing factors and drug application of iontophoresis in transdermal drug delivery: an overview of recent progress. *Drug Deliv Transl Res*. 2022;12(1):15-26.
42. Li Y, Yang J, Zheng Y, Ye R, Liu B, Huang Y, et al. Iontophoresis-driven porous microneedle array patch for active transdermal drug delivery. *Acta Biomaterialia*. 2021;121:349-58.
43. Ma S, Liu C, Li B, Zhang T, Jiang L, Wang R. Sonophoresis Enhanced Transdermal Delivery of Cisplatin in the Xenografted Tumor Model of Cervical Cancer. *Onco Targets Ther*. 2020;13:889-902.
44. Ita K. Recent progress in transdermal sonophoresis. *Pharm Dev Technol*. 2017;22(4):458-66.

45. Herwadkar A, Sachdeva V, Taylor LF, Silver H, Banga AK. Low frequency sonophoresis mediated transdermal and intradermal delivery of ketoprofen. *Int J Pharm.* 2012;423(2):289-96.
46. Seah BC, Teo BM. Recent advances in ultrasound-based transdermal drug delivery. *Int J Nanomedicine.* 2018;13:7749-63.
47. Park J, Lee H, Lim GS, Kim N, Kim D, Kim YC. Enhanced Transdermal Drug Delivery by Sonophoresis and Simultaneous Application of Sonophoresis and Iontophoresis. *AAPS PharmSciTech.* 2019;20(3):96.
48. Vaidya J, Shende P. Potential of Sonophoresis as a Skin Penetration Technique in the Treatment of Rheumatoid Arthritis with Transdermal Patch. *AAPS PharmSciTech.* 2020;21(5):180.
49. Pamornpathomkul B, Duangjit S, Laohapatarapant S, Rojanarata T, Opanasopit P, Ngawhirunpat T. Transdermal delivery of fluorescein isothiocyanate-dextrans using the combination of microneedles and low-frequency sonophoresis. *Asian Journal of Pharmaceutical Sciences.* 2015;10(5):415-24.
50. Ita K. Perspectives on Transdermal Electroporation. *Pharmaceutics.* 2016;8(1).
51. Cross S, Roberts M. Physical Enhancement of Transdermal Drug Application: Is Delivery Technology Keeping up with Pharmaceutical Development? *Current drug delivery.* 2004;1:81-92.
52. Feng S, Zhu L, Huang Z, Wang H, Li H, Zhou H, et al. Controlled release of optimized electroporation enhances the transdermal efficiency of sinomenine hydrochloride for treating arthritis in vitro and in clinic. *Drug Des Devel Ther.* 2017;11:1737-52.
53. Demir YK, Akan Z, Kerimoglu O. Characterization of polymeric microneedle arrays for transdermal drug delivery. *PLoS One.* 2013;8(10):e77289.
54. Hong X, Wu Z, Chen L, Wu F, Wei L, Yuan W. Hydrogel Microneedle Arrays for Transdermal Drug Delivery. *Nano-Micro Letters.* 2014;6(3):191-9.
55. Zhao Z, Chen Y, Shi Y. Microneedles: a potential strategy in transdermal delivery and application in the management of psoriasis. *RSC Advances.* 2020;10(24):14040-9.

56. Ami Y, Tachikawa H, Takano N, Miki N. Formation of polymer microneedle arrays using soft lithography. *Journal of Micro/Nanolithography, MEMS, and MOEMS*. 2011;10(1):011503.
57. Singh TRR, McMillan H, Mooney K, Alkilani AZ, Donnelly RF. Fabrication of Microneedles. In: Dragicevic N, I. Maibach H, editors. *Percutaneous Penetration Enhancers Physical Methods in Penetration Enhancement*. Berlin, Heidelberg: Springer Berlin Heidelberg; 2017. p. 305-23.
58. Ahmed Saeed Al-Japairai K, Mahmood S, Hamed Almurisi S, Reddy Venugopal J, Rebhi Hilles A, Azmana M, et al. Current trends in polymer microneedle for transdermal drug delivery. *Int J Pharm*. 2020;587:119673.
59. Omolu A, Bailly M, Day RM. Assessment of solid microneedle rollers to enhance transmembrane delivery of doxycycline and inhibition of MMP activity. *Drug Deliv*. 2017;24(1):942-51.
60. Sivamani RK, Liepmann D, Maibach HI. Microneedles and transdermal applications. *Expert Opin Drug Deliv*. 2007;4(1):19-25.
61. Li J, Zeng M, Shan H, Tong C. Microneedle Patches as Drug and Vaccine Delivery Platform. *Curr Med Chem*. 2017;24(22):2413-22.
62. Pamornpathomkul B, Wongkajornsilp A, Laiwattanapaisal W, Rojanarata T, Opanasopit P, Ngawhirunpat T. A combined approach of hollow microneedles and nanocarriers for skin immunization with plasmid DNA encoding ovalbumin. *Int J Nanomed*. 2017;12:885-98.
63. Cheung K, Han T, Das DB. Effect of force of microneedle insertion on the permeability of insulin in skin. *J Diabetes Sci Technol*. 2014;8(3):444-52.
64. Waghule T, Singhvi G, Dubey SK, Pandey MM, Gupta G, Singh M, et al. Microneedles: A smart approach and increasing potential for transdermal drug delivery system. *Biomed Pharmacother*. 2019;109:1249-58.
65. Dardano P, Battisti M, Rea I, Serpico L, Terracciano M, Cammarano A, et al. Polymeric Microneedle Arrays: Versatile Tools for an Innovative Approach to Drug Administration. *Advanced Therapeutics*. 2019;2.

66. Doppalapudi S, Jain A, Khan W, Domb AJ. Biodegradable polymers—an overview. *Polymers for Advanced Technologies*. 2014;25(5):427-35.
67. Larrañeta E, Lutton REM, Woolfson AD, Donnelly RF. Microneedle arrays as transdermal and intradermal drug delivery systems: Materials science, manufacture and commercial development. *Mater Sci Eng R Rep*. 2016;104:1-32.
68. Ahmed Saeed Al-Japairai K, Mahmood S, Hamed Almurisi S, Reddy Venugopal J, Rebhi Hilles A, Azmana M, et al. Current trends in polymer microneedle for transdermal drug delivery. *International journal of pharmaceutics*. 2020;587:119673-.
69. Yu J, Zhang Y, Ye Y, DiSanto R, Sun W, Ranson D, et al. Microneedle-array patches loaded with hypoxia-sensitive vesicles provide fast glucose-responsive insulin delivery. *Proceedings of the National Academy of Sciences of the United States of America*. 2015;112.
70. Zhang X, Wang Y, Chi J, Zhao Y. Smart Microneedles for Therapy and Diagnosis. *Research (Wash D C)*. 2020;2020:7462915-.
71. Kumar R. Chapter 8 Lipid-Based Nanoparticles for Drug-Delivery Systems. *Nanocarriers for Drug Delivery* 2019. p. 249-84.
72. Singpanna K, Dechsri K, Patrojanasophon P, Limpachayaporn P, Opanasopit P, Nuntharatanapong N. Transdermal delivery, cytotoxicity and anti-melanogenic activity of p-chlorophenyl benzyl ether loaded-liposomes. *J Drug Deliv Sci Technol*. 2021;65:102746.
73. Jash A, Ubeyitogullari A, Rizvi SSH. Liposomes for oral delivery of protein and peptide-based therapeutics: challenges, formulation strategies, and advances. *J Mater Chem B*. 2021;9(24):4773-92.
74. Kumar P, Rajeshwarrao P. Nonionic surfactant vesicular systems for effective drug delivery—An overview. *Acta Pharmaceutica Sinica B*. 2011;1:208–19.
75. Jaiswal M, Dudhe R, Sharma PK. Nanoemulsion: an advanced mode of drug delivery system. *3 Biotech*. 2015;5(2):123-7.
76. Ashaolu TJ. Nanoemulsions for health, food, and cosmetics: a review. *Environmental Chemistry Letters*. 2021;19(4):3381-95.
77. Barradas TN, de Holanda e Silva KG. Nanoemulsions as Optimized Vehicles for

- Essential Oils. In: Saneja A, Panda AK, Lichtfouse E, editors. Sustainable Agriculture Reviews 44: Pharmaceutical Technology for Natural Products Delivery Vol 2 Impact of Nanotechnology. Cham: Springer International Publishing; 2020. p. 115-67.
78. Scioli Montoto S, Muraca G, Ruiz ME. Solid Lipid Nanoparticles for Drug Delivery: Pharmacological and Biopharmaceutical Aspects. *Front Mol Biosci.* 2020;7(319).
79. Uner M. Preparation, characterization and physico-chemical properties of solid lipid nanoparticles (SLN) and nanostructured lipid carriers (NLC): their benefits as colloidal drug carrier systems. *Pharmazie.* 2006;61(5):375-86.
80. Wissing SA, Kayser O, Müller RH. Solid lipid nanoparticles for parenteral drug delivery. *Adv Drug Deliv Rev.* 2004;56(9):1257-72.
81. Pardeike J, Hommoss A, Müller RH. Lipid nanoparticles (SLN, NLC) in cosmetic and pharmaceutical dermal products. *Int J Pharm.* 2009;366(1-2):170-84.
82. Saupe A, Wissing SA, Lenk A, Schmidt C, Müller RH. Solid lipid nanoparticles (SLN) and nanostructured lipid carriers (NLC) -- structural investigations on two different carrier systems. *Biomed Mater Eng.* 2005;15(5):393-402.
83. Borges A, de Freitas V, Mateus N, Fernandes I, Oliveira J. Solid Lipid Nanoparticles as Carriers of Natural Phenolic Compounds. *Antioxidants.* 2020;9(10):998.
84. Zhang Z, Tsai P-C, Ramezanli T, Michniak-Kohn BB. Polymeric nanoparticles-based topical delivery systems for the treatment of dermatological diseases. *Wiley interdisciplinary reviews Nanomedicine and nanobiotechnology.* 2013;5(3):205-18.
85. Zhou X, Hao Y, Yuan L, Pradhan S, Shrestha K, Pradhan O, et al. Nano-formulations for transdermal drug delivery: A review. *Chinese Chemical Letters.* 2018;29(12):1713-24.
86. Wang M, Marepally SK, Vemula PK, Xu C. Chapter 5 - Inorganic Nanoparticles for Transdermal Drug Delivery and Topical Application. In: Hamblin MR, Avci P, Prow TW, editors. *Nanoscience in Dermatology.* Boston: Academic Press; 2016. p. 57-72.
87. Chen X, Li QW, Wang XM. Gold nanostructures for bioimaging, drug delivery and therapeutics. *Precious Metals for Biomedical Applications* 2014. p. 163-76.
88. Hu X, Zhang Y, Ding T, Liu J, Zhao H. Multifunctional gold nanoparticles: a novel

nanomaterial for various medical applications and biological activities. *Front Bioeng Biotechnol.* 2020;8:990.

89. Faridah AB, Rabiatal AZ. The synthesis of gold nanoparticles and its extensive applications. In: Nafarizal N, Soon CF, Khairul Anuar M, editors. *Current Advances in Microdevices and Nanotechnology*. Malaysia: Penerbit UTHM; 2019.
90. Subara D, Jaswir I. Gold Nanoparticles: Synthesis and application for Halal Authentication in Meat and Meat Products. *International Journal on Advanced Science, Engineering and Information Technology.* 2018;8(4-2).
91. Huang X, El-Sayed M. Gold nanoparticles: Optical properties and implementations in cancer diagnosis and photothermal therapy. *J Adv Res.* 2010;1(1):13-28.
92. Thanayutsiri T, Patrojanasophon P, Opanasopit P, Ngawhirunpat T, Plianwong S, Rojanarata T. Rapid synthesis of chitosan-capped gold nanoparticles for analytical application and facile recovery of gold from laboratory waste. *Carbohydr Polym.* 2020;250:116983.
93. Yafout M, Ousaid A, Khayati Y, El Otmani IS. Gold nanoparticles as a drug delivery system for standard chemotherapeutics: A new lead for targeted pharmacological cancer treatments. *Scientific African.* 2021;11.
94. Jeon HB, Tsalu PV, Ha JW. Shape effect on the refractive index sensitivity at localized surface plasmon resonance inflection points of single gold nanocubes with vertices. *Sci Rep.* 2019;9(1):13635.
95. Yeh YC, Creran B, Rotello VM. Gold nanoparticles: preparation, properties, and applications in bionanotechnology. *Nanoscale.* 2012;4(6):1871-80.
96. Jeong H-H, Choi E, Ellis E, Lee T-C. Recent advances in gold nanoparticles for biomedical applications: from hybrid structures to multi-functionality. *J Mater Chem B.* 2019;7(22):3480-96.
97. Elahi N, Kamali M, Baghersad MH. Recent biomedical applications of gold nanoparticles: A review. *Talanta.* 2018;184:537-56.
98. Nejati K, Dadashpour M, Gharibi T, Mellatyar H, Akbarzadeh A. Biomedical Applications of Functionalized Gold Nanoparticles: A Review. *J Clust Sci.* 2021.

99. Zhao P, Li N, Astruc D. State of the art in gold nanoparticle synthesis. *Coordination Chemistry Reviews*. 2013;257(3):638-65.
100. Alba-Molina D, Giner-Casares JJ, Cano M. Bioconjugated plasmonic nanoparticles for enhanced skin penetration. *Top Curr Chem (Cham)*. 2019;378(1):8.
101. Daruich De Souza C, Ribeiro Nogueira B, Rostelato MECM. Review of the methodologies used in the synthesis gold nanoparticles by chemical reduction. *J Alloys Compd*. 2019;798:714-40.
102. Baig N, Kammakam I, Falath W. Nanomaterials: a review of synthesis methods, properties, recent progress, and challenges. *Materials Advances*. 2021;2(6):1821-71.
103. Dong J, Carpinone PL, Pyrgiotakis G, Demokritou P, Moudgil BM. Synthesis of Precision Gold Nanoparticles Using Turkevich Method. *Kona*. 2020;37:224-32.
104. Mohammed I, Al-Gawhari F. Gold nanoparticle: synthesis, functionalization, enhancement, drug delivery and therapy: a review. *Sys Rev Pharm*. 2020;11(6):888-910.
105. Antonio M, Nogueira J, Vitorino R, Daniel-da-Silva AL. Functionalized Gold Nanoparticles for the Detection of C-Reactive Protein. *Nanomaterials (Basel)*. 2018;8(4).
106. Slepicka P, Slepickova Kasalkova N, Siegel J, Kolska Z, Svorcik V. Methods of Gold and Silver Nanoparticles Preparation. *Materials (Basel)*. 2019;13(1).
107. Hamamoto M, Yagyu H. Two-phase Brust-Schiffirin synthesis of gold nanoparticles dispersion in organic solvent on glass microfluidic device. 2017 IEEE 17th International Conference on Nanotechnology (IEEE-NANO). 2017:632-5.
108. Dou X, Wang X, Qian S, Liu N, Yuan X. From understanding the roles of tetraoctylammonium bromide in the two-phase Brust-Schiffirin method to tuning the size of gold nanoclusters. *Nanoscale*. 2020;12(38):19855-60.
109. Fuster MG, Montalban MG, Carissimi G, Lima B, Feresin GE, Cano M, et al. Antibacterial effect of chitosan-gold nanoparticles and computational modeling of the interaction between chitosan and a lipid bilayer model. *Nanomaterials (Basel)*. 2020;10(12).
110. Mohan CO, Gunasekaran S, Ravishankar CN. Chitosan-capped gold nanoparticles for indicating temperature abuse in frozen stored products. *NPJ Sci Food*. 2019;3:2.

111. Huang H, Yang X. Synthesis of Chitosan-Stabilized Gold Nanoparticles in the Absence/Presence of Tripolyphosphate. *Biomacromolecules*. 2004;5(6):2340-6.
112. Abrica-González P, Zamora-Justo JA, Sotelo-López A, Vázquez-Martínez GR, Balderas-López JA, Muñoz-Diosdado A, et al. Gold nanoparticles with chitosan, N-acetylated chitosan, and chitosan oligosaccharide as DNA carriers. *Nanoscale Research Letters*. 2019;14(1):258.
113. Daraee H, Eatemadi A, Abbasi E, Fekri Aval S, Kouhi M, Akbarzadeh A. Application of gold nanoparticles in biomedical and drug delivery. *Artif Cells Nanomed Biotechnol*. 2016;44(1):410-22.
114. Pandey V, Ganeshpurkar A, Thakur A, Sharma M, Rajpoot K, Tekade M, et al. Gold nanoparticles: An advanced drug delivery and diagnostic tool. *The Future of Pharmaceutical Product Development and Research* 2020. p. 609-69.
115. Connor DM, Broome A-M. Chapter Seven - Gold Nanoparticles for the Delivery of Cancer Therapeutics. In: Broome A-M, editor. *Advances in Cancer Research*. 139: Academic Press; 2018. p. 163-84.
116. Singh P, Pandit S, Mokkapati V, Garg A, Ravikumar V, Mijakovic I. Gold Nanoparticles in Diagnostics and Therapeutics for Human Cancer. *Int J Mol Sci*. 2018;19(7).
117. Martinho N, Damgé C, Reis CP. Recent Advances in Drug Delivery Systems. *J biomater nanobiotechnol*. 2011;02(05):510-26.
118. Duncan B, Kim C, Rotello VM. Gold nanoparticle platforms as drug and biomacromolecule delivery systems. *J Control Release*. 2010;148(1):122-7.
119. Du Y, Xia L, Jo A, Davis RM, Bissel P, Ehrich MF, et al. Synthesis and Evaluation of Doxorubicin-Loaded Gold Nanoparticles for Tumor-Targeted Drug Delivery. *Bioconjug Chem*. 2018;29(2):420-30.
120. Wójcik M, Lewandowski W, Król M, Pawłowski K, Mieczkowski J, Lechowski R, et al. Enhancing anti-tumor efficacy of Doxorubicin by non-covalent conjugation to gold nanoparticles - in vitro studies on feline fibrosarcoma cell lines. *PLoS One*. 2015;10(4):e0124955-e.

121. Zabielska-Koczywaś K, Wojtalewicz A, Użarowska E, Klejman A, Wojtkowska A, Dolka I, et al. Distribution of Glutathione-Stabilized Gold Nanoparticles in Feline Fibrosarcomas and Their Role as a Drug Delivery System for Doxorubicin—Preclinical Studies in a Murine Model. *Int J Mol Sci.* 2018;19:1021.
122. Riley MK, Vermerris W. Recent Advances in Nanomaterials for Gene Delivery—A Review. *Nanomaterials (Basel).* 2017;7(5).
123. Klebowski B, Depciuch J, Parlińska-Wojtan M, Baran J. Applications of Noble Metal-Based Nanoparticles in Medicine. *Int J Mol Sci.* 2018;19(12):4031.
124. Shahbazi R, Sghia-Hughes G, Reid JL, Kubek S, Haworth KG, Humbert O, et al. Targeted homology-directed repair in blood stem and progenitor cells with CRISPR nanoformulations. *Nat Mater.* 2019;18(10):1124-32.
125. Roep BO, Wheeler DCS, Peakman M. Antigen-based immune modulation therapy for type 1 diabetes: the era of precision medicine. *Lancet Diabetes Endocrinol.* 2019;7(1):65-74.
126. Joshi HM, Bhumkar DR, Joshi K, Pokharkar V, Sastry M. Gold nanoparticles as carriers for efficient transmucosal insulin delivery. *Langmuir.* 2006;22(1):300-5.
127. Mateu Ferrando R, Lay L, Polito L. Gold nanoparticle-based platforms for vaccine development. *Drug Discov Today Technol.* 2020;38:57-67.
128. Rathinaraj P, Al-Jumaily AM, Huh DS. Internalization: acute apoptosis of breast cancer cells using herceptin-immobilized gold nanoparticles. *Breast Cancer (Dove Med Press).* 2015;7:51-8.
129. Ou J, Zhou Z, Chen Z, Tan H. Optical Diagnostic Based on Functionalized Gold Nanoparticles. *Int J Mol Sci.* 2019;20(18):4346.
130. Khan S, Hasan A, Attar F, Sharifi M, Siddique R, Mraiche F, et al. Gold Nanoparticle-Based Platforms for Diagnosis and Treatment of Myocardial Infarction. *ACS Biomater Sci Eng.* 2020;6(12):6460-77.
131. El-Husseini DM, Helmy NM, Tammam RH. The effect of gold nanoparticles on the diagnostic polymerase chain reaction technique for equine herpes virus 1 (EHV-1). *RSC Advances.* 2016;6(60):54898-903.

132. Rahman WN, Corde S, Yagi N, Abdul Aziz SA, Annabell N, Geso M. Optimal energy for cell radiosensitivity enhancement by gold nanoparticles using synchrotron-based monoenergetic photon beams. *Int J Nanomedicine*. 2014;9:2459-67.
133. Singh RK, Patel KD, Leong KW, Kim HW. Progress in Nanotheranostics Based on Mesoporous Silica Nanomaterial Platforms. *ACS Appl Mater Interfaces*. 2017;9(12):10309-37.
134. Mackey MA, Ali MRK, Austin LA, Near RD, El-Sayed MA. The most effective gold nanorod size for plasmonic photothermal therapy: theory and in vitro experiments. *The journal of physical chemistry B*. 2014;118(5):1319-26.
135. Meir R, Popovtzer R. Cell tracking using gold nanoparticles and computed tomography imaging. *Wiley Interdiscip Rev Nanomed Nanobiotechnol*. 2018;10(2).
136. Yin D, Li X, Ma Y, Liu Z. Targeted cancer imaging and photothermal therapy via monosaccharide-imprinted gold nanorods. *Chemical Communications*. 2017;53(50):6716-9.
137. Murphy CJ, Thompson LB, Alkilany AM, Sisco PN, Boulos SP, Sivapalan ST, et al. The Many Faces of Gold Nanorods. *The Journal of Physical Chemistry Letters*. 2010;1(19):2867-75.
138. MubarakAli D, Thajuddin N, Jeganathan K, Gunasekaran M. Plant extract mediated synthesis of silver and gold nanoparticles and its antibacterial activity against clinically isolated pathogens. *Colloids Surf B Biointerfaces*. 2011;85(2):360-5.
139. Singh RK, Kurian AG, Patel KD, Mandakhbayar N, Lee N-H, Knowles JC, et al. Label-Free Fluorescent Mesoporous Bioglass for Drug Delivery, Optical Triple-Mode Imaging, and Photothermal/Photodynamic Synergistic Cancer Therapy. *ACS Appl Bio Mater*. 2020;3(4):2218-29.
140. Falahati M, Attar F, Sharifi M, Saboury AA, Salihi A, Aziz FM, et al. Gold nanomaterials as key suppliers in biological and chemical sensing, catalysis, and medicine. *Biochimica et Biophysica Acta (BBA) - General Subjects*. 2020;1864(1):129435.
141. Jeynes JCG, Merchant MJ, Spindler A, Wera AC, Kirkby KJ. Investigation of gold nanoparticle radiosensitization mechanisms using a free radical scavenger and protons of

different energies. *Physics in Medicine and Biology*. 2014;59(21):6431-43.

142. Retif P, Pinel S, Toussaint M, Frochot C, Chouikrat R, Bastogne T, et al.

Nanoparticles for Radiation Therapy Enhancement: the Key Parameters. *Theranostics*. 2015;5(9):1030-44.

143. Hsiao PF, Peng S, Tang T-C, Lin S-Y, Tsai H-C. Enhancing the in vivo transdermal delivery of gold nanoparticles using poly(ethylene glycol) and its oleylamine conjugate. *Int J Nanomed*. 2016;11:1867-78.

144. Zsikó, Csányi, Kovács, Budai S, Gácsi, Berkó. Methods to Evaluate Skin Penetration In Vitro. *Scientia Pharmaceutica*. 2019;87(3).

145. Yadav A, Garg V, Gulati M, Bansal P, Bansal K, Kaur P, et al. Design and performance verification of newly developed disposable static diffusion cell for drug diffusion/permeability studies. *Asian Journal of Pharmaceutical and Clinical Research*. 2018;11:1-7.

146. Oh L, Yi S, Zhang D, Shin SH, Bashaw E. In Vitro Skin Permeation Methodology for Over-The-Counter Topical Dermatologic Products. *Ther Innov Regul Sci*. 2019;2168479019875338.

147. Zaid Alkilani A, McCrudden M, Donnelly R. Transdermal Drug Delivery: Innovative Pharmaceutical Developments Based on Disruption of the Barrier Properties of the Stratum Corneum. *Pharmaceutics*. 2015;7:438-70.

148. Nair A, Jacob S, Al-Dhubiab B, Attimarad M, Harsha S. Basic considerations in the dermatokinetics of topical formulations. *Brazilian Journal of Pharmaceutical Sciences*. 2013;49:423-34.

149. Rossetti F, Depieri L, Bentley MVLB. Confocal laser scanning microscopy as a tool for the investigation of skin drug delivery systems and diagnosis of skin disorders. *Confocal Laser Microscopy - Principles and Applications in Medicine, Biology, and the Food Sciences*. 2013:99-140.

150. O'Goshi K, Serup J. Safety of sodium fluorescein for in vivo study of skin. *Skin Res Technol*. 2006;12(3):155-61.

151. Wang Q, Jaimes-Lizcano YA, Lawson LB, John VT, Papadopoulos KD. Improved

dermal delivery of FITC-BSA using a combination of passive and active methods. *J Pharm Sci.* 2011;100(11):4804-14.

152. El-Sayed N, El-Khourdagui L, Schneider M. Chapter 8 - Insights Into Interactions of Gold Nanoparticles With the Skin and Potential Dermatological Applications. In: Hamblin MR, Avci P, Prow TW, editors. *Nanoscience in Dermatology*. Boston: Academic Press; 2016. p. 99-113.

153. Caramella C, Ferrari F, Bonferoni MC, Rossi S, Sandri G. Chitosan and its derivatives as drug penetration enhancers. *J Drug Deliv Sci Technol.* 2010;20:5-13.

154. Lee JS, Oh H, Kim S, Lee JH, Shin YC, Choi WI. A novel chitosan nanosponge as a vehicle for transepidermal drug delivery. *Pharmaceutics.* 2021;13(9).

155. He W, Guo X, Xiao L, Feng M. Study on the mechanisms of chitosan and its derivatives used as transdermal penetration enhancers. *Int J Pharm.* 2009;382(1-2):234-43.

156. Mikusova V, Mikus P. Advances in chitosan-based nanoparticles for drug delivery. *Int J Mol Sci.* 2021;22(17).

157. Wang M, Lai X, Shao L, Li L. Evaluation of immunoresponses and cytotoxicity from skin exposure to metallic nanoparticles. *Int J Nanomedicine.* 2018;13:4445-59.

158. Filon FL, Crosera M, Adami G, Bovenzi M, Rossi F, Maina G. Human skin penetration of gold nanoparticles through intact and damaged skin. *Nanotoxicology.* 2011;5(4):493-501.

159. Penders J, Stolzoff M, Hickey DJ, Andersson M, Webster TJ. Shape-dependent antibacterial effects of non-cytotoxic gold nanoparticles. *Int J Nanomed.* 2017;12:2457-68.

160. Sani A, Cao C, Cui D. Toxicity of gold nanoparticles (AuNPs): A review. *Biochem Biophys Rep.* 2021;26:100991.

161. Shaker DS, Ishak RAH, Ghoneim A, Elhuoni MA. Nanoemulsion: a review on mechanisms for the transdermal delivery of hydrophobic and hydrophilic drugs. *Scientia Pharmaceutica.* 2019;87(3):17.

162. Yokouchi M, Kubo A. Maintenance of tight junction barrier integrity in cell turnover and skin diseases. *Exp Dermatol.* 2018;27(8):876-83.

163. Bäsler K, Bergmann S, Heisig M, Naegel A, Zorn-Kruppa M, Brandner JM. The role of tight junctions in skin barrier function and dermal absorption. *J Control Release*. 2016;242:105-18.
164. Brandner JM, Zorn-Kruppa M, Yoshida T, Moll I, Beck LA, De Benedetto A. Epidermal tight junctions in health and disease. *Tissue Barriers*. 2015;3(1-2):e974451.
165. Lin YC, Shih CP, Chen HC, Chou YL, Sytwu HK, Fang MC, et al. Ultrasound microbubble-facilitated inner ear delivery of gold nanoparticles involves transient disruption of the tight junction barrier in the round window membrane. *Front Pharmacol*. 2021;12:689032.
166. Li C-H, Shyu M-K, Jhan C, Cheng Y-W, Tsai C-H, Liu C-W, et al. Gold nanoparticles increase endothelial paracellular permeability by altering components of endothelial tight junctions, and increase blood-brain barrier permeability in Mice. *Toxicol Sci*. 2015;148(1):192-203.
167. El Hallal R, Lyu N, Wang Y. Effect of cetuximab-conjugated gold nanoparticles on the cytotoxicity and phenotypic evolution of colorectal cancer cells. *Molecules*. 2021;26(3).
168. Selvamani V. Chapter 15 - Stability Studies on Nanomaterials Used in Drugs. In: Mohapatra SS, Ranjan S, Dasgupta N, Mishra RK, Thomas S, editors. *Characterization and Biology of Nanomaterials for Drug Delivery*; Elsevier; 2019. p. 425-44.
169. Stanciu L, Diaz-Amaya S. Chapter 11 - Materials and devices for sensors and detectors: biocatalysts, bioimaging, and devices with integrated biological functionality. In: Stanciu L, Diaz-Amaya S, editors. *Introductory Biomaterials*. Boston: Academic Press; 2022. p. 267-306.
170. Pamies R, Cifre J, Espín V, Collado-González MM, Díaz Baños FG, Torre J. Aggregation behaviour of gold nanoparticles in saline aqueous media. *J Nanopart Res*. 2014;16:2376:1-11.
171. Sotnikov DV, Safenkova IV, Zherdev AV, Avdienko VG, Kozlova IV, Babayan SS, et al. A Mechanism of Gold Nanoparticle Aggregation by Immunoglobulin G Preparation. *Applied Sciences*. 2020;10(2):475.
172. Chen Y, Feng X. Gold nanoparticles for skin drug delivery. *Int J Pharm*.

2022;625:122122.





VITA

NAME Kanokwan Singpanna

DATE OF BIRTH 16 January 1995

PLACE OF BIRTH Chonburi, Thailand

INSTITUTIONS ATTENDED 2019-2023 Doctor of Philosophy, Ph.D. in Pharmaceutical Technology, Silpakorn University, Thailand.
2013-2018 Bachelor Degree, Doctor of Pharmacy (1st Class Honors), Pharmaceutical Technology, Silpakorn University, Thailand

HOME ADDRESS Chonburi, Thailand

PUBLICATION

1. Singpanna K, Chareonying T, Patrojanasophon P, Rojanarata T, Sukma M, Opanasopit P. Fabrication of a floating device of domperidone tablets using 3D-printing technologies. *Key Eng Mater.* 2020;859:289-294
2. Singpanna K, Oekchuae S, Jareonkunmetee K, Athipornchai A, Nuntharatanapong N, Opanasopit P, Limpachayaporn P. Synthesis and anti-tyrosinase activity evaluation of fluorinated chalcone and phenyl benzyl ether derivatives. *Thai Bull Pharm Sci*, 2020;15(1):81-89.
3. Singpanna K, Nuntharatanapong N, Rojanarata T, Limpachayaporn P, Patrojanasophon P, Opanasopit P. Development and evaluation of p-chlorophenyl benzyl ether-loaded microemulsions for transdermal delivery. *JCST*, 2021;11(1):90-99.
4. Singpanna K, Dechsri K, Patrojanasophon P, Limpachayaporn P, Opanasopit P, Nuntharatanapong N. Transdermal delivery, cytotoxicity and anti-melanogenic activity of p-chlorophenyl benzyl ether loaded-liposomes. *J Drug Deliv Sci Technol*, 2021;65:102746.
5. Singpanna K, Limpachayaporn P, Sukma M, Athipornchai A, Nuntharatanapong N. Synthesis of fluorinated N-benzylaniline derivatives and evaluations on anti-tyrosinase and anti-melanogenic activities. *Key Eng Mater* 2022;914:87-92.